DIGITIZING VERTEBRATE BRAIN DEVELOPMENT

WITH ULTRASHORT PULSE MICROSCOPY

A Dissertation

by

HOLLY CATHERINE GIBBS

Submitted to the Office of Graduate and Professional Studies of
Texas A&M University
in partial fulfillment of the requirements for the degree of

DOCTOR OF PHILOSOPHY

Chair of Committee,	Alvin T. Yeh
Committee Members,	Arne C. Lekven
	Brian E. Applegate
	Kristen C. Maitland
Head of Department,	Gerard L. Coté

December 2014

Major Subject: Biomedical Engineering

ABSTRACT

Embryonic development is a process of unparalleled dynamism. The only constant in development is change itself- change in size, change in shape, change in gene expression- all driving the formation of an organism from a single cell. While the complexity of these changes is fascinating, it creates quite a challenge for modern imaging systems aimed at visualizing developmental processes.

The embryonic brain is subdivided by unique patterns of gene expression prior to morphogenesis, but the mechanisms linking these phenomena remain poorly understood in part due to the lack of imaging techniques that can capture dynamic molecular, cellular, and tissue-scale dynamics simultaneously in 3-D.

We have established the use of Ultrashort Pulse Microscopy, a platform that utilizes the high peak power and short coherence length of broadband ultrashort pulses to simultaneously generate two-photon excited fluorescence and high-resolution optical coherence signals, and 3-D image registration for integrated imaging and analysis of morphogenesis, genetic cell lineage reporter dynamics, and gene expression domains during embryonic brain patterning in the vertebrate model *Danio rerio* (zebrafish).

Using these tools, we characterized *wnt1* lineage dynamics during midbrain-hindbrain boundary (MHB) formation and found differences in the refinement of gene expression domains along the dorsoventral axis at the boundary where *wnt1* and *fgf8a* form an interface. We then examined these dynamics in *fgf8a* loss of function and showed that initiation of the morphogenetic program at the boundary does not require *fgf8a,* but that anteriorly expanded hindbrain ventricle opening and failure to restrict the posterior limit of *wnt1* expression at the dorsal MHB results in a cerebellar to tectal transformation and termination of constriction morphogenesis.

ACKNOWLEDGEMENTS

Some people view graduate school as a training ground for independence, but the most important lesson I've learned is the value of interdependence. One must go into the desert alone, for a while, but in the end- we all have strengths and weaknesses. So, we try to put all of our strengths together to find something new or solve a problem.

I didn't learn this lesson independently (that would be ironic, wouldn't it?). Many thanks are in order, first to my committee chair, Dr. Alvin T. Yeh, for encouraging me to pursue academic research when I was still an undergraduate student planning rather to stay home with kids. He was there in the right time and place to put me on this path of discovery and has helped me navigate the forks in the road as a ready mentor- not providing much guidance as to what should be done conventionally or practically, but making a space for my curiosity and confidence as a researcher to grow and guiding me back to the question, "What do *you* want to do?"

I also want to thank my committee members, Dr. Kristen Maitland, Dr. Brian Applegate, and especially Dr. Arne Lekven, for always purporting themselves in a most collegial manner and contributing to my development as a researcher. They, and my previous mentors Dr. John Ford and Dr. Colin Campbell, are a pleasure to work with, and not just because of the pie. I look forward to continue working with these excellent investigators in the future.

Thank you to the undergraduate students, graduate students, post-doctoral fellows, and scientists I've had the pleasure to work with in the Yeh and Lekven labs who have been wellsprings of protocol and reagent assistance, data collection assistance, and the oftentimes much needed commiseration and comic relief. I specifically want to thank Dr. Laura Beaster-Jones and Amy Whitener for their support as I entered parenthood and Colin Dodson and Brian Kelly for helping to collect time-lapse data. I spared them the 3 am shift as they were excellent students and I didn't want to put them off of academic research so young, but their help on the afternoon-evening shifts was very appreciated. I'd also like to thank Jo-Ann

Fleming for playing excellent radio programs and music in the lab and being ready to help anyone with anything at anytime.

I'd like to also thank my husband, Brian, who has endured an extended period of "student-ish" life that may have taken him by surprise. As far as this dissertation, his love and unmatched coffee making, cooking, and parenting skills were indispensable. Despite his own busy schedule and business goals, he jumped right in to fill all of the voids left by my rush to finish this dissertation without a single complaint. Did I say he's the best ever? He is.

Thanks to my parents, Mark and Karen, for their love that instilled in me the self-confidence needed to pursue science with its requisite defeats and failures. And, who else besides Nana would agree to babysit Rex in the lab at 3 am while I finish time-lapse experiments? Just Papa if he could skip work, I imagine.

Thanks to my children. My daughter, Thistle, taught me to be brave and not to worry too much about what other people think. My son, Rex, has taught me how to ask for and receive help. I'm looking forward to what else they will teach me.

NOMENCLATURE

UPM	Ultrashort Pulse Microscopy
2PM	2-Photon Microscopy
2PF	2-Photon excited Fluorescence
OCM	Optical Coherence Microscopy
MHB	Midbrain-Hindbrain Boundary
Mes/r1	The domain in the developing brain including the mesencephalon and rhombomere 1 separated by the MHB
FP	Fluorescent protein
ISH	In situ hybridization
FISH	Fluorescence in situ hybridization

TABLE OF CONTENTS

Page

LIST OF FIGURES

Page

1. INTRODUCTION

1.1 Imaging embryonic development

Recently, the fields of developmental biology and microscopy have begun to fuel each other's advancement, but they have been entwined from their beginnings. The light microscope was revolutionary because it enabled scientists to see something new and unimagined- the morphology and structure of embryos during their development. Today's advanced microscopy techniques are revolutionary in a similar sense- they enable scientists to visualize previously invisible cellular and molecular details of embryos during their development. However, rather than reflected light rendering image contrast from the embryo's gross anatomy, we now have many other contrast-generating options including light probing the electronic states of molecules to create contrast from endogenous or exogenous fluorophores (for seeing reporter and fusion proteins or autofluorescence), light probing vibrational and rotational states of molecules to create contrast from molecular bonds (for visualizing lipid-rich structures, for example), and higher order light scattering from molecular structures and interfaces that produces contrast from harmonic generation (extracellular proteins and cell membranes). The modern developmental biologist can use these tools to study the mechanisms of various aspects of embryogenesis, from morphogenesis to organogenesis to cell fate specification, in most cases with the embryo living and intact. It is, therefore, a critical time for developmental biology and optics groups to collaborate, so that existing advanced imaging technologies can be fully utilized to further our understanding of development and so future advances in imaging and other optical technologies will match the needs of developmental biologists.

Live cell imaging utilizing both linear and nonlinear optical signals plays an indispensible role in answering questions in developmental biology, where the ultimate goal is to understand how epigenetic factors and changes in gene expression direct the cell movements, proliferation, and specification that culminate in a living organism. Imaging allows data collection from individual cells with minimal disruption of biological context, so the activity of biological circuits can be precisely analyzed in space and time (1). Dynamic processes that cannot be inferred from still images collected from fixed embryos

are readily understood after analyzing time-lapse data, and dynamic analysis of the formation of mutant phenotypes can reveal previously unappreciated aspects of gene function. Obtaining a comprehensive spatio-temporal atlas of development is another particularly demanding goal in developmental biology, requiring maximizing data collection resolution in many dimensions (*x, y, z, t,* and *lambda* for example). As the genetic and imaging tools for studying developmental biology improve, these questions, having been addressed separately by different research groups up to this point, can be integrated into a comprehensive systems level model of embryogenesis.

In this section, we first present a discussion of the complexity of embryonic brain development, especially the region of the brain at the junction of the midbrain and hindbrain known as mes/r1, followed by a survey of the state of the art in imaging techniques relevant to its study that are based on both linear and nonlinear interactions between light and physical matter.

1.2 Embryonic brain development

During embryonic development, the brain primordium is patterned by secondary organizing centers that govern spatiotemporal differences in gene expression to control cell fate specification (2). During the patterning and specification process controlled by these organizers, there is a concomitant and dramatic morphological rearrangement of the brain primordium from a flat neural plate epithelium into a 3-D, constricted, tubular pseudostratified epithelium.

One such organizer, sometimes referred to as the isthmic constriction or isthmic organizer, resides at a constriction in the embryonic brain called the midbrain-hindbrain boundary (MHB) constriction and is necessary for correct formation of adjacent structures and specification of their constituent neuronal cell types. In zebrafish, the optic tectum forms from the dorsal midbrain compartment anterior to the constriction and the cerebellum from the dorsal region of the anterior-most hindbrain compartment, rhombomere 1. The ventral regions give rise to tegmentum.

Despite their parallel action in embryonic brain development, researchers have addressed genetic regulatory networks and morphological programs quite separately. The following sections provide a

discussion of the molecular and morphogenetic events leading up to, during, and subsequent to the formation of the isthmic organizer. From the discussion, it will be obvious that teams of researchers specializing in a variety of model organisms have been working decades toward understanding the regulatory relationships governing the MHB organizer and its fate patterning activities while only recently, with the establishment of zebrafish as an important vertebrate model for visualizing developmental processes dynamically, has attention turned toward elucidating specific cell behaviors driving morphogenesis with live cell imaging.

1.3 Formation of the midbrain-hindbrain boundary

The organizing properties of the MHB were discovered by chimeric experiments in avian embryos when MHB transplanted to the forebrain and hindbrain was sufficient to induce mes/r1 character in surrounding tissues (3). Subsequently, the identities of the key regulator molecules in this area of the embryonic brain, which we refer to henceforth as mes/r1, were identified with loss of function experiments in several model organisms and their spatiotemporal expression patterns roughly characterized (4). These data provide the basis for the current model of organizer development (shown in Fig 1.1) that involves three steps: 1) positioning of the MHB, 2) independent activation of several key MHB pathways, and 3) maintenance of MHB gene expression through interdependent regulatory relationships. While the isthmic organizer is undoubtedly the most-studied secondary organizer in development, a complete understanding of its regulatory logic is still undetermined. How and when morphogenetic cell behaviors result from the underlying genetic program in a proposed fourth phase- morphogenesis – is also not understood.

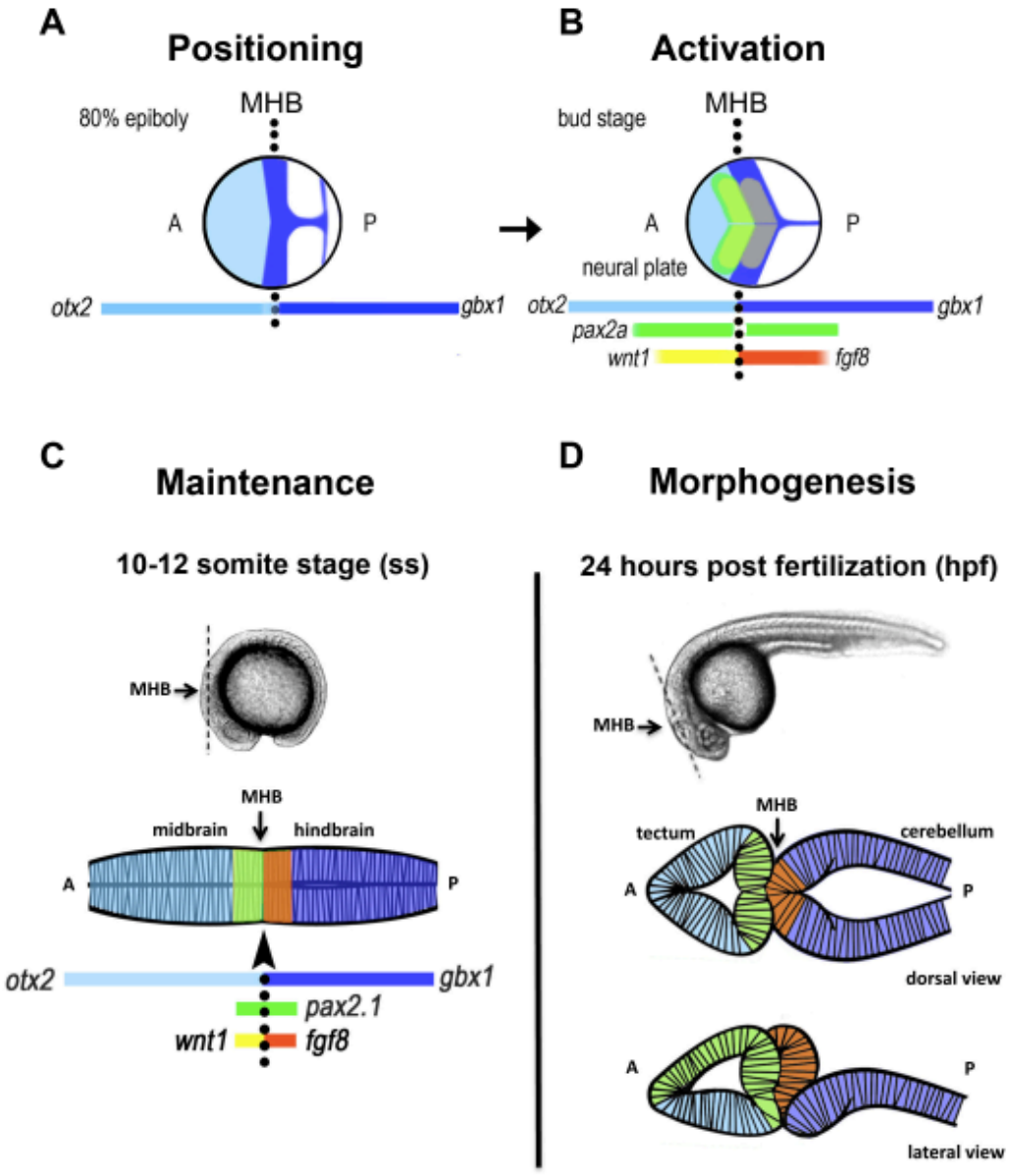

Fig 1.1 Coordinated genetic patterning and morphogenesis at the midbrain-hindbrain boundary (MHB) in zebrafish embryos. (A) The MHB is positioned within the presumptive neural plate during gastrulation by mutually repressive domains of *otx2* and *gbx1* expression. (B) Key signaling molecules and transcription factors are subsequently activated during early neurulation and expression boundaries sharpened. (C) Wnt1, Fgf8, and Pax2 form an interdependent maintenance regulatory loop as neurulation finishes and brain ventricle formation begins. (D) Proper formation of midbrain and hindbrain structures depends on continued maintenance of the MHB organizer genetic program.

1.3.1 Positioning

The position of the future MHB is specified during gastrulation when the shield (the primary organizer in zebrafish responsible for patterning different germ layers) initiates neural patterning by inducing mutually repressive domains of anteriorly expressed *otx2* (in the forebrain and midbrain) and posteriorly expressed *gbx1* (in the hindbrain) transcription factors. When first activated, these domains overlap slightly, but subsequently are sharpened and their interface is hypothesized to create a lineage-restricted boundary that compartmentalizes the developing neuroepithelium during convergence/extension movements into fore/midbrain and hindbrain compartments. Activation of these two genes occurs independently. *otx2* is initiated in the fore and midbrain under the control of several enhancer regions (5), while *gbx1* (6) is activated in the hindbrain by Wnt8 (7). In zebrafish, *gbx1* expression recedes posteriorly and is replaced with *gbx2,* a switch that may reflect an evolutionarily conserved function for zebrafish *gbx2* (8).

The mechanism used to sharpen the boundary is not entirely clear and may vary between species. In some reports from chick, there is discussion of a posterior shift in the position of the Otx/Gbx interface, such that it only coincides with the physical MHB constriction at later stages in development (9). In zebrafish and in mice, however, the consensus is that the Otx/Gbx boundary definitively marks the future MHB constriction prior to when it becomes morphologically visible. In either case, cells initially expressing both *otx2* and *gbx1* must make a choice to turn one or the other off in order to sharpen the abutting gene expression boundaries. In reports from chick, Notch signaling, which classically causes cells to make such boundary decisions by amplification of small stochastic differences in gene expression followed by cell sorting, has been implicated in sorting Otx and Gbx cells at the MHB (10). Other reports from mice and zebrafish suggest that the mixed population at the boundary defaults to hindbrain fate, as Gbx2 can directly compete with POU transcriptional activators of Otx2 (11, 12). In addition, once cells have committed to one side of the boundary or the other, the action of other subsequently expressed MHB genes, such as members of the Wnt and Fgf signaling pathways and Pax and Engrailed transcription factors, may also work to enhance this mutual repression (13, 14).

1.3.2 Activation

Once the Otx/Gbx boundary positions the isthmus organizer within the mes/r1 region, a distinct genetic program is subsequently activated in this territory (9). Mis-expression of either transcription factor under the control of a more anterior or posterior promoter can shift the position of the Otx/Gbx boundary and consequently, expression of MHB genes (15). However, double knockdown of the Otx/Gbx pair does not impede the subsequent molecular specification and morphogenesis of a fairly normal mes/r1 (16, 17). Thus, it would seem that while Otx/Gbx positions the MHB, neither is required for activation of MHB genes including the *pax*, *eng*, *wnt*, and *fgf* gene families. What is responsible for activating these genes is not yet understood.

Once activated, secreted signaling molecules play an important role in development as they can create gradients that provide positional cues to cells that in turn direct their identity. As previously mentioned, the key signaling molecules in the mes/r1 domain were mostly identified through loss of function studies. $Wnt1^{-/-}$ and $Fgf8^{-/-}$ mice fail to develop the entire mes/r1 region (18, 19). In zebrafish, loss of several redundant Wnts (Wnt 3, 3a, 1 and 10b) recapitulates a similar phenotype (20, 21) and the zebrafish *fgf8a* mutant lacks a cerebellum, though the midbrain is present but unpolarized, resulting in aberrant retinotectal projections (22). While it is unclear at this point how similar the regulatory relationships among and roles for MHB genes are between species, the key players are certainly conserved and worthy of further study.

In addition to signaling molecules, there are several transcription factors that begin to be expressed across the MHB boundary during the activation phase including *her5* in zebrafish, and Pax and Engrailed transcription factors in vertebrates generally. Different combinations of expressed transcription factors have the ability to confer differential competence to surrounding secreted signals to help direct cell fate. Important transcription factors in mes/r1 have also been identified by loss of function analysis. For example, the zebrafish *no isthmus* mutant, which lacks functional *pax2a,* loses the tectal and cerebellar structures in mes/r1 during mid somitogenesis due to massive apoptosis (22). The targets of these

transcription factors, and thus their potential roles in morphogenesis and cell specification, however, remain largely a mystery.

Fgf8 has been deemed the most important "organizing molecule" by the majority of the scientific community based on results from implanting Fgf8-soaked beads at sites anterior and posterior to the MHB. In these experiments, Fgf8 was sufficient to induce tectal and cerebellar structures and an underlying Otx/Gbx boundary, while similar experiments for Wnt1 showed no significant re-patterning of the surrounding tissues (23). Indeed, no gain of function analysis for all the other major MHB molecules in any organism has yielded such striking results; leading to the general acceptance that Fgf8 is "the" organizing signal. However, a recent study in which Otx2 and Fgf8 were simultaneously knocked down has challenged the idea that Fgf8 is required to pattern cell fates in the MHB. Foucher et al. showed that in the absence of Fgf8, if Otx2 levels were depleted, cerebellar neurons were able to successfully differentiate (24). A role for Wnt1 at the boundary has not been agreed on, though in mice it is shown that Wnt1 may have an important role in regulating the proliferation of a precursor pool of neurons in the midbrain (25). Many otherwise assume Wnt1 to function as a mitogen because of its previous association with that role in the developing spinal cord (26).

The activators and targets of key MHB genes remain largely to be determined. It is important to understand the upstream regulation of these organizer genes, which occurs during gastrulation and early neurulation, to disentangle the evolution of the Otx/Gbx boundary into the site of a powerful local organizer center. It is important to enumerate their downstream targets so that we can understand how this signaling program translates into the cell behaviors that shape the brain architecture in this region and lead to the specification of different types of neurons that may be of clinical significance for regenerative therapies.

1.3.3 Maintenance

To add another layer of complexity to the regulatory architecture of this region, once activated, the MHB gene program transitions to a maintenance phase where Fgf8, Wnt1, and Pax2 become dependent on each

other for expression (27). Loss of any one of these genes during the maintenance phase results in loss of the others and subsequent failure of the MHB organizer to execute properly. The transcription factor Lmx1b appears to mediate dependency between Fgf8 and Wnt1 at the isthmus (28, 29), but as with the activation phase, exact regulatory relationships have been difficult to tease out of complex *in vivo* systems.

Maintenance of the MHB organizer is important for the morphogenesis of the region and eventual differentiation of neuronal subtypes (30). During early stages of MHB formation, neurogenesis is actively inhibited by *her5* in zebrafish (31) but subsequently neurons are born as *her5* expression recedes to a narrow ring at the constriction. In the midbrain, beta-catenin stabilization from Wnt signaling and intersectional Shh signaling are important for dopaminergic neuron formation in mice (13, 32). Studies in zebrafish have shown that for catecholaminergic neurons (including dopaminergic neurons) in general, Nodal may play a more important role in specification, while combinatorial Fgf8 and Shh regulate their proliferation or the proliferation of their precursors (33). In the hindbrain, differentiation of cerebellar cell identities happens in spatiotemporal waves emanating from the cerebellar plate and the upper rhombic lip. Recently, these migrations were shown to be conserved in mice and zebrafish, with discrete Wnt1 populations in the upper rhombic lip sequentially migrating anteriorly toward the MHB and turning ventrally to their final positions in the hindbrain tegumentum (34).

miRNAs have recently been appreciated as contributors to the molecular maintenance of mes/r1 as well. Wnt1-cre-mediated conditional loss of Dicer in mice leads to MHB malformations and problems with both neural crest induction and dopaminergic differentiation (35). Also, Mir-9 has been shown to direct late organizer activity by modulating FGF signaling and regulating neural progenitor pool size (36).

The seemingly convoluted bi-phasic regulation (activation and maintenance) of these important MHB genes may be a reflection of the dynamically changing physical environment these cells find themselves in starting as early as gastrulation. In the next section, we introduce the tumultuous morphogenetic events occurring concomitantly with the positioning, activation, and maintenance of these genetic programs within the mes/r1 region.

1.3.4 Morphogenesis

During the time the isthmic organizer is positioned and activated, the neural tube is undergoing significant morphogenetic movements, including convergence/extension movements driving the elongation of the neural plate along the anteroposterior axis and subsequent invagination on the dorsoventral axis resulting in the formation of an epithelial neural tube. The details of convergence/extension and cranial neurulation vary from species to species, but generally there is a significant amount of conservation in cell behavior (37). Once the neural tube is formed, the MHB subsequently transitions to the maintenance phase that is accompanied by dramatic reshaping of the brain tissue and ventricular system, as well as production of cerebrospinal fluid that may itself contribute to MHB regulation (38, 39). Some would argue morphogenesis is a distinct process independent of the genetic programs underlying cell fate specification we have already discussed, but we argue that morphogenesis and cell fate specification programs are interdependent.

One of the earliest cell behaviors that gives shape to the developing neural territory appears to be lineage restriction. The early neural plate is an epithelium, thus there is little cell migration in the anteroposterior direction as determined by fate maps and evaluation of clonal cell dispersion during gastrulation (40). This is not surprising, since epithelial cells are highly coupled by gap junctions and act as coordinated sheets rather than individual cells in the absence of an epithelial-to-mesenchyme transition. However, some controversy remains regarding the possibility of leakiness in this lineage restriction boundary throughout different stages of development and what the exact mechanisms governing boundary formation may be. In chick, it would seem lineage restriction occurs later than in other models after cell sorting is achieved via Notch signaling mediated by Lrrn1 (41, 42). Other studies in mice and zebrafish suggest that by early somitogenesis stages, there is no cell mixing across the MHB. Notably a study in zebrafish characterized this restriction with extended time-lapse imaging and cell tracking (albeit only within a relatively shallow depth of field) (43, 44). Intercellular actinomyosin networks that have been shown to drive morphogenesis, such as during mesoderm invagination in *Drosophila*, may also play a role in lineage restriction (45).

Following convergence extension, restricted lineages are located along the anteroposterior axis of a relatively uniform neural plate that thickens and undergoes neurulation. This process of primary neurulation can vary significantly along the anterior-posterior axis of the cranial region, with transverse sections from the midbrain varying significantly in morphology from those in the hindbrain as the neural tube (neural keel in teleosts) takes shape. Once the neural tube forms, visible constrictions begin to delineate compartments within the brain that are sometimes termed neuromeres, though exactly what causes these neuromeres to become visible is debatable. Possibilities include local and differential constriction of the neural tube and differential cell growth and cell shape changes. In zebrafish, it has been shown MHB constriction requires basal constriction of cells at the mes/r1 boundary (46). Computational modeling and experimentation in chick indicate importance of differential myosin-mediated contractility to produce brain ventricle geometry and suggest strategies may differ from compartment to compartment depending on the end fate of the junction, as some are only transient structures (rhombomere boundaries, for example) while others, such as the MHB constriction, persist as structures in the adult brain that must resist increasing fluid pressure from the ventricular system (47). Using a similar computational approach, it was shown that slightly tweaking contractility of the neuroepithelium can recapitulate species-specific differences in brain ventricle morphology, emphasizing its importance as an evolutionarily conserved mechanism for brain morphogenesis (48).

There has been little characterization of how patterns of cell proliferation may affect these processes; though it is likely they will be incorporated into models as data from in toto time-lapse imaging become more readily available. For example, such patterns have been used to understand how the mes/r1 region, specifically the tectum, is shaped by cell proliferation in chick embryos (49).

1.3.5. Intersection of mechanical and genetic regulation of development

A major disconnect, which has been difficult to address using genetic manipulations in animal models, is specifically how certain signaling molecules are transduced by secondary molecules and downstream effectors to regulate gene transcription and subsequently cell behavior. This is precisely the arena,

however, in which the major signaling molecules of the MHB may intersect with and regulate cytoskeletal remodeling to produce the isthmic constriction. Boundary cells clearly receive signals that differentiate their mechanical behavior from their neighbors, but such behaviors and their upstream signals have yet to be well characterized. Literature searching reveals little research in this arena, but we present what we have found. None of these examples address the mes/r1 region, but are of use for sparking future lines of inquiry and do relate to the majoring signaling families in the mes/r1 region, the Wnts and Fgfs.

One example linking Fgf signaling with morphogenetic remodeling of the cytoskeleton has been proposed to work through Fgfr-Ras-MAPK signaling in the formation of the lateral line sensory system in zebrafish (50). In this study, authors found that Ras-MAPK signaling activated by Fgfr was required for the formation of rosettes by localizing Rho-associated kinase (Rock) to the apical surface to drive its constriction. Fgf signaling has also been shown to have a role in otic vesicle formation, which requires apical constriction mediated by local increases in actin. In the otic vesicle, FGF signaling activates phospholipase-C which triggers non-canonical myosin-II activity (51). Classically, myosin-II is understood to ratchet along actin filaments to promote contraction, however, upon phosphorylation by PLC, myosin-II promoted the degradation of basal actin (resulting in enriched apical actin and otic cup invagination).

Wnt signaling has also been implicated in cytoskeletal remodeling via the planar-cell-polarity pathway and perhaps also canonical signaling pathways (52). It has been shown that novel Wnt receptors Ryk and Rok can interact with the cytoskeleton to promote axon guidance (53). While these examples remain few, advances in fluorescent tagging and live sub-cellular imaging should make it more straightforward to begin to understand important cytoskeletal changes and their upstream signals during MHB formation.

There are still many open questions regarding how correct brain architecture is formed and cell types designated during neural development, though a thorough understanding of these processes are of extreme importance from a basic science perspective and also for advancement of regenerative medicine in neural disease. There is continued debate on the evolutionary origins of the MHB organizing center and

a precise inter-species comparison of this secondary organizer at a systems level remains for future study. In fact, a systems level understanding of this organizer in any single model species remains to be seen but would be of great value.

The simultaneous generation of correct brain morphology, cell types, and neural circuitry is a daunting challenge but appears to be very robust and adaptable. Cell behaviors such as differential adhesion, growth and apoptosis, migration, and cytoskeletal remodeling must be precisely coordinated over large regions within the developing neuroepithelium and this achievement is so astounding that it is understandable we have been both fascinated and frustrated with our attempts to understand the process as a whole. Moving forward from here to a more complete mechanistic understanding connecting the earliest patterning events with eventual brain architecture and cell fates will require enhanced cooperation between disciplines so that the best possible models can be formulated and thoroughly tested.

1.4 Approaches to imaging embryonic development

Having discussed the complexities of embryonic brain development in the mes/r1 region, we survey the linear and nonlinear imaging tools aimed at resolving open questions in developmental biology by dynamically capturing data from live organisms.

1.4.1 Confocal microscopy

Of the high-resolution microscopy techniques, confocal microscopy is the most common. The concept of blocking light from above and below the focus of an imaging objective with a pinhole in a conjugate focal plane was patented by Marvin Minsky in 1961. Minsky studied neural connections as a doctoral student, and in his memoir he describes his interest in reverse engineering the circuits of the brain (54). The first step toward this goal, he reasoned, was to generate a comprehensive wiring map of the brain, what we would call today a "connectome." However, Minsky realized the state of the art in both imaging and labeling at the time were not adequate tools for this task, and these limitations motivated him to develop a method for optically sectioning biological specimens. Minsky was hesitant, however, to attempt to use

scanning optics and so to generate images used a scanning stage instead, which made acquisition time relatively long and introduced vibrational artifacts into images. It was not until White and independently, Carlsson, invented the laser scanning confocal microscope in the 1980's that the biology community fully embraced the confocal microscope (55, 56). Many of the first important demonstrations of the improved axial resolution obtained with confocal fluorescence microscopy were done in embryos, including White's landmark paper reporting images of a fertilized sea urchin egg, *Drosophila* larvae, *C.elegans* embryo, and a chick embryo (57).

Confocal microscopes improve upon conventional wide field fluorescence microscopes by i) using point illumination to reduce scattering and ii) eliminating out-of-focus background signal with a pinhole at a conjugate imaging plane (58). The smaller the pinhole, the better the axial resolution. There are many variations of confocal microscopes including a popular option, the tandem-scanning or spinning-disk confocal microscope, that uses a spinning disk of micro lenses to illuminate several points on the sample at a time so data acquisition is faster. Petran and Hadravsky invented the tandem scanning confocal microscope in the 1960's (59) to image reflected light but it was not until lasers were more readily available that the high-loss spinning disk was suitable for fluorescence imaging.

One advantage of confocal microscopy is speed, making it a good choice for investigating relatively rapid processes over moderate periods of time. Most instruments provide temporal resolution adequate for imaging morphogenesis, cell migration and division, and dynamics of sub-cellular structures when imaging one or two fluorescent markers over a small field of view. For example, two-color time-lapse confocal microscopy of zebrafish embryos showed direct development of blood stem cells (marked by *cymb*:eGFP) from the ventral portion of the dorsal aorta (marked by *kdrl:*memCherry) during heart morphogenesis and their entrance into the circulation via the caudal vein (60, 61). Confocal microscopy has also performed well in studies requiring sub-cellular resolution. In a study of oligodendrocyte progenitor cells (OPCs) in zebrafish, Kirby et al. showed that dynamic filopodia extension and retraction between neighbors was important for spacing OPCs evenly along axons prior to myelination (62). Neighboring filopodia were resolved by using a transgenesis strategy that caused OPCs to randomly

express RFP, GFP, or a combination of RFP and GFP. In a study of replication licensing in *C.elegans* embryos, Sonneville et al. used spinning disc confocal microscopy to image several transgenic lines that expressed mCherry-H2B and GFP fused with protein components of the replication licensing program, to view the dynamic interaction of each these components with chromatin during meiosis I, II and mitosis (63). They found that, in contrast to what was reported from work in cell culture, in *C.elegans* replication-licensing proteins were exported from the nucleus to prevent re-synthesis during S-phase instead of being degraded, possibly due to the transcriptionally silent cell cycle in the early embryo. Thus, confocal microscopy has been established to study protein localization and regulatory networks *in vivo*.

Many researchers associate confocal microscopy with fluorescence microscopy, but confocal microscopes can be used to detect scattered or reflected light as well. In reflectance mode, the incident light that is scattered back toward the objective is detected, usually discriminated from the incident light by some other means than wavelength, such as polarization or off-axis detection. This mode has been used to study cataract formation in zebrafish *cloche* mutants (64), to determine the viability of mouse embryos *in vitro* (65), and to characterize heart defects due to ethanol exposure in *Xenopus* embryos (66).

One-photon excitation schemes are not generally used for simultaneous imaging of fluorescent proteins variants, since excitation and emission wavelengths overlap, so instead they are imaged in rapid sequence to get data as nearly simultaneously as possible. Teddy et al. has reported 4-color imaging in chick using confocal microscopy (67). Another approach is to multiplex marker data from independent confocal stacks from different experiments *in silico,* which has been promising in *Drosophila* and *C.elegans* (68, 69). However, the approaches in those studies relied on the relative simplicity and stereotype of those particular model organisms and would be difficult to implement in vertebrate embryos. To develop dynamic virtual embryos or atlases of gene expression with cellular resolution in vertebrate embryos will require multi-marker imaging.

One of the significant limitations of confocal fluorescence microscopy is that the sample is illuminated and signal is generated throughout the z-axis, resulting in out-of-plane photobleaching. This continuous illumination can be detrimental when imaging live embryos over extended periods of time and

has impeded its use to study extended periods of development. Another disadvantage is limited imaging depth, which has been less problematic in zebrafish and *C.elegans* embryos that are relatively transparent, but is unsuitable for *in vivo* imaging in other model organisms.

1.4.2 Light sheet microscopy

Light sheet microscopy, which has been used for both one- and two-photon fluorescence imaging, has recently emerged in the developmental biology community (70-73) and goes by several names including SPIM (selective plane illumination microscopy), mSPIM (m for multidirectional), and DSLM (digital scanned laser light sheet microscopy), denoting differences in configuration and formation of the light sheet (74). The basic principle of SPIM was developed in 1903 by Siedentopf and Zsigmondy (70), but as with confocal microscopy, the technique did not impact the biological community until much later when in 2004, Stelzer's group demonstrated the first use of SPIM *in vivo* to image both the relatively transparent medaka embryo and more opaque *Drosophila* embryo (75). To create a sheet of light, Huisken et al. used a cylindrical lens, which focuses light along one axis instead of two, as a spherical lens does, creating a sheet of light rather than a point. The sheet is scanned through the sample and the signal detected by an objective lens placed at a 90° angle that images onto a charged-coupled device (CCD) array. This way, an entire xy image is collected at once, and by scanning the z-axis, image stacks can be collected very quickly.

More recently, light sheets have been created by fast-scanning a laser beam with a long depth of focus along one axis (DSLM), providing significantly higher signal to noise ratios than previous approaches (76). In demonstrating DSLM, Keller et al. characterized nuclear movements in zebrafish over the first 24 hours of development for both wild type and *Mzoep* mutant embryos. Keller et al. found that the mechanism of hypoblast formation during epiboly varied by position, with dorsal mesendoderm forming by ingression and ventral mesendoderm by involution. *Mzoep* mutants failed to internalize cells to form the hypoblast.

SPIM can also be used to synchronize photochemistry over a large area of the embryo, which is important for controlling or studying rapid processes. Optogenetics is an emerging field in which organisms are genetically engineered so that a biological process can be controlled with light, combining transgenesis and photochemistry. In a recent study Arrenberg et al. generated a line of zebrafish expressing rhodopsin-based light-gated ion channels in differentiating cardiomyocytes (77). Optical activation of the chloride ion gate with orange light coupled with the detection arm caused pacemaker depolarization to stop (reversibly), and when the orange light was removed, pacemaker depolarization resumed. Using a micro mirror device to pattern the orange illumination light, the authors selectively tested pacemaker functionality from different areas of the sinoatrial region by shaping and moving this pattern over the developing heart tube while imaging the response with SPIM. Using this approach, the authors were able to identify all the functional pacemaker cells at different stages of development and concluded that very few pacemaker cells are required to induce a heartbeat. This method is an exciting new way to be able to image and test the functionality of an organ during its development. Another group has developed an elegantly simple design for SPIM microsurgery they term SPIM-microscapel which provides a more direct way to influence developmental processes through plasma ablation (78). They demonstrate the ability to use 355 nm pulses of 470 picosecond duration to dissect microtubules, cut zebrafish fins, and induce hemocyte immune response in *Drosophila* embryos to a point of targeted ablation while near-simultaneously imaging with SPIM.

The perpendicular geometry of the illumination and detection arm in SPIM can be more practical than parallel illumination and detection for imaging embryos that need to be mounted in agarose, like zebrafish, but cumbersome for imaging samples on a microscope slide. Wu et al. has engineered a useful solution to this problem by developing a simple v-shaped SPIM illumination/detection arm for attachment to an inverted microscope base (iSPIM) (79).

The limitations of SPIM currently are penetration depth and marker multiplexing. One approach to improving the imaging depth has been to use structured illumination DSLM (71). Structured illumination is a technique that can be used to discriminate scattered background photons from signal

photons by illuminating the sample with a pattern, usually a grid of lines, rather than uniformly. Post-processing of several differently illuminated images of the same plane can optimize resolution, and this approach is also used in some "super-resolution" microscopy techniques. Since scattering increases with depth, this allows deeper imaging, though at the cost of acquisition time. Two-photon SPIM also may be useful for increased imaging depth (80). In terms of marker multiplexing, live time-lapse SPIM has been limited mainly to two-color movies similar to confocal microscopy. The ability to capture all cell movements and divisions within the zebrafish embryo also presents an opportunity to study lineage similar to what has been done in *C.elegans* and to quantify the variability in cell lineages is in a vertebrate model, which would be useful for understanding the variability in digital atlases of zebrafish development.

1.4.3 Optical Coherence Tomography/Microscopy

Optical coherence tomography (OCT), introduced by Fujimoto's group in 1991 (81), is a useful technique since in the majority of applications, OCT does not require the use of exogenous labels. OCT was developed for clinical applications in the eye and skin. The near-infrared wavelengths used in OCT/M have been deemed safe for clinical use by the FDA and are scattered by biological tissues less than UV light, so they can penetrate deeper, greater than 1 mm depending on the sample. Because of these clinical beginnings, those groups developing OCT/M have capitalized on its label-free method of generating imaging contrast. Because of its application to imaging the rapidly moving eye, it has also been driven towards rapid acquisition. OCT/M has been compared to other tomographic techniques such as high frequency ultrasound, micro-CT, and high resolution-MRI and has been put forward as an option with better resolution for screening birth defects in mammalian embryos (82).

The coherence in OCT/M refers to the fact that in order for light waves to constructively or destructively interfere with each other, their fields must be correlated to some degree in space and time. This property of light waves is called spatial and/or temporal coherence. The contrast in OCT/M images comes from the interference of back-scattered light from the sample and light reflected from a separate reference arm that ends at a mirror. A typical OCT/M setup has a beamsplitter to create these two arms,

sending them to the sample and reference respectively, and recombining the reflected signals so that they can interfere with each other on the way to the detector, provided they are matched within the coherence length of the light source. If the reflections are mismatched, there is no interference and consequently no signal, and this is the mechanism that generally provides the axial resolution in OCT that can be 2-10 um depending on the bandwidth of the source (83). Sources with broader bandwidths have shorter coherence lengths and consequently provide better axial resolution. Common sources for OCT/M include superluminscent diodes, supercontinuum sources, and pulsed lasers. There are two main forms known as time-domain and fourier-domain OCT, with fourier-domain OCT being more prevalent as the reference arm does not need to be scanned to match the scanning in depth along the z-axis, since spectral detection encodes the profile of reflections along the whole z-axis within the confocal parameter of the objective lens.

For OCT, tomographic nomenclature may be used to describe the data. An A-line (axial line) is obtained instantaneously, while a B-scan is a 2D image created by scanning the A-line along the x- or y-axis. This way the image generated is not rendered en face (x,y), as with more familiar microscopes, but rather xz or yz images are rendered and 3-D data may also be easily generated. OCM, on the other hand, uses conventional point-scanning and is usually employed when higher lateral and axial resolutions are desired.

An early demonstration of OCT for imaging embryos was given by Boppart et al. in 1996, who reports detailed morphology of opaque embryos such as *Rana pipiens*, *Xenopus laevis*, and *Brachydanio rerio* (84). Several other demonstrations for different varieties of OCT/M applied to imaging embryonic development have been given (85). For example, in the murine cardiovascular system, OCT was used to study congenital heart malformations (86). Interestingly, because of its superior imaging depth, OCT/M has also been used to image mice *in utero* even without the need to dissect the uterus from the mother (82). This approach will be able to powerfully characterize the details and timing of how congenital malformations arise in mammals in longitudinal studies.

Rapid, label-free imaging of morphogenetic processes are of interest as more groups begin studying the mechanical forces that contribute to developmental programs (87). For forces driving morphogenetic processes, OCT/M imaging can provide the input parameters for mechanical simulations obtained from label-free time-lapse imaging. For example, Varner et al. used OCT combined with tracing vital dyes to create a model of mechanical forces driving head fold formation in chick embryos (88).

Other features than morphology can be visualized using only slightly more complicated OCT/M setups that incorporate patterned illumination. A variation called speckle variance OCM can be used to image moving parts within an embryo such as blood cells moving within the developing vasculature and can be used to estimate relative blood flow. This technique has been used to study the relationship of neurons and blood vessels in the rodent spinal cord (89) and has also been used to study blood vessel development in live mammalian embryos (90).

OCT/M is limited in that while it provides "label-free" contrast, these signals generally lack molecular specificity. Another limitation of OCT is relatively poor spatial resolution compared to confocal or multiphoton imaging because of the need to balance depth (confocal parameter) and lateral resolution, which are coupled properties of the imaging objective. By moving from A-line scanning in OCT to point-scanning OCM, axial and lateral resolution becomes comparable to confocal or multiphoton imaging, but at the expense of acquisition time.

1.4.4 Two-Photon Microscopy

Two-Photon microscopy (2PM) is the nonlinear optical microscopy (NLOM) technique that has been most broadly adopted by developmental biologists to date (91). The theory of two-photon absorption was developed by Maria Goppert-Meyer in the 1930's but the phenomenon was not observed experimentally until after the invention of the laser in 1960 by Maiman (92). Once a light source with a high enough photon density was finally available, Kaiser and Garrett made the first report of two-photon excited fluorescence (93). The application of the technique to microscopy of biological samples was pioneered by Denk and Webb in the early 1990's (94) after the invention of the now most common laser source for

2PM, the titanium:saphhire (Ti:Sapph) solid-state laser, now a turn-key laser source requiring relatively low maintenance compared to previously used dye-pulsed lasers. This advance in user-friendliness of short-pulsed laser sources was key to the adoption of NLOM by biologists.

2PM signals arise from the third order optical susceptibility, $\chi^{(3)}$. Two-photon absorption occurs when two photons from a pulse of near-infrared light arrive simultaneously at a molecule and are absorbed, exciting an electron to a higher energy state. Two-photon absorption spectra are available for many dyes and fluorescent proteins and conventionally, a 100-170 fs pulsed Ti:Sapph laser is tuned to an absorption peak of the fluorophore of interest for imaging. If more than one fluorophore is imaged, the laser will be tuned to a compromised wavelength. Green fluorescent protein (GFP) has a two-photon absorption peak at 940 nm, which coincides roughly with twice the wavelength of the one-photon peak at 488 nm. The two-photon peak is not exactly twice the wavelength of the one-photon peak because quantum mechanical selection rules prevent one and two photon transitions to the same electronic state. The fluorescence emission generated from multiphoton absorption however, either autofluorescence or fluorescence from exogenous fluorescent dyes or proteins, are usually the same as for one-photon excited fluorescence because the excited electron typically relaxes non-radiatively down to the one-photon transition state before releasing a photon. Two-photon excited fluorescence signals, being significantly weaker than one-photon excited fluorescence signals, are typically detected using photo multiplier tubes (PMTs).

2PM quickly became popular for studying neurodevelopment in mice. Due to the near infrared excitation wavelength, 2PM can penetrate through a thin-shaved skull or an implanted window deep enough to observe many neurobiological processes *in vivo* (95, 96). 2PM continues to be frequently coupled with tracer dyes and intracellular calcium sensing dyes to study circuit function and development both *in vivo* and in brain slices. In a recent study, 2PM was used to study the developmental dynamics of the unique one-to-one innervation of the auditory neurons in the calyx of held (97). Imaging dendritic spines with 2PM has shed important insights on the mechanism of Fragile X Syndrome, a genetically based pleiotropic form of mental retardation that is manifested as social, perceptual, and motor

dysfunction linked to the FMR1 gene on the X chromosome. Fragile X mice have been suggested as a model for autism. Pan et al. used transcranial 2PM to study the dynamics of dendritic spine formation in Fmr1 KO mice from 2 days post natal to 1 month. Imaging a YFP reporter that is expressed in just a small subset of motor neuron axons (98), they found that previous reports of increased numbers of immature looking dendritic spines in these KO mice could be accounted for by a higher rate of turnover or plasticity of these spines (99). This dynamic aspect of the mutant phenotype could only be realized with time-lapse microscopy. Cruz-Martin et al. independently confirmed these results with 2PM, and also showed that blocking mGluR signaling, which is upregulated in FmrKO mice, surprisingly enhanced the immature dendrite phenotype rather than suppressed it (100).

2PM can image fast enough to study morphogenetic cell movements deeper within the embryo and with less phototoxicity than one-photon excited fluorescence techniques since near infrared light is both scattered and absorbed less by tissues (101). Halacheva et. al. used 2PM to simultaneously image cell proliferation and cell movements during mammalian primitive streak formation in rabbits, which are useful models since implantation occurs later compared to mice and rabbits have a disc- rather than a cup-shaped epiblast (102). The authors found that some cells near the forming primitive streak in the posterior gastrula elongation (PGE) will pass through neighboring cells which subsequently reconvene after the cell has passed, a new movement they call "processional cell movement" and also noted preferred alignment of metaphase plates with the A/P axis by late metaphase, preceded by rotations of the mitotic spindle until the preferred orientation was achieved. In *Drosophila*, there have been several excellent studies on ventral furrow formation. McMahon et al. used 2PM with excitation and detection optimized for GFP to capture all cell movements of the ectoderm and emerging mesoderm in *Drosophila* for both normal and *htl* Fgf8 receptor mutant backgrounds (103). They were able to analyze differences in cell behavior to uncover the mechanism of Fgf to help furrowed cells collapse and form the mesodermal layer by guiding them back down to the outer ectodermal layer. Video force microscopy, where computational mechanics is combined with time-lapse 2PM, was used to study mechanical forces during these ventral furrow formation dynamics in *Drosophila* (104).

2PM is also useful for studying how organs are formed from progenitor subsets because of its superior penetration depth. Taking advantage of the low scattering of red light for both excitation and fluorescence emission, Hagerling et al. developed a *prox1* mOrange reporter mouse for imaging lymph development, a complex process where nascent lymph vessels must successfully separate from the blood circulation and create their own networks of vessels (105). The authors demonstrated combined 2PM and second harmonic generation (SHG) imaging of developing superficial lymph beds in fetal mouse skin, which can be used to study the dynamics of lymph vessel formation combined with extracellular matrix interactions.

Single marker imaging or imaging coupled with parallel assays can provide important information about fate specification mechanisms. McDole et al. utilized 2PM to study early fate decisions in the pre-implantation mouse embryo (106). Tracking nuclear movements and divisions marked with H2B-GFP fluorescence between 8 and 32 cell stage, the authors identified an intermediate population which contributed to both inner (inner cell mass) and outer (trophectoderm) fates and showed the fate decision between trophectoderm and the inner cell mass depends on cell-division order. Importantly, these authors also conducted thorough viability experiments demonstrating that with 2PM imaging every 6 minutes during this sensitive developmental phase, complete developmental competency was maintained. Simply visualizing these dynamic processes in 3-D led to significant new insights.

To conduct an experiment following the genetic profiles (marked by several reporter transgenes) of specific lineages during fate specification will require spectral time-lapse imaging because of the broad fluorescence emission profiles of genetically encoded fluorescent protein variants (107, 108). These broadly overlapping excitation and emission spectra make it impossible to separate spatially co-localized combinations of close variants, for example CFP, GFP, and YFP, using standard glass filters since such filters discriminate only by wavelength. While the wavelengths for excitation and emission overlap significantly, each variant does have a unique spectral fingerprint that can be visualized by dispersing the wavelengths of the emission and imaging them onto a detector. After collecting such “lambda-stacks” for each pixel in an image, over-lapping fluorescent protein emissions can be separated with mathematical

algorithms that take these unique fingerprints into account. In fact, co-localized fluorescent protein emission profiles will be simply a linear sum of the contributions of each individually present fluorophore. This scheme is also sometimes referred to as "multi-spectral" imaging, to illustrate that multiple spectral profiles are unmixed for multi-marker imaging.

The most significant limitations of 2PM currently are speed and cost. Speed of acquisition is limited by signal generation, since 2-photon excited signals are weaker than one-photon excited signals and are generally detected with PMTs. One approach to improving speed has been to create multiple points to scan at once, splitting image acquisition into simultaneous parallel scans (109, 110), somewhat similar to how confocal microscopy speed was improved by moving from laser-scanning to spinning-disk illumination. Two-photon implementations of light sheet microscopy have also demonstrated improved imaging speeds and improved embryo viability (80). Cost may be brought down by exploring other ultrashort pulse sources such as semiconductor disk lasers that can be built with wafer manufacturing technology and can be pumped with relatively low-power sources (111). The commercial models currently available cost about a quarter to half a million dollars, however, one can build an in-house system for less. One advantage of a home-made system is that it can be more easily outfitted with other implementations, such as one custom-built system integrated with a suite of electrophysiology tools for neurobiology (112).

Multi-marker imaging will also be important for imaging the parallel fate specification events that accompany morphogenesis and organogesis since complex organs are likely to comprise multiple interacting cell lineages thus necessitating methods for imaging multiple lineages at once. Two-photon excitation spectra are red-shifted out of the emission range of most fluorescent protein variants, so unlike with one-photon excited fluorescence, simultaneous excitation and detection of multiple markers is achievable. The usefulness of such an approach has been elegantly demonstrated by Mahou et al. in a scheme that uses two excitation wavelengths to target the two-photon absorption peaks of three different fluorescent proteins simultaneously for imaging the formation of neural circuits with the "brainbow" labeling system (113).

1.4.5 Harmonic generation microscopy

Harmonic frequencies are integer multiples of a fundamental base frequency. Harmonic generation is a nonlinear scattering process where two or more incoming photons, best thought of as waves in this process, are mixed together by the structure of the material being imaged, resulting in a signal at two or more times the frequency of the original wave (114, 115). The discovery of harmonic generation followed a similar trajectory to that of two-photon excitation, but second harmonic generation was experimentally observed and implemented as a microscopy modality before two-photon excited fluorescence based microscopy (116, 117). The technological advances that made 2PM both possible and more accessible are the same for second harmonic generation (SHG), while third harmonic generation (THG) has required the use of longer wavelength sources (>1000 nm) so that the third harmonic (1000/3 = 333 nm) would remain in the visible-uv spectrum to match the range of commonly available collection and detection optics (118).

The generation of second harmonics arises from phased-matched wave mixing in crystals that have a chiral structure, lacking a center of symmetry which results in nonzero components of the second order optical susceptibility term, $\chi^{(2)}$. The most common biological substance that fits the description is collagen, whose handed alpha-helical protein structure aggregates into larger ordered fibrils with a crystalline structure. Third harmonic signals are generated from spatial variations of the electronic part of the third-order susceptibility, $\chi^{(3)}$, that are typical at interfaces like aqueous-lipid interfaces such as cell membranes. These signals are usually inherent to the sample, so harmonic generation imaging is "label-free". Harmonic generation is a parametric process, which means that no energy is transferred to the sample and, consequently, photobleaching is irrelevant and depending on the background absorption of the excitation source, photodamage is less of a concern. Harmonic generation is so "non-invasive" that is has been put forward as a potential clinical method for screening the viability of embryos for in vitro fertilization (119).

Researchers have taken advantage of the parametric nature of SHG and THG to image sensitive early periods of development completely "label-free". Olivier et al. published a landmark paper demonstrating the power of this technique to study cell lineage in zebrafish embryos during the cleavage

stage (120). Using a special spiral-scanning pattern that increased pixel dwell time for center of the field of view, which correlated to the innermost part of the embryo, these authors captured all cell cycle dynamics up to the 1000 cell stage, creating lineage trees of several early blastula embryos. Mitotic spindles visualized with SHG and cell membranes visualized with THG were sufficient signals for analyzing cell movements and cell cycle dynamics with high spatiotemporal precision, and the authors showed a progressively amplified asynchrony in cell division based on radial position, potentially in response to maternal factors within the innermost cells of the blastoderm, is adequate to explain the origins of asynchronous cell divisions, in contrast to previously suggested dramatic switch from a synchronized to a pseudo-wave pattern of division.

1.4.6 Raman-based CARS and SRS

Raman scattering is inelastic light scattering in which light that interacts with a molecule gains or loses energy that corresponds to vibrational energy levels of the molecule. This phenomenon happens spontaneously only rarely, but use of coherent light can stimulate the process to occur at high enough rates for imaging (121, 122). Two such approaches, Coherent Anti-Stokes Raman Scattering (CARS) microscopy and Stimulated Raman Scattering (SRS) microscopy are emerging as important tools for label-free imaging that also retain molecular specificity at the level of the chemical bond that dictates a particular vibrational mode (123, 124).

Lipids are common targets for Raman-based techniques. Chien et al. demonstrated imaging of the fat-body that provides a source of energy for *Drosophila* embryos during metamorphosis with a combined CARS-2PM system (125). CARS has also been used to screen for mutant phenotypes that affect general lipid metabolism in *C.elegans* (126) and a more recent implementation of SRS using a broadband source demonstrated the capability to differentiate lipids (including cholesterol, stearic acid, and oleic acid) in *C.elegans* (127). By introducing the ability to image specific lipids, CARS and SRS open a new, very unexplored dimension of embryonic development.

2. ULTRASHORT PULSE MICROSCOPY*

2.1 Light-matter interactions

Having surveyed both linear and nonlinear imaging techniques applied to imaging embryonic development, we should briefly discuss what differentiates them in physical terms, as both are used in Ultrashort Pulse Microscopy (UPM). In general, the electric field of light passing through a material can interact with the constituent molecules by perturbing the distribution of their electrons, causing a time-varying polarization of the molecules (Fig 2.1A). Each material has its own propensity, i.e. susceptibility, χ, to be polarized by light, which affects how it will convert the incoming light into a detectable signal, with nominal intensity incident light required to drive linear polarization modes and higher intensity incident light required to drive nonlinear polarization modes (Fig 2.1B). This relationship between the incident electric field of the light, *E(t),* and the polarization, *P(t),* that is the source of new optical signals, is linked by χ and can be written mathematically (Fig 2.1C). The first term in the right side of this equation has the first order-susceptibility, $\chi^{(1)}$, which gives rise to the signals used in linear microscopy techniques. Familiar optical phenomena such as scattering and absorption are derived from $\chi^{(1)}$. Higher order susceptibility terms are responsible for signals used in nonlinear microscopy techniques such as second harmonic generation, $\chi^{(2)}$, and two-photon absorption, $\chi^{(3)}$. A more detailed list of optical signals available as potential image contrast mechanisms is given in Fig 2.1C.

---

*Part of this section is reprinted with permission from *Imaging embryonic development with ultrashort pulse microscopy* by Gibbs HC, Bai Y, Lekven AC, & Yeh AT (2014) *Optical Engineering* 53(5):051506. doi: 10.1117/1.OE.53.5.051506.

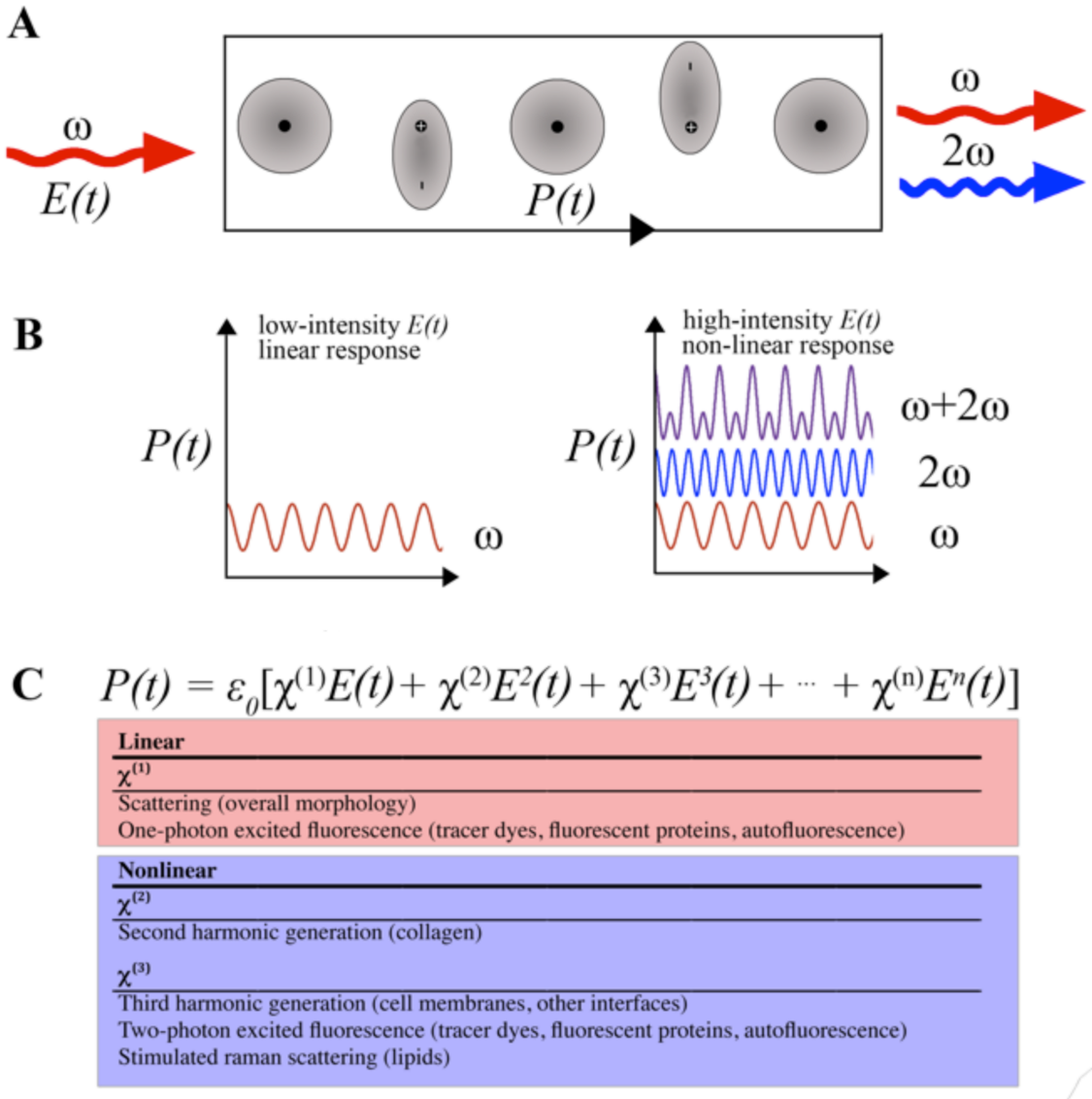

Fig 2.1 Signal diversity arising from linear and nonlinear light-matter interactions. (A) The electromagnetic field of light, *E(t)*, interacts with a molecule by polarizing its electron cloud based on the optical susceptibility, χ, of the material. The oscillating polarization, *P(t)*, drives the generation of new frequencies of light that can be used as signals for imaging contrast. (B) Low intensity electric fields drive the oscillating polarization in a linear mode while higher intensity electric fields can induce nonlinear modes of oscillation. (C) The optical susceptibility, χ, has linear and nonlinear orders that that contribute to the polarization of the molecule in the presence of an electric field. Each order of the susceptibility arises from unique properties of the material that can be exploited to generate signals for imaging embryos during development.

2.2 Linear imaging techniques ($\chi^{(1)}$)

An imaging technique is linear when the signal used to create the images comes from a linear light-matter interaction. Two common linear signals are linearly scattered light and one-photon excited fluorescence. Linear light-matter interactions have a high probability of occurring, so lamps that provide relatively low power, incoherent illumination can be adequate light sources and CCDs can be used as detectors. However, to generate higher signal to noise ratios, linear imaging arrangements can use coherent sources such as continuous-wave or pulsed lasers and photomultiplier tubes, which have higher photon density and detection sensitivity, respectively. The linear imaging techniques we have discussed are confocal microscopy, light sheet microscopy, and optical coherence microscopy. These techniques all provide three-dimensional resolution through different optical sectioning mechanisms and can be used for live imaging.

2.3 Nonlinear imaging techniques ($\chi^{(2)}$, $\chi^{(3)}$)

Nonlinear optical microscopy (NLOM) techniques rely on higher order interactions between light and matter that require intense fields of light generally from pulsed laser sources to generate signals that can be used to create images. The N in NLOM refers to the relationship between the input power and the output signal, and that a plot of output signal versus input power would not be a straight line. This nonlinear dependence and the fact that higher-order interactions are rare compared to linear single-photon interactions is the source of inherent optical sectioning with NLOM. It is important to note that this optical sectioning is unique from linear techniques like confocal microscopy. The difference is that with NLOM, signal is generated only at the focus in the developing embryo, in contrast to confocal microscopy, for example, where the signal is generated throughout the embryo, but only signal from the focus is collected through the pinhole. So, like SPIM, NLOM does not generate out-of-plane photobleaching.

2.4 Two-photon excitation by ultrashort pulses

Temporally ultrashort pulses, such as in the 10 fs regime, are advantageous compared to conventional 100-170 fs pulses used in 2PM applications because 1) for a given pulse energy, the peak power of an ultrashort pulse will be higher because the energy is compressed in time and 2) an ultrashort pulse necessarily contains a broader range of wavelengths that can together create two-photon transitions (128, 129). Using a semi-classical model of a two-photon transition, where the electric field is treated classically and the molecule is treated quantum-mechanically as a two-level system, this benefit can be quantified in terms of relative two-photon transition probabilities.

To compare the theoretical transition probabilities of our sub-10-fs pulses with conventional pulses, we first measured the spectral intensity, $|E(\omega)|^2$, of sub-10-fs pulses output from our Ti:Sapphire oscillator. To model the electric field, $E(\omega)$, of alternative transform-limited pulses (all frequencies arrive at the focus in phase) of varying temporal duration, τ_p, we used the Gaussian relationship shown in Eq. (1).

$$E(\omega) = \exp(-\tau_p^2 \omega^2 / 8\ln(2)) \tag{1}$$

Two-photon transitions can occur through degenerate and non-degenerate mixing of frequency components, so if the pulse is transform-limited, then all possible combinations of the frequencies within the pulse can be given by the two-photon excitation power spectrum (130), $T(\omega)$, described by Eq. (2).

$$T(\omega) = \left| \int_0^\infty E(\omega/2 + \Omega) E(\omega/2 - \Omega) d\Omega \right|^2 \tag{2}$$

The two-photon excitation spectrum of our sub-10-fs pulse is compared to that of a 100 fs pulse in Fig 2.2A. In the context of imaging embryonic development, molecules of interest generally have a frequency-dependent response, sometimes called a two-photon action cross-section (131). To meaningfully compare the theoretical performance of these pulses, this response must be known. The yield or transition probability (132, 133), Γ, then, is the overlap integral of $T(\omega)$ and the frequency response of the molecule, $\gamma(\omega)$, as shown in Eq. (3).

$$\Gamma \propto \int_{-\infty}^{\infty} T(\omega)\gamma(\omega) d\omega \tag{3}$$

From Eq. (3) it can be seen that the probability of a two-photon transition depends on the magnitude of the area under the two-photon power spectrum curve and the degree to which this overlaps with the absorption lineshape of a given fluorophore. We used $\gamma(\omega)$ measured from the commonly used enhanced green fluorescent protein (eGFP) (134) to calculate transition probabilities for our sub-10-fs pulses centered at 800 nm and from 100 fs pulses centered at 940 nm, the maximum of the eGFP frequency response, illustrated in Fig 2.2B. We calculated a 5-fold enhancement of yield in the case of un-tuned, sub-10-fs pulses compared to optimally tuned 100 fs pulses given the same pulse energy. In terms of imaging embryonic development, this enhancement could be used to image more rapidly or alternatively, to decrease pulse energy to reduce stress on the developing embryo.

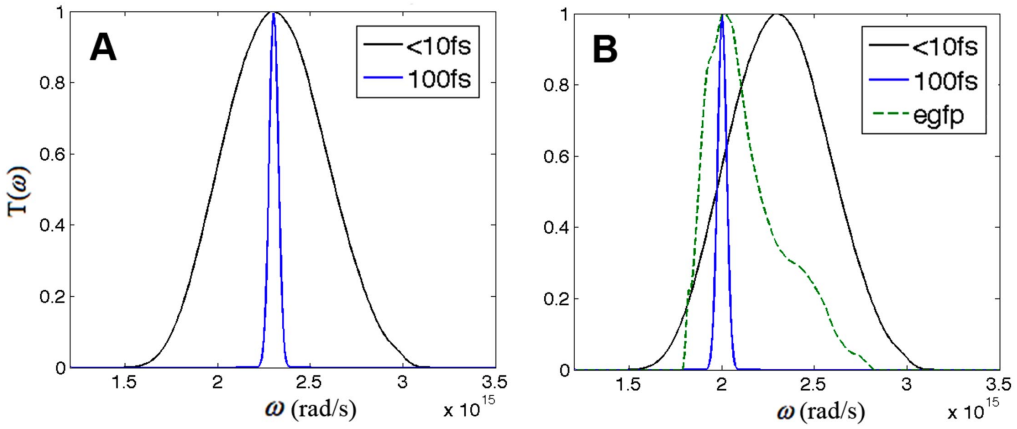

Fig 2.2 Advantage of using ultrashort pulses in 2PM. (A) Two-photon power spectra, T(ω), for 10 fs (black line) versus 100 fs (blue line) pulses with the same pulse energy centered at 800 nm. The area under the curve represents the ability to create two-photon transitions in materials with frequency independent response, γ(ω). (B) T(ω) for 10 fs (black line) pulses at 800 nm and 100 fs pulses (blue line) tuned to 940 nm, the maxima of γ(ω) for green fluorescent protein (GFP) (dotted green line). The ability to create two-photon transitions for GFP, where the response is now frequency dependent, is the overlap integral of T(ω) and γ(ω), which is five times greater in the case of un-tuned, transform-limited pulses at 10 fs pulses at 800 nm versus optimally tuned 100 fs pulses.

For imaging multiple fluorescent protein variants simultaneously, the advantage of using sub-10-fs pulses increases. A single narrowband source will necessarily be tuned to a compromised wavelength that interacts with the frequency responses of the different molecules, decreasing the yield for each, while the sub-10-fs pulse interacts substantially with each simultaneously (135, 136). Thus, with ultrashort pulses, it may be more feasible to image multiple genetically marked lineages during embryonic development.

2.5 Coherence gating with ultrashort pulses

The benefits of utilizing the short coherence length of ultrashort pulses to improve axial resolution of OCT/M are well known (137). Using Fourier-domain detection, the frequency components of the interferogram produced by the sample and reference arms encode the spatial profile of the biological sample along the optical axis (A-line) within the confocal parameter of the imaging objective (83). Rapid imaging can be achieved by scanning this A-line across the sample in two dimensions. Thus, for OCT imaging a low numerical aperture (NA) objective resulting in a large depth of field is desirable, so long as the diffraction-limited lateral resolution remains comparable to the axial resolution, Δz (138), which depends on the source frequency bandwidth at full-width-half-maximum (FWHM) as shown in Eq. (4).

$$\Delta z = \frac{2(\ln 2)}{\pi} \frac{\lambda_0^2}{\Delta\lambda} \tag{4}$$

Our sub-10-fs pulses have a FWHM of 133 nm centered at 800 nm, corresponding to a theoretical axial resolution of 2.12 μm, whereas a more conventional pulse with a bandwidth of 10 nm at this central wavelength will have an axial resolution of 28 μm. This resolution difference is significant when imaging individual cells and small-scale tissue structures in developing embryos. In the context of combining OCM with 2PM, the resolution offered by use of ultrashort pulses also better matches the two-photon interaction volume resulting from a tightly focusing high NA objective so simultaneously acquired 2PM and OCM images are automatically co-registered (139).

2.6 Instrumentation

Our multi-modal UPM system, summarized in Fig 2.3 and shown schematically in Fig 2.4, combines 2PM and Fourier-domain OCT/M in a single platform with the option of either two-channel (with OCM) or spectral detection (stand-alone) capabilities for 2PM. Detailed more in these reports (139-141), we describe the instrument here briefly. Sub-10-fs pulses from a Kerr-lens, mode-locked Ti:Sapphire oscillator (Femtolasers, Vienna, Austria) at 800 nm central wavelength with 133 nm bandwidth (full-width half maximum) are pre-compensated using double chirped mirrors (GSM 270, Femtolasers) and coupled to the multi-modal imaging system. For combined 2PM-OCM, a 5% beamsplitter splits the beam into signal and reference arms in a Michelson interferometer configuration. The signal arm is coupled using galvanometer driven mirrors (Cambridge Technology, Cambridge, MA) into an upright microscope (Axioskop2, MAT, Carl Zeiss, Thornwood, NY), expanded, and directed by a 635 nm short-pass dichroic mirror (Chroma Technologies, Bellows Falls, NY) to the back aperture of the water-immersion imaging objective (20X, 1.0 NA or 40X, 0.8 NA, Carl Zeiss) which focuses the pulses to a diffraction-limited spot that is scanned in the x-y plane across the sample. Backscattered near-infrared light is collected by the imaging objective and reflected back to the beamsplitter where it recombines with the reference arm and is coupled into a single mode fiber and sent to a home-built spectrometer consisting of a collimating lens, reflective grating (1200 lines/mm), collimating lens, and CCD array (Basler, Exton, PA). Dispersion is matched in the reference arm using a combination of a prism pair and BK7 glass. For OCM, the interferogram obtained from each pixel is integrated into a single intensity value to build up a 256 x 256 2-D image rendered *en face*. Simultaneously, 2PM signals are collected by the imaging objective and directed onto two PMT detectors (Hammamatsu, Bridgewater, NJ) using appropriate dichroic mirrors and bandpass filters (Chroma). Photon counts are saved as intensity values.

For spectral 2PM, the 2PM signals are collected by the imaging objective and coupled into a multimode fiber and sent to a home-built spectrometer consisting of a collimating lens, diffraction grating (700 lines/mm), collimating lens, and a 16-channel multi-anode PMT array (Hammamatsu). 3-D images

are built up by translating the sample in the z direction along the optical axis. Instrumentation control and data acquisition are performed using custom LabVIEW software (National Instruments, Austin, TX).

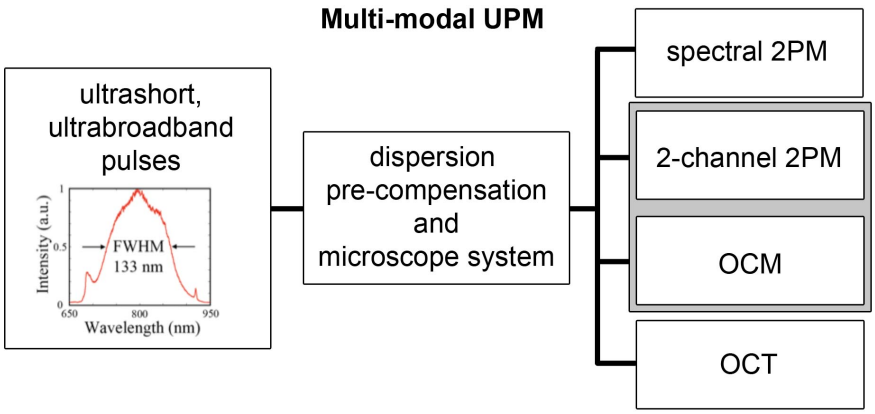

Fig 2.3 Multi-modal Ultrashort Pulse Microscopy (UPM). A single oscillator outputting 10 fs pulses centered at 800 nm at 80 MHz is coupled to a microscopy system with several detection modes. Pulses are pre-compensated for 2nd order dispersion introduced by the microscopy system with double chirped mirrors.

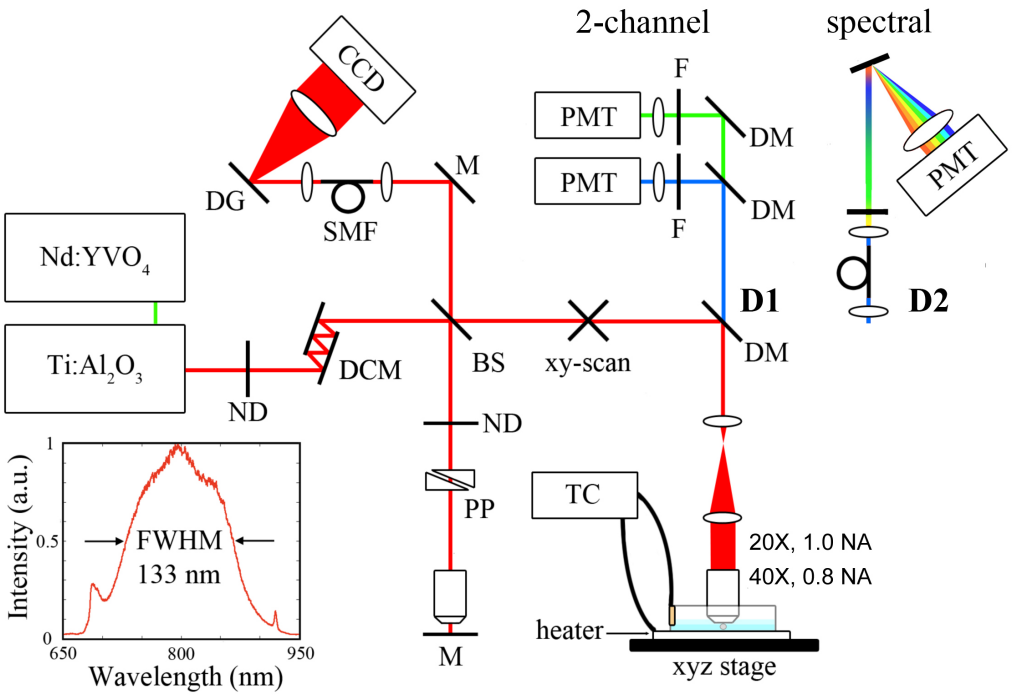

Fig 2.4 Schematic of Ultrashort Pulse Microscopy (UPM). 10 fs pulses from a mode-locked Ti:Sapphire laser are dispersion compensated and coupled into a combined platform for detecting optical coherence signals and two-photon excited fluorescence signals via two-channel or spectral detection. ND-neutral density filter, DCM-dispersion compensating mirror, BS-beam splitter, PP-prism pair, M-mirror, DM-Dichroic mirror, F-filter, PMT-photomultiplier tube, SMF-single mode fiber, DG-diffraction grating, TC-temperature controller, lp-long pass, sp-short pass, NA-numerical aperture.

3. IMAGING EMBRYONIC DEVELOPMENT WITH UPM*

3.1 Background

As we have discussed, embryonic development is the shaping of a single cell into a functioning organism through the interdependent forces of cell proliferation, migration, and genetic specification. Our understanding of embryonic development represents a conceptual synthesis of what has been shown through many different types of direct and indirect experimentation, enabled by the evolving experimental tools available to developmental biologists. Transplantation technology allowed the astounding discovery of the developmental organizer (142), mutagenesis uncovered many key developmental genes/networks (143, 144), genomic sequencing revealed unexpected levels of evolutionary conservation in the development of the animal body plan (145, 146) and together with the discovery of fluorescent proteins (147, 148) has enabled the construction of genetic reporters for labeling and tracking specific populations of cells in developing embryos (149). These discoveries have helped us begin to understand the origin of birth defects ((150)), the interplay of genetic and environmental factors during development (151, 152), and how to genetically program clinically important cell types for regenerative therapies (153-155). At the foundation of this process of discovery is visualization, a function of contrast mechanisms and the ability to meaningfully capture them. Consequently, progress in understanding embryonic development and downstream clinical application of that basic knowledge is intimately tied to progress in imaging technology.

The events of embryonic development can be briefly summarized as follows, to emphasize the demands on an imaging system that would attempt to directly capture them. When an egg (a zebrafish egg is approximately 600-700 um in diameter (156, 157) is fertilized, the resulting embryo begins a stage of rapid cell division (15-30 minutes per division (120)) known as the cleavage stage. Toward the end of this stage, the embryo transitions from relying on pre-existing molecular cues deposited in the egg to utilizing

---

its own genomic machinery (thousands of genes (158, 159)) and shortly thereafter, the three germ layers are distinguished during the process of gastrulation where rapid cell movements (several μm/min (74)) accompanied by spatiotemporal varying patterns of gene expression result in recognizable anterior-posterior and dorsal-ventral embryonic axes. Continued cell proliferation, slowed cell movements (~0.5 μm/min), and further refinement of gene expression then shape the body plan composed of segments of appropriately fated cell lineages (now tens of thousands of cells (74)). From this point, within each segment, cells differentiate and take on specific morphologies and functions as individual organs mature. Perhaps not surprisingly, despite a detailed framework and list of components, these events as a whole have yet to be fully observed or understood.

Each aspect of embryonic development, then, presents unique challenges. Its dynamism requires imaging to be non-destructive and preferably non-invasive. Its fundamental unit is the cell, but sub-cellular events, such as cell division and mitotic spindle orientation, are vital to proper embryonic development, as are collective cell behaviors behind tissue and organ morphogenesis. Adding to the complexity is the daunting number of genes involved that have disparate spatial and temporal expression patterns. All this activity occurs over a relatively large 3D space, placing further demands on imaging capabilities. The challenge to modern imaging systems, then, is to rapidly and non-invasively acquire large, high resolution, multi-channel volumetric images from a live developing embryo (1).

Toward this goal, two-photon microscopy (2PM) has become favored over one-photon approaches because of the advantages of near-infrared (NIR) light, including 1) less photodamage to embryos allowing longer time-lapse imaging sessions, 2) less scattering allowing imaging deeper into embryos, especially more opaque embryos, and 3) the option of simultaneously exciting multiple fluorescent species in the biological window (400-700 nm) without the excitation light (750-1000 nm) interfering with imaging signals (94). As 2PM techniques have become more widespread, so has ultrafast laser technology, with most imaging systems typically employing pulses from a Ti:Sapphire oscillator with a temporal duration of 100-170 fs (91, 160). Despite the advantages gained by adopting 2PM,

however, it has remained challenging to acquire high-resolution, 3-D multi-channel movies of embryonic development.

Microscopists are well acquainted with the trade-offs encountered when attempting to optimize imaging parameters due to a photon economy that is limited by an organism's tolerance of the probing light radiation. For example, to increase imaging speed to capture more rapid cell movements during embryogenesis, narrowband NIR pulses will generally be tuned to the optimum 2P absorption peak of a single fluorescent marker and all emitted light will be collected as a single channel (103). This approach provides "in toto" characterization of cell proliferation, death, and migration, but provides little information about the shaping of the embryonic tissue and none about the genetic specification of cells. With a transition from single-point scanning to line-scanning the excitation light source, as in digital scanned light sheet microscopy (DSLM), it is possible to add another channel (161, 162). However, imaging two or three genetic markers in 4-D (space, time) is the current technological limit (113, 163), while the genetic regulatory networks governing embryonic development contain vastly more components.

Optical coherence tomography/microscopy (OCT/M) is a linear imaging technique that images the morphology of biological samples based on changes in index of refraction that frequently also employs NIR laser pulses (81). Because of the high sensitivity of the interferometric detection scheme employed in OCT/M, this approach has been used to image extraordinarily fast movements during embryogenesis, such as heart tube pumping and development (164, 165). Alternatively, because of the enhanced penetration of both the input and output NIR signals, OCT has also been used for longitudinal imaging of mouse embryos in utero, where the uterus is temporarily dissected from the mother (166). Since 2PM and OCT/M can be relatively easily integrated into a multi-modal platform, it would be interesting to explore potential applications of OCT/M to additionally render molecularly specific signals in the context of embryonic development. NBT/BCIP is a robust and strongly scattering precipitate that is commonly used to mark domains of gene expression through a standard immunohistochemical technique called in situ hybridization (ISH) (167). Though ISH requires embryos to be fixed, it provides fundamentally unique data from 2PM approaches that track fluorescent protein markers because it provides a more accurate view

of gene transcript localization at a specific developmental stage. Such data will be complementary to that obtained by time-lapse 2PM while also being relatively easily obtained with the same imaging platform.

In the previous section, we have presented the theoretical benefit of using ultrashort pulses, on the order of 10 fs, for imaging embryonic development. In this section, we demonstrate this benefit manifest as unique capabilities for exciting and rendering a wide variety of optical signals from developing embryos simultaneously. In addition, we demonstrate these capabilities in a system where dispersion compensation is implemented in a relatively simple and user-friendly manner using double chirped mirrors (140). Our multi-modal instrument can be used for 2PM (and other forms of nonlinear optical microscopy such as second harmonic generation) with both standard two-channel detection or with spectral detection, as well as for OCM, and we refer to these techniques collectively as ultrashort pulse microscopy (UPM). Within a single experiment, UPM provides the opportunity to better link the behaviors of genetically labeled cell lineages with the morphogenesis of tissues and organs during development. In addition, while UPM still only scratches the surface of embryonic development in its entirety, it does have the potential to provide more information from a single experiment than other approaches, which could enable a more accurate construction of systems-level views of vertebrate development by combination of data sets onto dynamic digital atlases (68, 69, 168).

3.2 Materials and methods

3.2.1 Label-free imaging of fixed and live wild-type embryos

Zebrafish were maintained and bred according to standard protocols (169). For imaging, wild-type embryos were treated with 0.003% (w/v) phenylthioluria (ptu) to suppress the formation of pigment cells (except for label-free imaging of melanocytes) and mounted in 1.2% low-melt agarose hydrated with Instant Ocean (United Pet Group, Blacksburg, VA). Live wild-type embryos were imaged at 25°C, with time-lapse imaging performed at 27°C at 15-30 minute intervals. In some cases, embryos were fixed in 4% (w/v) paraformaldehyde overnight at 4°C and stored in phosphate buffered saline (PBS) before imaging.

Average power of the excitation beam was attenuated to 25-30 mW on the sample (not accounting for scattering due to the agarose embedding) and pixel dwell time ranged from 120-480 μs. In most cases, lateral resolution was limited by digital resolution but kept on the order of 1-2 μm, while axial step size was generally 3 μm, as recommended (76) to capture all cells in the imaging volume. Signals were collected into a single channel using a BG38 filter (Schott, Elmsford, NY).

3.2.2 Imaging transgenic embryos

Stable transgenic lines expressing eGFP under a *wnt1* regulatory element that recapitulates *wnt1* expression in the midbrain and at the midbrain-hindbrain boundary (170) were used to demonstrate time-lapse imaging of genetically labeled cell lineages in live zebrafish embryos. Transgenic fish were intercrossed and embryos imaged during the segmentation period of development as described above, with stacks acquired at 15 minute intervals. Autofluorescence and eGFP signals were separated with a 490 nm long-pass dichroic mirror (Chroma) and further discriminated with 450/60 and 525/50 nm band-pass filters (Chroma) respectively. For demonstrating excitation and spectral detection of a variety of fluorescent protein variants within zebrafish embryos using ultrashort pulses, wild-type embryos were injected at the 1-cell stage with plasmid DNA containing a fluorescent protein gene (eBFP2, CFP, mOrange, and mRFP) or a fluorescent protein fusion (citrine-H2B) under a cmv promoter resulting in mosaic expression throughout cells of the embryo at 24 hpf. For acquiring spectral images of eGFP, the aforementioned stable transgenic lines were used. Embryos were imaged at 24 hpf and fluorescent signals were collected with the spectral detection scheme described in Section 2.

3.2.3 In situ hybridization and imaging NBT-BCIP with 3-D resolution

In situ hybridization was performed as previously described (21) for either *krox20* or *egfp* mRNAs. Embryos stained with NBT/BCIP and hydrated in PBS were mounted as described above and imaged in the combined 2PM-OCM modality with an average power of 35 mW on the sample (not accounting for scattering due to the agarose embedding), a pixel dwell time of 480 μs and step size of 3 μm.

3.2.4 Image processing

Images were processed using custom Matlab routines and openly available image processing software ImageJ and FIJI (171). 3-D, multi-channel reconstructions were rendered in V3D (172). Nuclear segmentation from autofluorescence signal was performed manually.

Spectral unmixing was performed with custom Matlab routines that utilized spectral standards of the components to be unmixed (obtained online from Invitrogen, Molecular Probes or measured experimentally). The algorithm creates a set of fits, $F(\lambda)$, that are the linear weighted sum of n scalar coefficients, c_i, and 16 element reference spectra, $R_i(\lambda)$, of n presumed constituents, as shown in Eq. (5)

$$F(\lambda) = \sum_{i=1}^{n} c_i R_i(\lambda) \tag{5}$$

The solution is the set of positive coefficients that sum to 1 and produce a fit that minimizes the mean squared error between the fit and measured spectra.

3.3 Results and discussion

3.3.1 Label-free imaging of embryonic tissues

To determine whether endogenous fluorescence could be used to image vertebrate development, we imaged wild type zebrafish embryos free of exogenous labels with 10 fs pulses centered at 800 nm. The zebrafish, also known as *Danio rerio*, is a well-characterized and established model organism especially useful for time-lapse imaging analysis of developmental mechanisms (156).

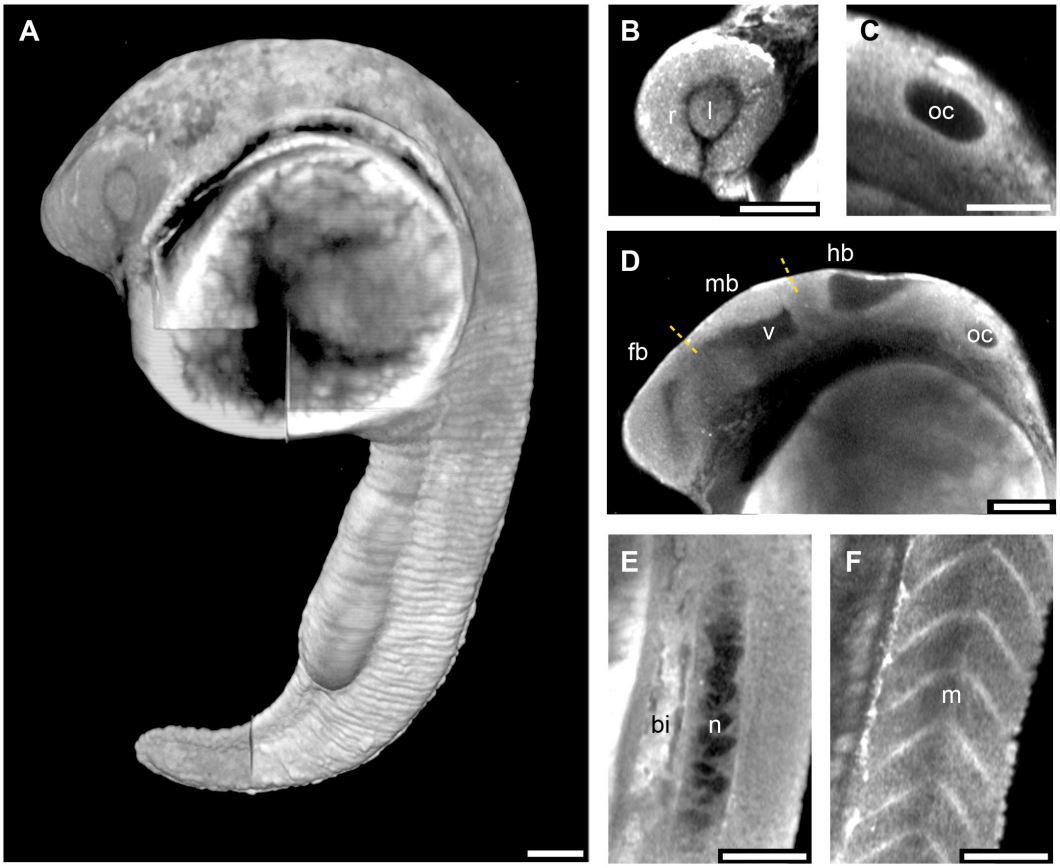

Fig 3.1 Label-free imaging of embryo and organ morphology with UPM. (A) Lateral view of a volume rendering of endogenous signals excited by ultrashort pulses in a zebrafish embryo at 24 hours post fertilization (hpf), also referred to as the prim-5 stage. Image is the product of fusing 9 different volumes. (B-F) Optical sections of the same embryo detailing various forming organs including (B) the eye, composed of the lens (l) and retina (r) (C) the developing otic cup (oc), (D) different brain segments including the forebrain (fb), midbrain (mb), and hindbrain (hb) and ventricular spaces (v), (E) trunk region including notochord (n) and blood islands (bi), and (F) more laterally in the trunk region, myotome (m) or muscle segments. Scale bars are 100 μm.

We first examined embryonic development at the tissue level. At 24 hours post fertilization (hpf), the major organ systems in zebrafish embryos have taken on a recognizable morphology according to the basic vertebrate body plan, so we imaged a fixed embryo in its entirety using overlapping fields of view to observe those features visible from endogenous fluorescence. The combined image rendered using FIJI volume viewer is shown in Fig 3.1A.

We observed strong autofluorescence signal from most tissues in the embryo and developing structures were easily visible in optical sections including structures of the eye, ear, developing brain and ventricular system, notochord, blood islands, and muscle segments (Fig 3.1B-F). These data illustrate that ultrashort pulses efficiently excite autofluorescence from the constituent cells of the embryo such that the morphogenesis of a wide variety of organ systems can be characterized quantitatively without the need for exogenous labels. Such data will be useful for the re-emerging field of physical biology that seeks to model the mechanical forces that give rise to embryonic shape (48, 173), and potentially connect these forces to specific cell behaviors and patterns of gene expression.

3.3.2 Label-free imaging of individual cells and their movements

We were also interested to determine whether cellular autofluorescence signal was sufficient for tracking individual cells, so we performed time-lapse imaging of the cranial region of zebrafish embryos during the segmentation period, when neural crest cells are derived from the roof plate of the neural tube and migrate to give rise to different structures and cell types in the embryo, including craniofacial cartilage and bone, melanocytes, and peripheral sensory neurons (174). As seen in Fig 3.2A and B, these neural crest cells generally originate from the dorsal side of the densely-packed neuroepithelium and migrate laterally and ventrally into a less-dense mesenchyme outside the neural tube. In this mesenchyme, individual neural crest cells were easily visible from autofluorescence signal and demonstrate that UPM could potentially be utilized to track the dynamic migration of different populations of neural crest i.e. produce a high-resolution neural crest fate map independently of exogenous cell labels.

We also decreased the field of view to match our digital resolution to the diffraction-limited performance of the system to assess the possibility of imaging individual cells within the tightly-packed neuroepithelium at 24 hpf. At this time in development, the neuroepithelium is a contorted tube, pseudo-stratified with the apical side in contact with the brain ventricular system and the basal side facing outward. Fig 3.2C shows a cartoon of this arrangement from a dorsal view, where the anterior portion of the head is directed to the left. The neural tube has been segmented into morphologically distinct regions

including the forebrain (fb), midbrain (mb), and hindbrain (hb). The boundary between the midbrain and hindbrain is referred to as the midbrain-hindbrain boundary (MHB) organizer (the term organizer denotes the importance of this region for correct development of structures in the midbrain and hindbrain such as the tectum, tc, and cerebellum, cb, respectively). Fig 3.2C' shows autofluorescence from an optical section taken from this boundary region on the right side of the embryo. The large dark portion of the image in the bottom left corresponds to the fluid-filled brain ventricle while other dark spots correspond to individual cell nuclei. Fig 3.2C'' is the same image inverted and marked to show the arrangement of individual cell nuclei in yellow and the outline of the neuroepithelium in blue. We were able to image a unique region of the epithelium at the boundary where a group of cells seems to have recaptured the character of a simple one-layer epithelium with the nuclei aligned rather than staggered. This particular arrangement may provide some structural support to the MHB constriction as the tectum and cerebellum rapidly develop on either side. We have also observed that this group of cells can be identified as part of the *wnt1* lineage (see figure on p. 48). While there is a significant literature concerning the genetic basis underlying the structure and specification of this region (175), there is relatively little known about how these genes direct individual or collective cell behaviors that achieve this complex tissue architecture.

The autofluorescence signal we detect arises predominantly from pyridine nucleotides and flavins found in the mitochondria and cytoplasm whose 2P excitation spectra have been measured (176). While narrowband pulses can simultaneously excite key autofluorescence molecules NADH, NAD(P)H, FAD, and lipamide dehydrogenase, we have not seen reports of these signals used to measure tissue morphology and cell movements over time in embryonic development. It may be that for a given pulse energy, ultrashort pulses provide a significant enhancement over conventional pulses such that the autofluorescence is transformed from unwanted background noise to a label-free method to integrating the cellular and tissue scale dynamics of development.

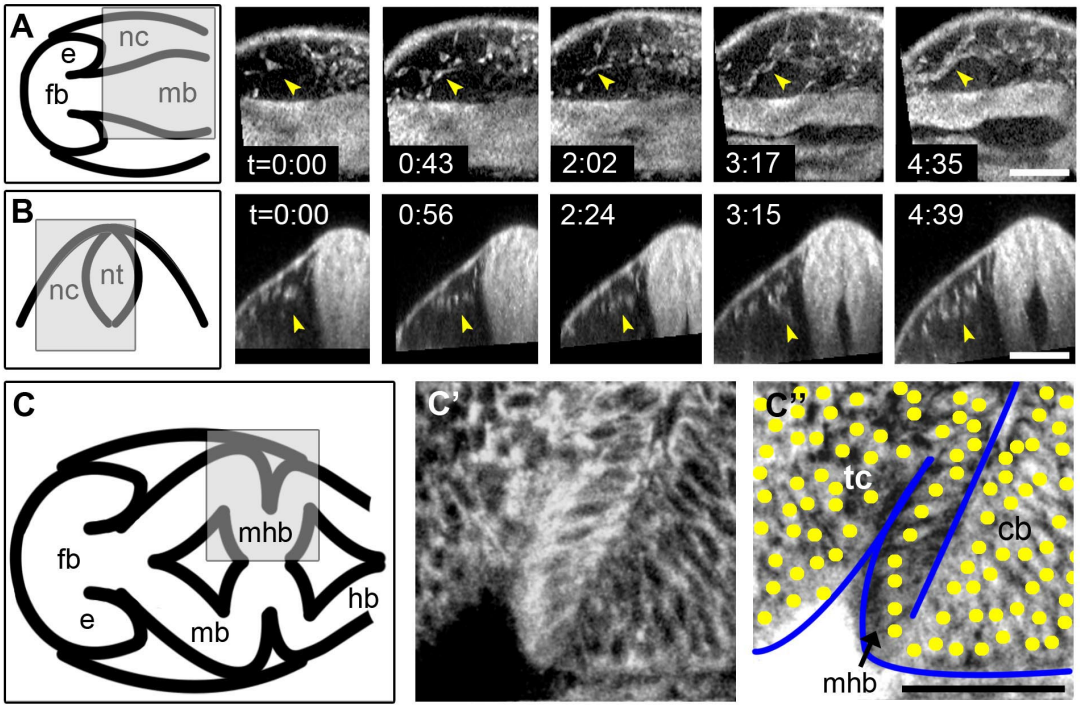

Fig 3.2 Label-free imaging of individual cells and their movements with UPM. (A) For reference, a cartoon of a dorsal view of the embryonic brain including the forebrain (fb), eye (e), neural crest (nc), and midbrain (mb). Left-right symmetry can be assumed. The rest of panel A are optical sections (x,y) depicting coordinated migration of neural crest cells in a low density mesenchyme tracked during the segmentation period of development (t=0:00 is the 10 somite stage). Images were rendered en face in this orientation (B) Cartoon depicting a transverse view of the embryonic neural tube (nt). The rest of panel B are optical sections (y,z) of neural crest cells migrating lateral to the neural tube. (C) Cartoon depicting morphology of the midbrain-hindbrain boundary (MHB) at 24 hpf. (C') Optical section of the area outlined in gray. At this stage, the neuroepithelium is stratified and densely packed, but autofluorescence excited by ultrashort pulses can still be used to identify individual cells. Nuclei, lacking endogenous fluorophores, remain dark. (C'') Different cellular organization in different brain compartments, such as the tectum (tc) and cerebellum (cb), including a special non-stratified epithelium at the MHB. Scale bars are 100 μm.

3.3.3 Label-free imaging of pigmented cells

Melanocytes, derived from the multi-potent neural crest cell linage, have been a prominent model for the study of cell differentiation and of the establishment of adult stem cell populations during development (177). We have observed strong (10-20 fold stronger than cellular autofluorescence) 2P excited fluorescence from melanocytes (commonly called melanophores in fish) as shown in a volumetric maximum intensity projection in Fig 3.3A. Live embryos that were not treated to block melanin

production were imaged at 24 hpf. We observed brightly fluorescing cells distributed throughout the cranial region underneath the periderm displaying expected differentiated cranial melanocyte morphology and positioning (174). Neural crest delamination and migration occurs with varying dynamics along the anterior-posterior axis and, at a specific spatial location, neural crest may delaminate in temporally sequential waves. For example, in the zebrafish trunk, at least two different temporal waves give rise to neural crest migration along a medial and, later, a more lateral pathway (178). In the cranial region these dynamics are not well characterized and could be significantly more complex.

Optical sections in Fig 3.3B-D reveal a striking population in the optic tectum localized at the dorsolateral hinge points of the neural tube, which appear pigmented while still integrated in the neural epithelium. This finding is unusual because melanocytes are generally thought to differentiate from melanoblast precursors that have already delaminated from the neuroepithelium (179). Some neurons, such as dopaminergic neurons, are known to be pigmented (180) but no pigmented neurons have been reported in this region of the optic tectum in zebrafish. One interpretation of this data is that ultrashort pulses provide significantly more sensitive detection of melanin than can be achieved with standard light microscopy and that, at least for a sub-population of melanocytes, differentiation occurs prior to or during the epithelial-to-mesenchyme transition. Efficient 2P excitation of melanin using conventional pulses and resulting in bright fluorescent signals has been reported in cell culture (181) and in a concentration dependent manner *in vivo* (182). It would be interesting to use a combination of autofluorescence and melanin fluorescence to track the origin and eventual fate of this unique population, although the overwhelming melanin signal would impede the addition of any fluorescent protein gene reporters simultaneously.

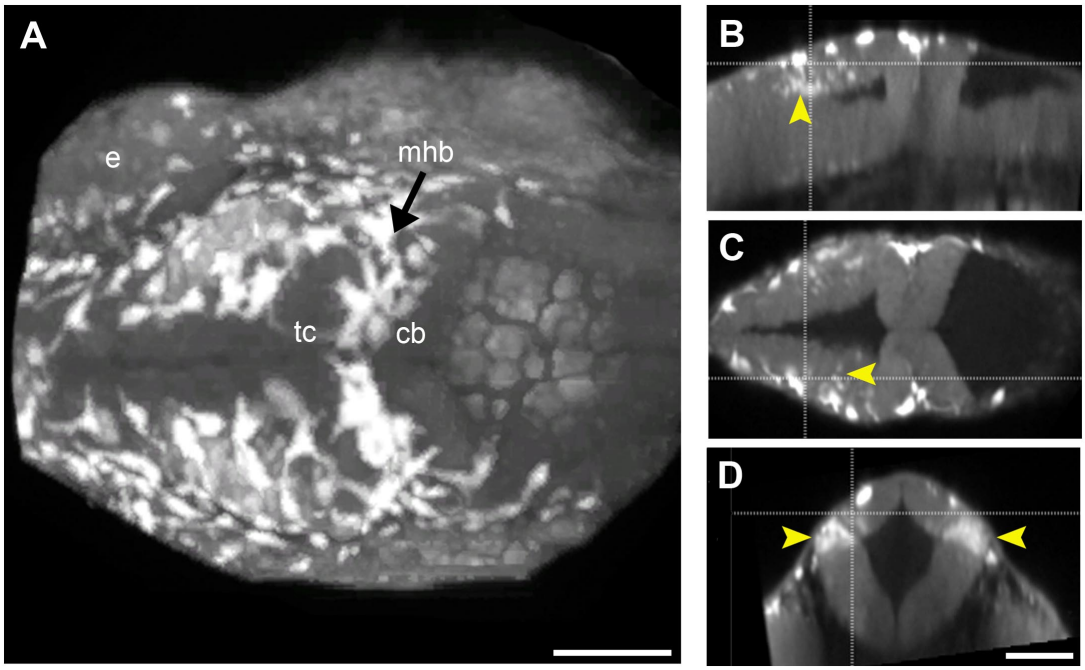

Fig 3.3 Label-free imaging of melanocytes and other pigment cells. (A) Dorsal view of a three-dimensional maximum intensity projection of the embryonic zebrafish brain at 24 hpf. At this stage, cells derived from the neural crest have differentiated into melanocytes in a characteristic pattern in the cranial region. A strong signal (4-5 fold brighter than tissue autofluorescence) excited by ultrashort pulses matches this characteristic pattern. (B-D) Optical sections (B – lateral, C - dorsal, D – transverse) from volume in A also reveal a population of pigmented cells in the neural epithelium that is localized at dorsolateral hinge points in the tectal primordium. Cells appear to be undergoing an epithelial-to-mesenchyme transition. Scale bars are 100 μm.

3.3.4 Time-lapse imaging of genetically labeled cell lineages

We next demonstrated imaging the dynamics of a genetically labeled cell lineage simultaneously with morphogenetic events in the embryonic brain. Stable transgenic embryos expressing eGFP under the control of regulatory elements from the *wnt1* gene were imaged during segmentation over a period of 12-13 hours. During segmentation, *wnt1* is expressed in the midbrain and at the MHB and is important for proper development of the region. In mice lacking Wnt1, the entire midbrain and hindbrain region (known as mes/r1) is deleted (18). In zebrafish, other Wnts have redundant roles to *wnt1*, however, loss of these Wnts in combination also results in the deletion of midbrain and hindbrain structures (20, 21). Thus, *wnt1* has an important role in the specification of these embryonic brain tissues.

Morphogenesis of the MHB region imaged with UPM progressed in step with previous reports (183). We show in Fig 3.4 the dynamics of the *wnt1*-expressing lineage in this complex structural environment of the mes/r1 region. When the MHB is initially formed, genetic determinants from either side of the boundary initially overlap and their expression subsequently sharpens. This sharpening coincides with the development of a morphologically visible constriction at the boundary by the 10-somite stage (t=0:00). We observe eGFP positive cells in the hindbrain at this stage whose fluorescence gradually diminishes, suggesting that the boundary sharpens at least in part when cells alter their pattern of gene expression in response to a still undetermined mechanism of spatial identity acquisition. At t=0:00 we also observe the *wnt1* lineage to have a longer extent along the anteroposterior axis in the dorsal neural tube than in ventral neural tube and find that this arrangement persists throughout the periods of segmentation and ventricle formation, suggesting this initially labeled lineage is proliferative but relatively stationary along the anteroposterior axis within the neuroepithelium. Intensity of the eGFP signal increases over time in cells at the boundary itself and anteriorly along the dorsal midline up to the epiphysis, indicating continuous production of reporter transcripts in these regions, which continue to express *wnt1*. At t=3:53 we also captured the epithelial-to-mesenchyme transition of a portion of the *wnt1* lineage comprising neural crest cells, marked by arrowheads. After time-lapse imaging concluded, we observed disfiguration of the tail and slight edema as expected when immobilizing zebrafish embryos with a combination of tricaine and agarose (184), but otherwise embryos continued to develop normally through larval stages.

Photobleaching by ultrashort pulses appears to be minimal as sub-populations of the *wnt1* lineage that have stopped transcribing the *wnt1* reporter (as indicated by in situ hybridization at previous stages) can be tracked for several hours despite the dilution of available eGFP molecules by cell division. As mentioned previously, ultrashort pulses do not appear to cause undue stress to the developing embryo as evidenced by normal morphological progression of the irradiated region of the embryo throughout the period of imaging and up to 7 days later. However, in the future it may be prudent to assess the damage threshold for these organisms using ultrashort pulses similar to what has been reported for *Drosophila* (185). Using a combination of markers including lethality, necrosis, and TUNEL staining, Saytashev et al.

showed that for a given signal level, shorter pulses (37 fs) resulted in less thermal damage and fewer DNA strand breaks than longer pulses (100 fs).

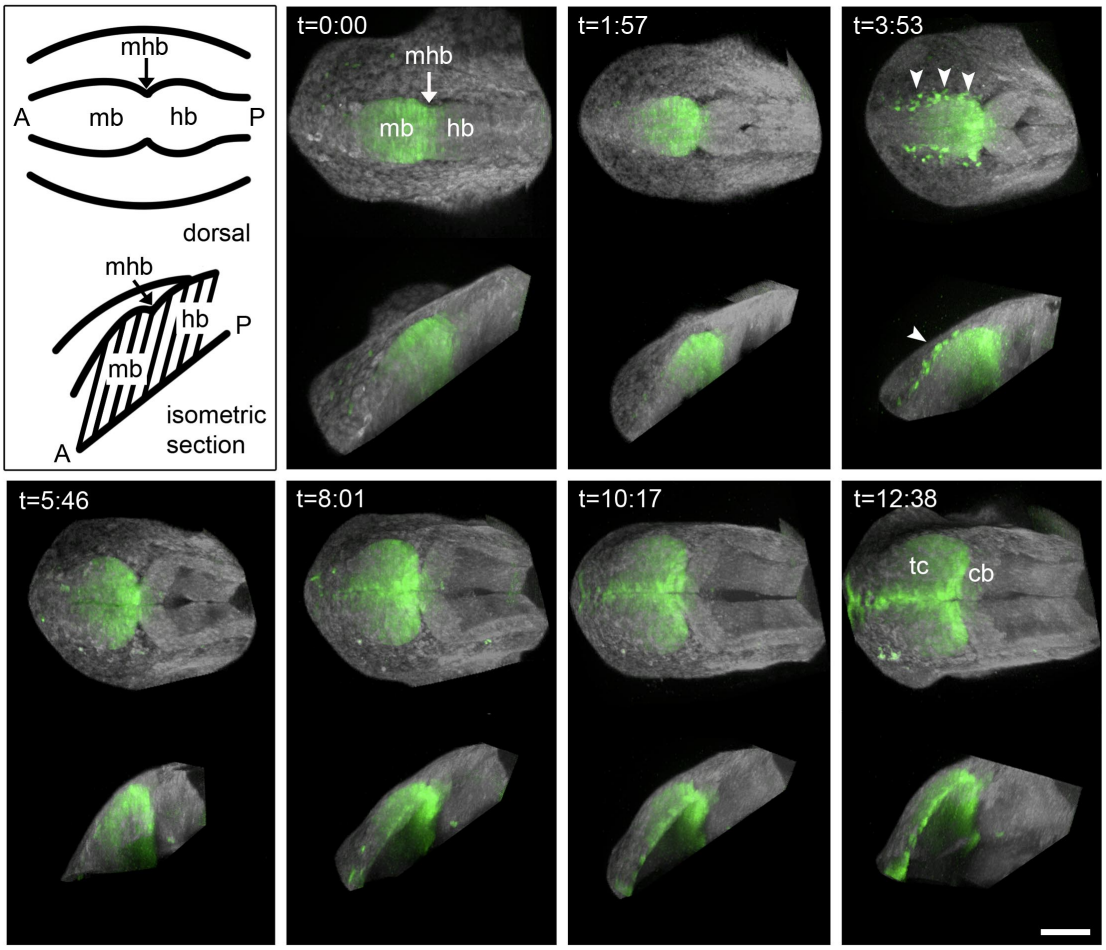

Fig 3.4 Imaging genetically labeled cell lineages in their morphological context. First panel shows a cartoon of the region of the brain depicted in subsequent three-dimensional maximum intensity projections from a time-lapse experiment on a stable transgenic line expressing eGFP protein under the control of a *wnt1* regulatory element. Time-lapse follows the midbrain (mb) and hindbrain (hb) region during the formation of the midbrain-hindbrain boundary (mhb) constriction and brain ventricle formation. t = 0:00 corresponds to the 10-12 somite stage, when the neural tube is still closed. The *wnt1* population (green) is tracked with three-dimensional resolution alongside the dramatic reorganization of neural morphology visible by autofluorescence (white). Arrows point to the migration of neural crest cells that are derived from a *wnt1* lineage. Scale bar is 100 μm.

3.3.5 Imaging a variety of labels with a single pulse source

To demonstrate the potential for capturing the dynamics of multiple fluorescently labeled genetic lineages simultaneously during embryonic development, we obtained several fluorescent protein variants and expressed them mosaically in independent zebrafish embryos through transient transgenesis. These embryos were imaged at 24 hpf using our home-built 16-channel spectral detector spanning 350 to 630 nm for capturing 2PF signals. For each pixel in a 2-D image or voxel in a 3-D image, a 16-channel lambda stack is acquired from live embryos. The average of the spectral profile for different regions in the embryos was compared to delineate autofluorescence contributions (acquired from areas of the embryo not expressing the injected fluorescent protein variant) and spectral signatures from eBFP2, CFP, eGFP, citrine, mOrange, and mRFP. Except for eGFP, the amount of plasmid injected was the same for each FP variant, thus, the relative intensity of fluorescent protein to autofluorescence can be interpreted using the 2P overlap integral among the variants with our two-photon excitation power spectrum as in Eq. 3. As expected for pulses centered at 800 nm, the overlap appears to be more significant for blue variants than for red, as seen in Fig 3.5, although other red variants such as TagRFP1 (186) have been reported to have a significant 2P action cross section near 800 nm and thus may be better suited for this application. These spectral signatures show that we can indeed efficiently excite a wide spectrum of fluorescent protein variants simultaneously, as all spectra were obtained with the same un-tuned ultrashort pulses. Once a suitable transgenic line is created, it may then be possible to image the dynamics of up to five different genetically labeled lineages.

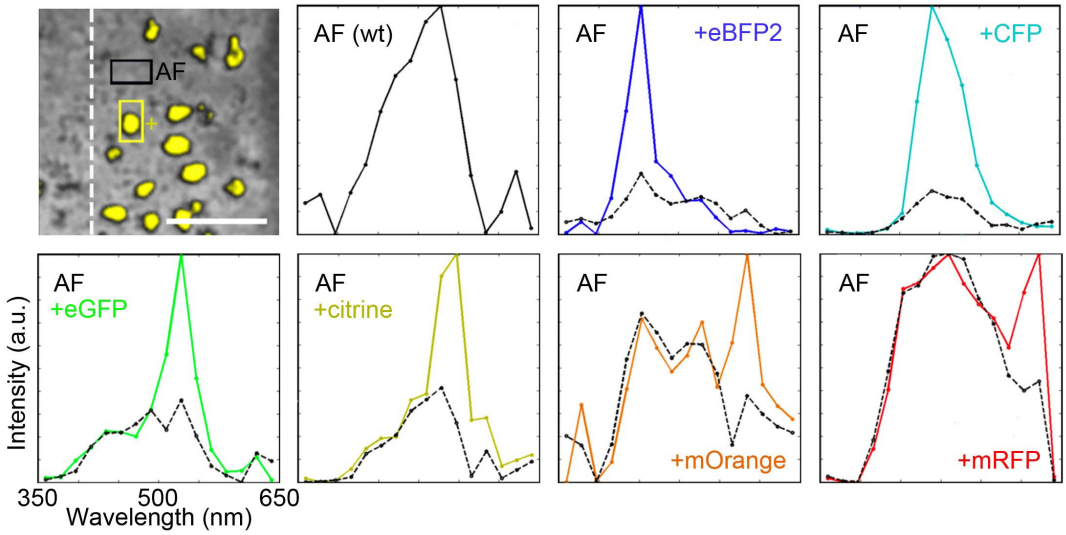

Fig 3.5 Excitation and spectral detection of fluorescent protein variants transiently expressed in zebrafish embryos. The first panel shows a representative image from an embryo mosaically expressing a fluorescent protein variant (citrine-H2B in this case, segmented and superimposed in yellow). The dotted line represents the embryonic midline, and boxes show area from which pixel-by-pixel 16-channel spectra have been summed. Subsequent graphs show the spectral data from embryos injected with different variants, spanning a range from blue to red fluorescent proteins. One spectral profile obtained from a region of the embryo with little or no exogenous label (black line) is compared to an area where the injected fluorescent protein is present (appropriately colored line). The autofluorescence (AF) contributes a broad and somewhat indistinct spectral profile while peaks from individual fluorescent proteins are readily identifiable at their expected locations. Scale bar is 50 µm.

To demonstrate the potential to accurately delineate these simultaneously excited overlapping spectral emissions, we performed spectral time-lapse imaging with simultaneous excitation of closely overlapping eGFP and citrine (a yellow fluorescent protein) emissions and separated them with linear unmixing. The unmixing algorithm assumed three constituents, 1) autofluorescence 2) eGFP and 3) citrine. Autofluorescence reference spectra were measured directly from wild-type embryos while eGFP and citrine reference spectra are available online (Molecular Probes, Invitrogen). The stable transgenic line marking the *wnt1* lineage with eGFP was injected with plasmid DNA encoding citrine-H2B at the one-cell stage resulting in differential distribution of these two fluorescent markers across the MHB at 24 hpf. Summed images are shown in the top row of Fig 3.6. Individual cells on either side of the boundary were tracked (green and yellow arrowheads) and their spectral profiles unmixed revealing the expected higher

levels of eGFP expression in the cell tracked in the midbrain (bottom row) compared to cell tracked in the hindbrain (middle row) reflected by the respective areas underneath the unmixed eGFP reference profile. Within the neuroepithelium, cells undergo interkinetic migration that is characterized by cell and nuclear movements between the basal and apical surfaces with cell division occurring at the apical side. It would be interesting to determine whether the fluorescence contribution from the citrine-H2B fusion protein, which labels nucleosomes, could be quantified as a means to track cell cycle dynamics. Intensity from the marker would presumably fluctuate as nuclear chromatin replicates and subsequently condenses prior to chromosome segregation.

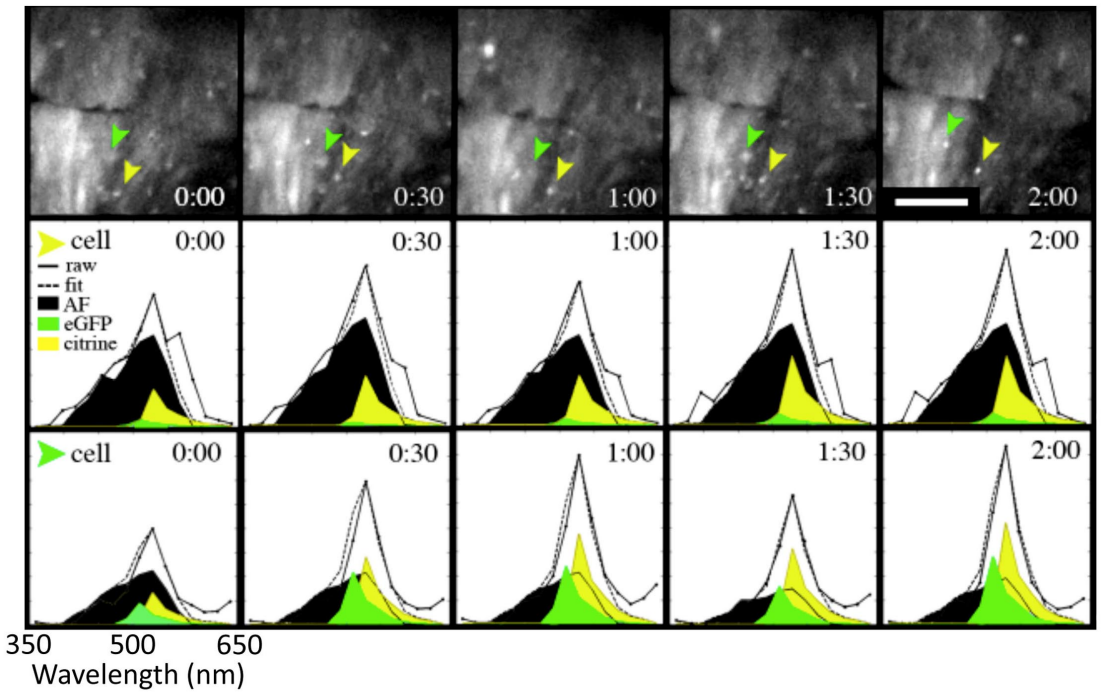

Fig 3.6 Spectral unmixing of overlapping fluorescent spectra from live cells at the MHB. Stable transgenic embryos expressing eGFP in the *wnt1* lineage were injected at the 1-cell stage with plasmid DNA containing a citrine-H2B fusion protein to mosaically mark inividual nuclei. Top row shows summed spectral image and arrowheads point to cells tracked in the midbrain (green arrowhead) and hindbrain (yellow arrohead). The spectral profiles of these cells were unmixed by varying weighting parameters for a linear sum of reference spectra (solid curves) to minimize the mean squared error between the proposed fit (dotted line) and measured data (solid line). Scale bar is 50 μm.

3.3.6 Imaging in situ hybridization with 3-D resolution

Having established that the broad 2P power spectrum of ultrashort pulses is useful for integraing molecular, cellular, and morphogenetic information in live organisms over time, we sought to take advantage of the short coherence length of such pulses to provide complementary data on mRNA transcript localization. Though fluorescent staining can be employed for transcript detection and confocal or 2PM used to image transcript localization with 3-D resolution, such protocols are notoriously fickle to the degree that many develomental biologists continue to use the more classical chromogenic precipitate, NBT/BCIP. There have been reports both of confocal imaging based on backscattering (187) and a deep red fluroescence emission (188) from NBT/BCIP for determining transcript localization in 3-D. While we were not able to detect NBT/BCIP excited with our ultrashort pulses centered at 800 nm, we were able to detect backscattered light with OCM. Simultaneous 2PM imaging of tissue autofluorescence, which is significantly quenched by NBT/BCIP, can be used to highlight domains of NBT/BCIP staining as shown in Fig 3.7A-D. Fig 3.7A shows NBT/BCIP staining marking the location of *krox20,* which is expressed in rhombomeres 3 and 5 in an easily distinguisable pattern. Fig 3.7B shows the quenching that occurs in that region. Fig 3.7C shows the OCM signal from both the tissue and NBT/BCIP stain. The overlay, shown in Fig 3.7D, highights regions stained by NBT/BCIP (low autofluorescence and high OCM signal) in red, while tissue architecture (marked by comparable OCM and autofluorescence signal) is shown in green to yellow.

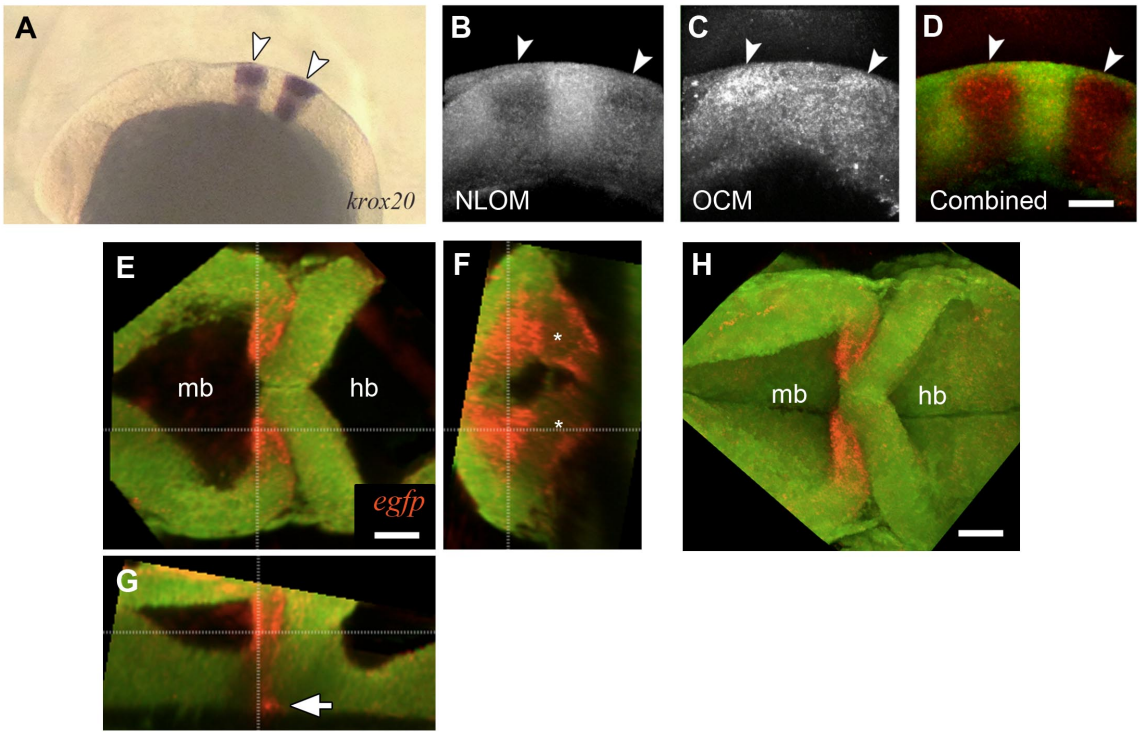

Fig 3.7 Imaging gene expression domains with multi-modal UPM. (A) Light microscopy image of an in situ hybridization where the expression domain of the *krox20* gene is marked by NBT/BCIP staining (arrowheads). Combined 2PF-OCM from this embryo shows that NBT/BCIP quenches tissue autofluorescence (B) while it enhances scattering detected by OCM (C). When these signals are combined (D), the NBT/BCIP positive domains are marked by red, while the rest of the tissue is visible as either green (low OCM signal in tissue relative to autofluorescence) to yellow (comparable OCM signal in tissue relative to autofluorescence). (E-G) Optical sections of combined 2PM-OCM using ultrashort pulses from the midbrain-hindbrain boundary, showing where *egfp* transcripts are present in NBT/BCIP stained embryos with 3-D resolution. Sections correspond to placement of cross-hairs. (E) En-face rendered image dependent on lateral resolution. Transcripts are localized to the MHB (F – transverse, G - lateral). Optical sections dependent on axial resolution. Asterisks point to characteristic lessening of staining intensity in the basal portion of the neural tube at the MHB. Arrow points to NBT/BCIP staining in the most ventral portion of the neural tube, at a depth of about 180 μm. (H) Three-dimensional maximum intensity projection of the same data set as E-G. Scale bars are 50 μm.

To demonstrate how this OCM technique can be used to complement 2PM data, we performed ISH to detect *egfp* transcripts in the stable transgenic line where eGFP is driven by *wnt1* enhancer elements and imaged those embryos with combined 2PM-OCM at 24 hpf (Fig 3.7E-H). Comparing the distribution of *egfp* transcripts versus eGFP protein revealed that a substantial portion of the *wnt1* lineage

stopped expressing the *wnt1* reporter, as suggested by tracking eGFP protein signal over time. Although this type of analysis can only be performed for a single time point in a given embryo, it will be useful for characterization of the genetic networks governing cell fate decisions during embryogenesis, as they involve not only the turning on of certain genes, but also the silencing of others.

3.4 Conclusion

We have provided both theoretical arguments and data in favor of the use of ultrashort pulses for imaging the dynamic multi-parameter mechanisms of embryonic development that begin at the molecular scale and culminate in the shaping of an entire organism. In particular, we have shown 1) the ability to image tissue morphogenesis and individual cells and their movements within developing embryos from intrinsic autofluorescence i.e. label-free, 2) the ability to simultaneously track tissue morphogenesis and genetically labeled cell lineages, 3) the ability to excite a wide range of fluorescent protein markers simultaneously for tracking multiple genetically labeled lineages in their morphological context, and 4) the ability to image mRNA transcript localization marked by NBT/BCIP staining with 3-D resolution. These capabilities, summarized in Fig 3.8, are available with a simple implementation for dispersion control, double chirped mirrors which are relatively easy to align and produce less unwanted third-order dispersion (TOD) than prism pairs (189).

In reality, it is highly unlikely we have achieved the theoretical enhancement predicted for transform limited pulses. It will be interesting in the future to implement more sophisticated pulse control methods for managing TOD and other sources of propagation time delay such as MIIPs pulse shaping (190), MEMs (191), or a grating/prism compressor (192) that could be used to tune second and third order dispersion simultaneously. Such improvements may be used to more precisely account for varying imaging conditions and biological samples, further increase imaging speed, or if needed, decrease irradiation to the embryo while maintaining the same signal level.

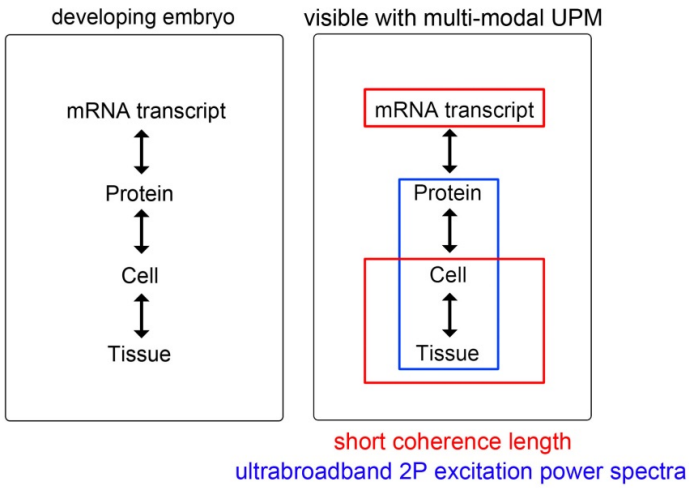

Fig 3.8 Integrated imaging of multi-scale embryonic development using multi-modal UPM. Left diagram depicts the components that drive embryogenesis in a dynamic, responsive manner. Right diagram highlights the components that can be visualized simultaneously with multi-modal UPM.

4. COMBINED LINEAGE MAPPING AND EXPRESSION PROFILING WITH UPM

It cannot be overstated enough that embryonic development is a thoroughly dynamic process, in which a combination of proliferation and programmed death, morphogenetic choreography and individual migrations, genetic programs and environmental influences intersect to grow a single cell into a living organism. Attempts to understand the interactions of these varying processes have driven advances in imaging and labeling techniques, with a push toward multi-dimensional approaches (1). However, despite recent advances in *in toto* microscopy techniques, the imaging of morphogenetic movements with their underlying gene expression remains to be demonstrated. Here, we describe the development and application of a method for combined lineage mapping and genetic profiling of tissues in the embryonic brain using integrated 2-photon excited fluorescence-optical coherence microscopy (2PF-OCM) with sub-10-fs pulses, which we have termed Ultrashort Pulse Microscopy (UPM), and image registration. Our approach to combine data from lineage mapping and in situ hybridization into the same context of live embryo morphology provides a new and more comprehensive analysis of dynamic changes during vertebrate brain development.

4.1 Background

4.1.1 Lineage mapping and fate specification

Lineage mapping techniques are used to find the dynamic address (time, place) from which specific fates (identities) arise during embryogenesis. These techniques require two capabilities: i) a method to label progenitor cells so their lineage can be subsequently traced and ii) an instrument to visualize the marked lineage within the embryo. Having only a light microscope available, some of the first lineage mapping experiments were performed by combining embryos from different color newts, so the tissues arising from the donor embryo would be easily distinguishable by eye (142). With the advent of fluorescence

microscopy, several other labeling strategies have been devised, including manual injection of fluorescent dyes, photoactivatable fluorophores (193), and transgenic strategies utilizing fluorescent proteins (108).

Transgenic strategies that rely on gene-specific enhancer elements to drive transcription of reporter genes, such as GFP, mark a lineage only once that specific gene is turned on. Thus, the lineage map gains an additional dimension of data, the role of particular gene of interest in embryogenesis. For mapping, however, a reporter necessarily must remain present in the lineage (unless the lineage is characterized *in toto*), either by means of unconditional activation (194) or by reliance on a lengthy half-life of the reporter transcript and/or fluorescent reporter protein (195). As a consequence of this stability, when a gene is transiently expressed, the reporter's presence no longer reflects the current activity of the gene of interest within its initially marked lineage. Transient gene expression arises as a normal part of development, as tissues are specified by both activation and repression of genes. Thus, this approach to lineage mapping reveals the unique *pathway* of gene activation through which a population of differentiated cells has journeyed, but does not necessarily reveal gene expression dynamics or the unique set of genes that continue to be expressed in a particular cell type. In addition, while fluctuations in the intensity of a reporter are quantifiable, interpreting these fluctuations as changes in gene expression levels can be difficult for several reasons, including a lack of characterization of the dynamics of reporter protein maturation and degradation, dilution of the reporter protein by cell division, and potential photobleaching, all processes that contribute to the amount of fluorescent protein in a cell at any given time. Yet, understanding both this history of gene expression and the genes actively expressed by a particular cell type will be important for understanding the regulatory networks governing specification (196, 197).

4.1.2 Imaging NBT/BCIP localization

In contrast to reporter protein lineage mapping, whole-mount in situ hybridization (ISH) can be used to visualize endogenous mRNA transcripts in embryos, reflecting the most current gene expression profiles of developing tissues. Because this technique requires fixation, however, it is not suitable for subsequent temporal analysis of the genetic profile in the same embryo. Rapidly maturing and unstabilized fluorescent

protein reporter variants can be used to better reflect dynamic changes in gene expression in live embryos compared to a stable lineage reporter (198), however, ISH is inherently more sensitive to gene expression and remains the gold standard for such analysis.

Chromogenic and fluorogenic approaches to ISH are common, but light microscopy of dark purple NBT/BCIP stain remains one of the most robust and widely used visualization methods for ISH in developmental biology laboratories. Unlike fluorogeneic ISH, chromogenic ISH with NBT/BCIP has not been utilized as broadly for 3-D imaging, but several reports have shown NBT/BCIP can be imaged with 3-D resolution. Confocal reflectance microscopy has been used to image NBT/BCIP staining in 3-D (187), and previously unknown red fluorescence of the stain has also been characterized (188). As OCM, like confocal reflectance microscopy, relies on detecting backscattered light from biological samples (138), we have investigated its potential in combination with 2PF as another useful technique to image NBT/BCIP with 3-D resolution.

4.1.3 Data registration using morphological landmarks

Since lineage reporters can be imaged live, but precise domains of gene expression can be imaged only after fixation, to compare these data to each other requires image registration, even when they are acquired from the same embryo. Much work has been done to develop registration techniques for medical images acquired by modalities such as CT, MRI, PET, and ultrasound (199-201) that has been recently extended to microscopy images (202-204) including 3-D images of model organism embryos (205). Specifically, nonrigid or elastic registration techniques (206) have been of interest for correcting motion or pressure artifacts from live imaging for diagnostics and image-guided intervention (207, 208), merging data sets acquired from different samples to generate virtual models and atlases (69), and, as in our present case, merging data sets obtained from the same sample under different conditions and with different detectors (209).

The ideal registration tool for this application will be familiar to the biology community, will be open-source, may be operated cross-platform, will perform registration on 3-D image stacks, and will

require minimal computational time. One such tool is found in the image processing software package FIJI, an extended version of ImageJ, with a system for review and submission of custom plugins (171). The plugin "Name Landmarks and Register" allows users to easily mark correspondences in two data sets and register one onto another. Both rigid and nonrigid registration can be performed with this plugin, but as there were considerable deformation between our data sets, we chose to apply and evaluate a nonrigid registration algorithm based on thin-plate splines, radial basis functions that model a thin metal sheet (210). To interpolate deformations, chosen landmarks were constrained to perfect correspondence and, away from these landmarks, the transformation minimized the "bending energy" of the metal sheet. This approach has the advantage of requiring relatively few landmarks, resulting in tractable computation times, and has been widely applied to study neuroanatomy (211-213), and thus should be suitable for registering gene expression data onto live lineage tracing data in the early zebrafish brain.

4.1.4 Midbrain-hindbrain patterning

Nervous system patterning may be a particularly suitable biological system for combined lineage mapping and fate profiling analysis. During segmentation, the divisions of the early brain are marked by unique expression of genes overlapping at presumptive boundaries that are subsequently refined to sharp abutting domains of gene expression. Concomitantly, the early brain also begins to develop its complex morphological architecture. Once the final architecture is roughly in place, specific neurons then mature in their respective regions. The process is highly dynamic – gene expression and tissue architecture are constantly changing the environment of a cell, with each unique environment resulting in unique cell types.

In particular, the midbrain and hindbrain of vertebrates are patterned by a conserved organizing center called the midbrain-hindbrain boundary (MHB), or isthmic organizer, and these tissues collectively are known as the midbrain-hindbrain domain (MHD) or mes/r1 (175). In zebrafish, within mes/r1, the midbrain and the anterior hindbrain give rise to the optic tectum and the cerebellum, respectively, each developing on either side of a constricted ring of cells. While the identity of the genes important for the

formation of this organizer and subsequent tissue specification has been elucidated with gain and loss of function experiments *in vivo*, the precise roles and relationships of these genes have not yet been uncovered. Dynamic characterization of changes in gene expression in 3-D correlated with morphogenesis, however, could reveal important relationships between these regulatory networks and MHD development.

The MHB is positioned by overlapping expression of the homeobox genes *otx2*, expressed in the anterior neural plate, and *gbx1* in the posterior neural plate. *wnt1* is first expressed in zebrafish during gastrulation in the presumptive midbrain of the neural plate epithelium, and like *otx2*, also initially overlaps the presumptive anterior hindbrain. During neurulation, convergence/extension movements cause the neural plate to lengthen and thicken into the neural keel and the *otx2* and *gbx1/2* domains become exclusive by an unknown mechanism. By the end of segmentation, within mes/r1, *wnt1* expression also recedes anteriorly to the MHB, becoming confined to a small ring of cells around the neural tube at the posterior limit of the midbrain and a group of cells positioned along the dorsal midbrain. Here we used a fluorescent protein reporter for *wnt1* as a method to track lineages across the MHB and compared this to gene expression data for insight into how the boundary is sharpened.

4.2 Materials and methods

4.2.1 Generation and maintenance of transgenic zebrafish lines, in situ hybridization, mock in situ hybridization, and immunohistochemistry

Fish care and maintenance were performed according to standard protocols (169). The stable transgenic line Tg(*wnt1*:eGFP) has been described elsewhere (170). Briefly, a transgene construct was generated with an upstream 110 bp, major evolutionarily conserved (214) *wnt1* enhancer region driving eGFP expression and injected into wild type embryos at the 1-cell stage. Parent lines were crossed and the expression patterns of identified founders were compared to endogenous *wnt1* expression at bud stage, mid-somitogenesis, and 24 hours post fertilization (hpf). The reporter construct recapitulates the spatiotemporal

expression of *wnt1* within the MHD. ISH was performed as previously described (21) using NBT/BCIP (Roche, Indianapolis, IN). To minimize morphological distortions, embryos were never dehydrated in MeOH for storage.

To compare GFP protein distribution before and after fixation and ISH, embryos were imaged live with our UPM system at 24 hpf and immediately placed in 4% paraformaldehyde at 4°C and left overnight. Embryos were washed in PTW 3X for 5 minutes and, to protect the antigenicity of the GFP protein against heat denaturation (215), incubated in 150mM Tris-HCl at pH 9.0 for 5 minutes and heated to 70°C for 15 minutes. Embryos were washed again in PTW 3X for 5 minutes and mock ISH was performed exactly as a standard in situ hybridization, but no probe was used. For subsequent immunodetection of GFP, embryos were blocked in 1% BSA in PTW for 1 hour at room temperature and incubated with 1:100 Rabbit anti-GFP primary antibody (A-11122, Invitrogen, Life Technologies Corporation, Grand Island, NY) overnight at 4°C. Embryos were then washed in PTW 6X for 20 min and blocked again in 1% BS in PTW for 1 hour at room temperature and incubated with 1:50 Alexa Fluor 488 goat anti-rabbit secondary antibody (A-11008, Invitrogen) overnight at 4°C. After washing again 6X for 20 min in PTW, embryos were washed 3X for 5 min in PBS and re-imaged with our UPM system.

4.2.2 Time-lapse 2PF imaging

For time-lapse imaging, Tg(*wnt1*:eGFP) embryos were intercrossed and maintained at 25°C with 0.003% (w/v) phenylthiourea to prevent melanization until the 10 somite stage, when they were dechorionated and mounted in a dorsal orientation in 1.2% low melt agarose in a 2-3 mm deep well constructed from 1.2% standard agarose using a p200 tip (to allow room for tail growth). During imaging, embryos were maintained at 27°C using a temperature controller (Cole Parmer, Vernon Hills, IL) in a feedback loop with a heating pad placed underneath the embryo (Omega, Stamford, CT) and thermocouple (Omega) placed in the embryo medium which contained 200 mg/L tricaine. Z-stacks were acquired every 30 minutes at a step size of 3 μm with a pixel dwell time of 488 μs using a 20X objective with 1.0 NA (Carl Zeiss, Thornwood, NY) and 40 mW of power.

The UPM system has been described in previous sections. Briefly, sub-10-fs pulses from a passively mode-locked Ti:Sapphire oscillator (800 nm center wavelength, 133 nm full-width half maximum) were pre-compensated with dispersion compensating mirrors (GSM 270, Femtolasers) and coupled by a galvanometer driven x-y scanner (Cambridge Technology, Cambridge MA) into an upright microscope (Axioskop2 MAT, Carl Ziess). The beam was directed by a 635 nm short pass dichroic mirror (Chroma, Bellows Falls, VT) through the imaging objective to the sample. Autofluorescence and eGFP signals were collected through the imaging objective and separated using a 490 nm long-pass dichroic mirror, further discriminated with bandpass filters (450/60 nm for autofluorescence and 525/50 nm for eGFP) (Chroma), and detected with PMTs (Hammamatsu. Bridgewater, NJ). Data acquisition was controlled with custom LabVIEW software (National Instruments, Austin, TX).

4.2.3 2PF-OCM imaging

For 2PF-OCM imaging after ISH, embryos were mounted in agarose the same as for time-lapse imaging except for samples cleared with glycerol, for which a coverslip was placed over the well containing the embryo and coupled to the water immersion objective with PBS. In the 2PF-OCM setup, a 5% beamsplitter introduced in the path of the beam of the UPM system described above created a Michelson interferometer in which the sample and reference beams were recombined, coupled into a single mode fiber and sent to a home-built spectrometer that has been described in previous sections for Fourier domain detection. Z-stacks were acquired with a step size of 3 μm using a 40X, 0.8 NA objective (Carl Zeiss), and OCM images generated by integrating the FFT of the spectral interferogram acquired for each pixel as images were rendered *en face* simultaneously with 2PF collection. Pre-compensation of the sub-10-fs pulses was adjusted to account for the beam splitter and 40X objective.

4.2.4 Image processing and registration

Image stacks (256 x 256 x 60 voxels) were scaled in FIJI to account for different sampling along the in-plane dimensions versus the axial dimension, so that each voxel was equivalent to 1.6 x 1.6 x 1.6 μm^3.

Stacks obtained of the MHD region of developing embryos were rotated in FIJI to an optimal orientation in which the entire dorsoventral axis of the MHB constriction was aligned parallel to the z-axis. This standard orientation ensured that measurements taken from the same embryo over time, or from the same embryo imaged under different conditions, were repeatable. Multi-channel and multi-modal 3-D renderings were created in V3D, known now as Vaa3D (172, 216).

OCM images contained contrast from both the embryonic tissue and from the NBT/BCIP stain. To produce images exclusively of gene expression domains marked by the deposition of NBT/BCIP stain from combined 2PF-OCM, we took advantage of quenching of embryonic tissue autofluorescence by the NBT/BCIP precipitate. First, we measured the average value of the signal from the tissue in regions where no NBT/BCIP was expected in both the 2PF and OCM images. We normalized the intensity of tissue in the 2PF image to the intensity of the tissue in the OCM image and subtracted it from the OCM image in order to subtract the contribution from the embryonic tissue and isolate the NBT/BCIP signal. Since the autofluorescence was quenched in regions where NBT/BCIP was deposited, values subtracted from the OCM image were much lower in these regions, additionally enhancing the contrast.

Processed post ISH image stacks of NBT/BCIP marked gene expression were registered to image stacks of GFP marked lineage using the mutual morphological information in each stack from tissue autofluorescence with the "Name and Register Landmarks" plugin in FIJI. Global accuracy of registration was evaluated by manually segmenting the neuroepithelium in each transverse section of the 3-D data along the anteroposterior axis, converting these to a black and white image, and calculating an overlap coefficient defined as the ratio of the sum of the intersection of the transformed image and the live template image divided by twice the sum of the live template image. Local accuracy was determined by comparing the alignment of the peaks of GFP from anti-GFP immunostained embryos post mock ISH registered to live Tg(*wnt1*:eGFP) embryos along the dorsoventral axis.

4.3 Results and discussion

We combined lineage mapping and gene expression profiling using 2PF-OCM and image registration to study the formation of the MHB constriction with the approach shown in Fig 4.1. We hypothesized that distinct midbrain and hindbrain compartments are created by changes in gene expression within lineages at the MHB. To test this hypothesis, we quantified the dynamics of *wnt1* enhancer driven GFP signal in mes/r1 during the segmentation period and registered the end point with a subsequent ISH for *wnt1* mRNA. We also used 2PF to quantify the effects of fixation and ISH on mes/r1 morphology and the accuracy of registration. We found this approach provided a good approximation of the 3-D distribution of a particular genetic lineage compared to the subset of the lineage still actively expressing the gene of interest, within the context of live brain morphology, and that the subset of the *wnt1* lineage found initially in the hindbrain behaved differently depending on its dorsoventral position in the neural tube to sharpen the MHB.

4.3.1 MHD morphogenesis and mapping the wnt1 lineage with time-lapse 2PF

We utilized the broad power spectra of 10 fs pulses, compared to those used in conventional 2PF (129), to image the MHD of embryos from mid-somitogenesis to early pharyngula stages in order to capture the dynamics of neuroepithelium morphogenesis and the *wnt1* lineage. As a control to measure whether this imaging regimen affected normal development, transgenic and wild type embryos were imaged under the same conditions and allowed to develop until the swim bladder had inflated at 5 days post fertilization (n=3/3). No apparent damage was observed, apart from mild edema from extended exposure to tricaine and restricted growth of the tail from embedding in agarose similar to what has been previously reported (184). For combined 2PF-OCM, embryos were immediately fixed after time-lapse imaging.

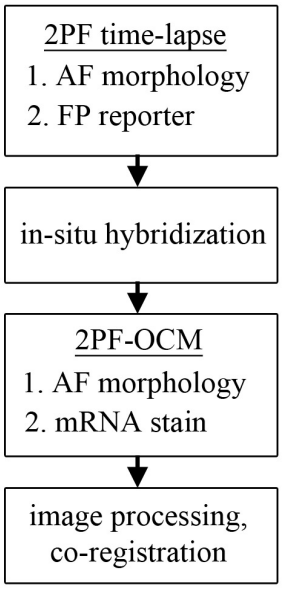

Fig 4.1 Combined lineage mapping and expression profiling. Using a combined 2PF-OCM system utilizing ultrashort pulses, complementary data sets of the spatial distribution of a genetic fluorescent protein (FP) reporter used as a lineage tracer and regions of active gene expression (mRNA stain) are collected from the same embryo live and post-fixation, respectively. Subsequent co-registration of the data using morphological landmarks from the neuroepithelium autofluorescence (AF) enables direct comparison of the active and historical gene expression profiles of a particular cell lineage in a live morphological context.

We set the initial time point, t=0:00 at the 12 somite stage (ss), when the MHB is morphologically visible, but the neural keel is closed along the anterior-posterior axis (Fig 4.2A, t=0:00), and acquired 180 μm z-stacks with a step size of 3 μm approximately every half hour. Fig 4.2A shows three views of this progression, a dorsal section (D) through the center of the neural keel at the MHB, a transverse section at the MHB constriction (T), and a lateral section lateral to the midline (L). The hindbrain ventricle opens first, initiating at the roof plate and extending ventrally while the neural keel of the midbrain and MHB remains closed (Fig 4.2A, t=1:22). Subsequently, the midbrain vesicle opens while the neural keel/tube remains shut at the MHB constriction (Fig 2A, t=2:02) until it opens at t=3:13, and the constriction becomes more pronounced, giving rise to the primordia of the tectum and cerebellum in the midbrain and hindbrain respectively (Fig 4.2A, t=7:34). This sequence of events is in correspondence with what has been previously reported (217) and further demonstrates the viability of embryos imaged with

2PF using sub-10-fs pulses over long periods of time. We also observed the retraction of fine cellular processes during ventricle formation, marked by an arrow in Fig 4.2A (t=3:13) in both midbrain and hindbrain formation, as has been previously shown (217).

Within this evolving architecture of the embryonic brain, the *wnt1* lineage is marked by the expression of a reporter GFP molecule under the control of a *wnt1* enhancer such that once the *wnt1* gene is activated in a cell, that cell and its progeny will remain fluorescent for the lifetime of the GFP proteins that were generated, even if *wnt1* expression ceases. Thus, all cells in the embryo that have expressed *wnt1* under the control of this enhancer are marked by GFP for >24 hours (218) and we simultaneously followed this lineage throughout somitogenesis.

We quantified fluorescence intensity profiles of the *wnt1* lineage from the neuroepithelial tissue in dorsal and ventral regions of the embryo using the freehand line tool, allowing us to profile the same tissue over time despite dramatically changing morphology. At t=0:00, the *wnt1* lineage extends into the anterior hindbrain as shown by the position of the bars in Fig 4.2A and quantitatively in Fig 4.2B,C. As development progresses, cells in the midbrain just anterior to the sharpening physical constriction build up increasing amounts of GFP protein regardless of dorsoventral position in the neural tube (-50 to 0 μm, Fig 4.2B,C). In the dorsal midbrain neuroepithelium, the lineage proliferates at a higher rate than in nearby tissues (217), possibly contributing the bowing of the developing tectal lobes, as the overall length of this domain increases (Fig 4.2B) despite its confinement to the same space along the anterior-posterior axis (bars, Fig 4.2A). In the anterior of the dorsal midbrain neuroepithelium, reporter intensity increases at the presumptive epiphysis, (-250 to -300 μm, Fig 4.2B) a sensory region involved in circadian rhythms.

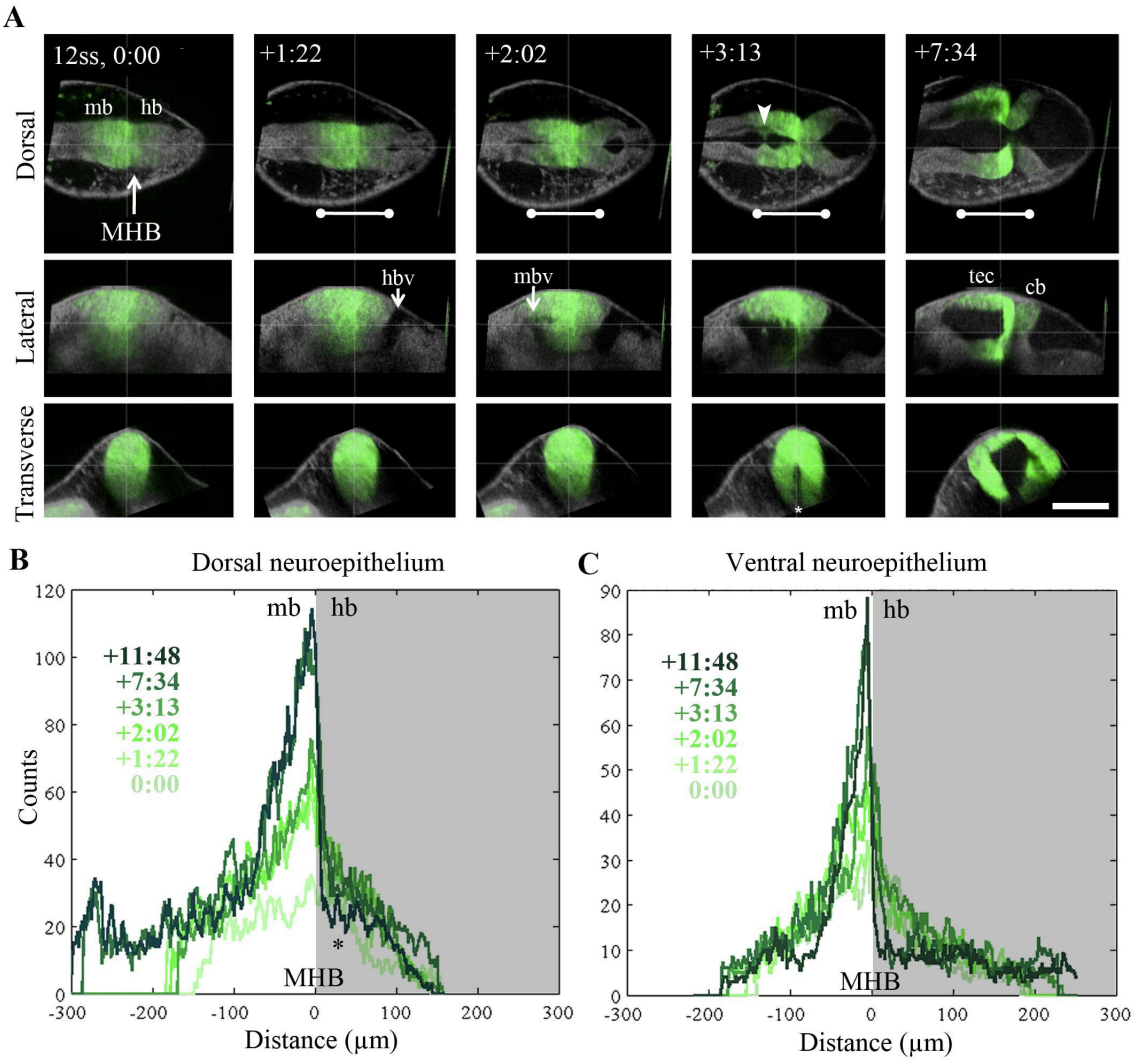

Fig 4.2 *wnt1* lineage mapping during morphogenesis using time-lapse 2PF indicates different mechanisms for boundary refinement depending on dorso-ventral position in the neuroepithelium. (A) Dorsal, lateral, and transverse sections of the *wnt1* lineage in the developing midbrain-hindbrain domain (MHD) over time. As the midbrain-hindbrain boundary (MHB) forms dividing the midbrain (mb) and hindbrain (hb) primordia, the hindbrain ventricle (hbv) opens first, followed by the midbrain ventricle (mbv) that are subsequently connected by the opening of the isthmus region (asterisk). Cellular processes retract during ventricle formation (arrowhead). By +7:34, regions that will develop into the optic tectum and cerebellum are clearly morphologically distinct. Bars indicate the *wnt1* lineage within the neuroepithelium is stationary in the A/P direction. A portion of the *wnt1* lineage in the midbrain undergoes epithelial-to-mesenchyme transition at +7:45 (not shown). Scale bar = 100 μm. (B) Quantification of reporter fluorescence intensity changes from dorsal and ventral regions of the MHD over time shows steady increase of reporter intensity just anterior to the MHB (0 to -30 μm) within the midbrain as well as more anteriorly near the epiphysis (dorsal plot, -200 to -300 μm). Intensity within the midbrain and hindbrain are slowly (dorsal, asterisk) or sharply (ventral) decreasing.

In the dorsal hindbrain neuroepithelium, reporter intensity fluctuates and appears to decrease slightly by 24 hpf (asterisk, 0 to 100 μm, Fig 4.2B). We measured similar dynamics in the ventral midbrain neuroepithelium, however, in the ventral hindbrain neuroepithelium, the reporter fluorescence drops sharply over time (0 to 100 μm, Fig 4.2C).

Measurable changes in intensity of reporter fluorescence can be due to the combination of several independent factors. Continuing transcription would contribute to an increase in fluorescence intensity, as can be seen in the *wnt1* lineage just anterior to the MHB and in the presumptive epiphysis. In these tissues, we can conclude that *wnt1* remains actively expressed if the activity of the native and reporter mRNA transcripts are similar. Unchanging or decreasing reporter intensity is more difficult to interpret. GFP degradation, photobleaching, or redistribution during cell proliferation all would cause a decrease in intensity. Since the rates of these different options are difficult to measure independently, we cannot make definitive conclusions about which cells in the lineage are still actively expressing the gene of interest if the intensity is unchanging or decreasing. With respect to MHB refinement, our results suggest that in the dorsal neuroepithelium, the MHB is refined as a small group of cells continue or increase their rate of *wnt1* transcription while cells away from the boundary reach a steady-state or stop transcription by the end of somitogenesis. In the ventral neuroepithelium, the sharp decline of GFP signal could indicate cells sorting to sharpen the boundary, as the *wnt1* lineage is no longer physically present in the anterior hindbrain to generate GFP signal. The ability to see the regions where *wnt1* remains actively expressed by imaging *wnt1* mRNA distribution would help to distinguish between these possibilities.

4.3.2 Quantification of morphological distortion due to in situ hybridization

Although ISH is a common technique, there has been little work done to quantify how the protocol affects embryo morphology. Fixation is already known to shrink biological tissues (219-221), but how fixation and further processing with ISH may affect tissue morphology, specifically of the early embryonic brain, has not been examined.

To quantify the distortions we would need to correct in order to register mRNA transcript data acquired post ISH to fluorescent reporter protein data acquired from live embryos, we imaged five 24 hpf embryos with 2PF at different points in the processing. Autofluorescence from the neuroepithelium was collected 1) live, 2) post fixation, 3) after in situ hybridization, and 4) after optical clearing with glycerol. Qualitative analysis of the images, shown in Fig 4.3A, reveal a dramatic and additive change in brain morphology.

We selected four parameters to characterize brain morphology deformation within mes/r1. A/P distance is the distance from the widest point of the midbrain to the widest point of the hindbrain (Fig 4.3B) and provides a measure of changes in the anteroposterior aspect of the embryo, which we refer to as longitudinal changes. The MHB angle characterizes changes in the structure of the constriction and as this value changes with depth, is measured always in the dorsal plane of the sulcus limitans, identified in the transverse section where the midbrain is widest. The midbrain tissue parameter is the cross sectional area of the tissue in a transverse section at the widest point of the midbrain, and is a measure of distortions of the neural tube radially. Finally, the midbrain ventricle parameter is the cross sectional area of the ventricle in the same transverse section, and provides a measure of ventricle collapse. How these parameters change would then inform potential registration strategies.

We found that for each of these four parameters, measured using FIJI, each step in the processing produced a significant change, with effects cumulating in 31% average longitudinal shrinkage, 77% increase in the MHB angle, 53% shrinkage in the radial direction and 79% ventricle collapse. Notable is the significant increase in MHB angle, altering the conformation of the morphologically complex constriction after ISH when compared to live embryos. With this information, we decided to concentrate more registration landmarks near the MHB to compensate for these drastic distortions. We also noted that even though the MHB angle increased, which possibly has the effect of increasing A/P distance, the overall distance we measured decreased. We considered this might lead us to underestimate the shrinkage in the A/P direction, making it difficult to assess if the embryo shrinks uniformly. For this reason, we did not attempt to scale embryos prior to image registration. In the future, it may be useful to use fiduciary

markers, such as GFP-H2B and/or DAPI stained nuclei, to characterize strain fields within the tissue, as has been done in human brains (222) and avian embryos (223), to quantify local tissue-dependent differences in the deformations induced by ISH.

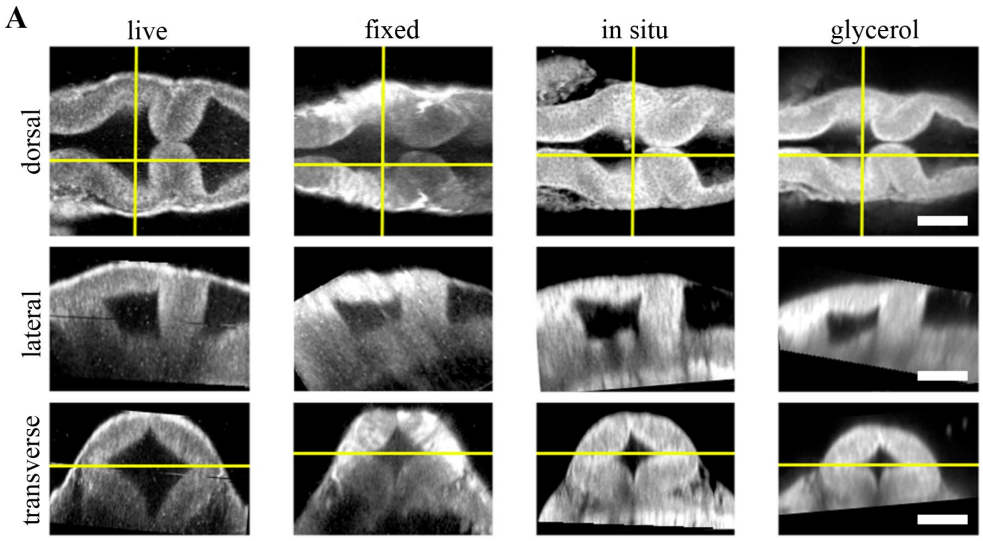

Fig 4.3 Processing for in situ hybridization introduces significant morphometric distortions, including longitudinal and radial shrinkage of the tubular neuroepithelium, diminishing constriction angle and ventricle collapse. (A) Dorsal, lateral, and transverse sections of autofluorescence signal from the same embryo imaged with 2PM live, after fixation in 4% paraformaldehyde, after performing mock in situ hybridization, and after equilibration in 100% glycerol shows striking distortion of early brain morphology at 24 hpf. Scale bar = 100 μm. (B) Four morphometric parameters were measured from the same individual embryo to quantify significant ($p>0.95$) contributions of each processing step toward longitudinal and radial tissue shrinkage (A/P distance and Midbrain tissue area), disruption of the constriction (MHB angle), and ventricle collapse (Midbrain ventricle area). These distortions will need to be corrected to combine the spatial distributions of the live reporter and mRNA for direct comparison.

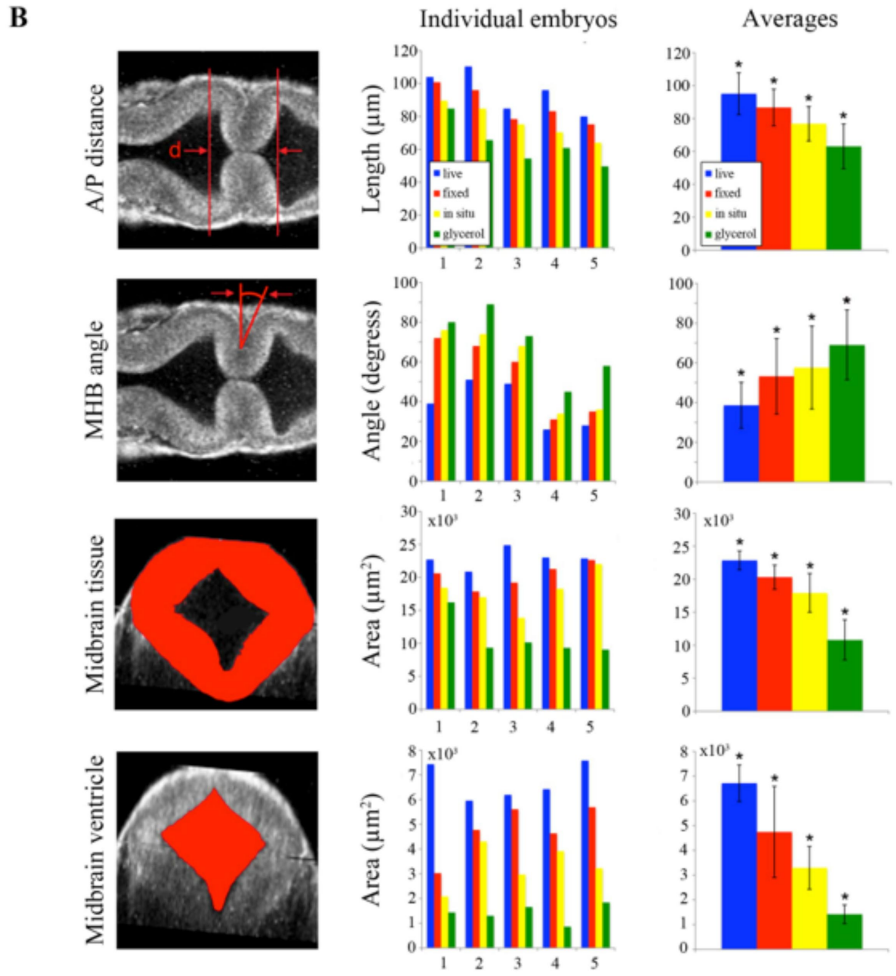

Fig 4.3 Continued.

4.3.3 Imaging domains of gene expression with 2PF-OCM

To utilize the robustness of NBT/BCIP staining for analyzing gene expression domains in 3-D, we imaged embryos after performing ISH to detect *wnt1* mRNA using combined 2PF-OCM. Using both modalities provides the advantage of simultaneously imaging tissue morphology with gene expression domains. Subsequent image registration may also be simpler with both data sets acquired on the same UPM platform.

Fig 4.4A shows the results of imaging *wnt1* gene expression domains in zebrafish embryos fixed at 24 hpf that were not optically cleared after ISH. Two-photon excited autofluorescence (AF) signal is quenched in regions of the embryo, outlined in yellow, where a strong contrast in the OCM image shows the presence of NBT/BCIP compared to areas where *wnt1* is not expected to be expressed, unstained tissue outlined in blue. The neuroepithelium, which in the zebrafish embryo at this stage of development is quite transparent, is also visible with OCM. In the resulting overlay, red to yellow indicates the tissue unstained and unquenched by NBT/BCIP, while green regions are where NBT/BCIP is present.

OCM has been used to image retinal regeneration in adult zebrafish (224) and to evaluate the effects of ethanol on embryonic brain development in larval zebrafish (225, 226). These tissues are turbid compared to the 24 hpf embryo, and we could only find one report of OCM imaging on 24 hpf zebrafish (227) in which the signal seemed comparable to our data, relatively weak, presumably due to the transparency of the embryo. In these cases, OCM provides only structural information about tissue morphology. There have been efforts to use OCM for imaging with molecular contrast such as detecting backscattered light from gold nanoparticles conjugate to antibodies for immunodetection (228) and using spectral domain detection to look for absorption signatures of specific molecules such as hemoglobin (229), but to our knowledge, this is the first report of the application of OCM to image molecular contrast using NBT/BCIP.

By omitting the clearing step that requires equilibration in glycerol, morphological distortions of the early brain from ISH processing could be drastically reduced. A/P shrinkage, MHB angle relaxation, radial shrinkage, and ventricle collapse could be reduced 14%, 30%, 38%, and 29% respectively, reducing demands on image registration significantly. Yet optical clearing agents such as glycerol are known to reduce tissue attenuation and improve contrast in OCM on a variety of biological specimens (230, 231), and we considered whether clearing could preferentially improve the OCM signal from the NBT/BCIP precipitate over the neuroepithelium tissue. To determine if there was indeed any benefit to clearing the tissue toward enhancing the NBT/BCIP contrast and decide if that benefit was worth correcting for the

additional distortions to the embryo, we performed ISH for *wnt1* on embryos and compared the signals from ones that were subsequently cleared to those that were not (n=10).

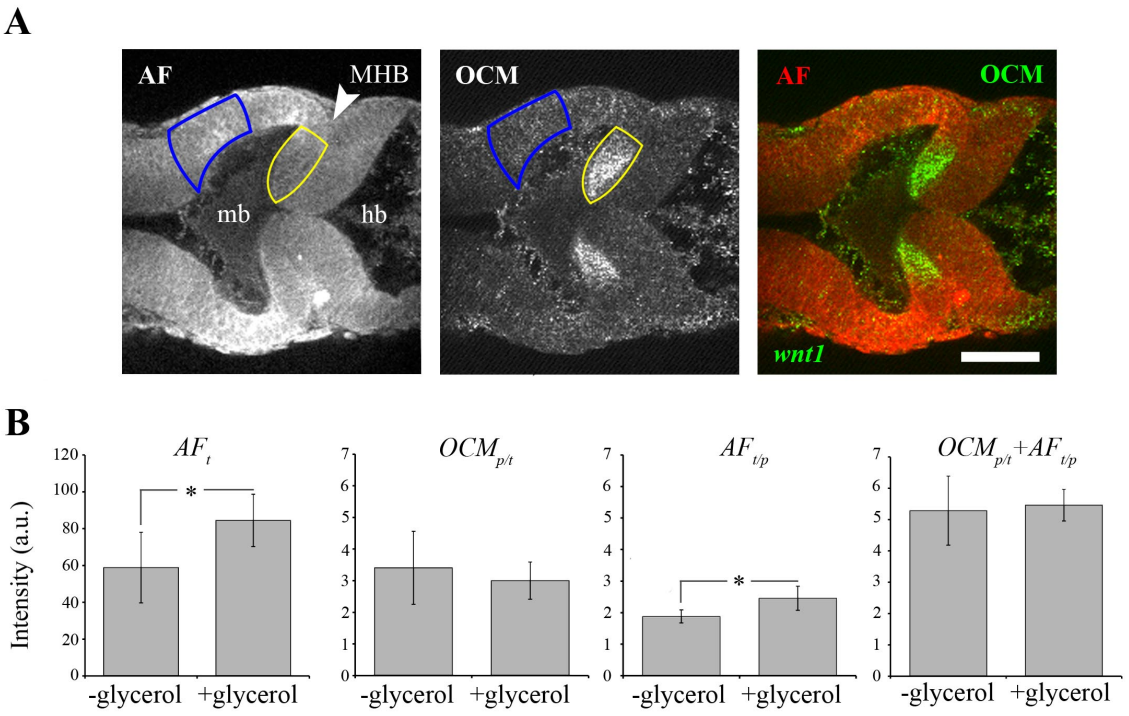

Fig 4.4 Imaging gene expression in the midbrain-hindbrain domain with 2PF-OCM using ultrashort pulses is not enhanced with glycerol optical clearing treatment. (A) Dorsal section from a 24 hpf embryonic brain after in situ hybridization to detect *wnt1* shows quenched autofluorescence (AF) and increased backscattering detected by OCM in regions where the NBT-BCIP precipitate is deposited (yellow outlined region). Unstained neuroepithelial tissue generates positive AF and OCM signals (blue outlined region). Combining these images results in brain tissue appearing red to yellow and the precipitate marking regions actively expressing *wnt1* in green in the midbrain anterior to the MHB constriction. Scale bar = 100 μm. (B) Signals from embryos treated with or without glycerol after in situ hybridization were quantitatively compared. Tissue autofluorescence, AF_t, is significantly increased with glycerol treatment, and to a lesser extent, the intensity ratio from unstained tissue relative to areas of quenching from the precipitate, $AF_{t/p}$ (p>0.95). Glycerol treatment increased OCM signal from unstained tissue and areas where the precipitate were deposited similarly, resulting in no significant difference in the intensity ratio $OCM_{p/t}$. When both quenched 2PF and positive OCM signals are combined, $OCM_{p/t} + AF_{t/p}$, NBT/BCIP can be detected from embryos not treated with glycerol just as well as those that have been cleared, so that morphological distortions can be minimized.

Fig 4.4B shows a comparison of relative potential for NBT/BCIP specific contrast based on the use of positive OCM signal from and quenching of autofluorescence signal by NBT/BCIP in embryos that were equilibrated in 100% glycerol after ISH and those that were stored in PBS. In agreement with previous reports, tissue autofluorescence measured from unstained neuroepithelial tissue in the region outlined in blue, AF_t, increased significantly with glycerol treatment (232). OCM signal in stained and unstained regions of the embryo both increased significantly (not shown), but not preferentially, for unstained tissue as the ratio of the signal from stained versus unstained tissue, $OCM_{p/t}$, did not change significantly. Clearing did cause a small but significant increase in quenching of autofluorescence signal in stained areas of the embryo, $AF_{t/p}$, but when the two modes of contrast were combined, there was no significant improvement in NBT/BCIP detection in cleared embryos.

4.3.4 Landmark co-registration of different data sets from the same embryo

After quantifying the effects of ISH on tissue morphogenesis and determining that there was no benefit to optically clearing the embryos, we defined landmarks in the late somitogenesis zebrafish MHD for 3-D image registration. Constantly changing morphology made selection of reliable landmarks non-trivial, and since thin-plate spline registration can be computationally costly, it was desirable to minimize the number of landmarks. In studies on the rhesus hippocampus, 10 landmarks was a sufficient number for accurate registration (233) while in prostate samples, 22 landmarks provided sufficient accuracy (234). In Fig 4.5, we present a set of 24 landmarks for registration of the zebrafish mes/r1.

Fig 4.5A shows an X-slice rendering of the 24 hpf MHD imaged live with 2PF. Three transverse planes were readily identifiable during the morphogenesis of the MHD from mid to late somitogenesis within the same embryo imaged over time and from the same embryo imaged under different conditions, *ta*, for transverse anterior, *tm*, for transverse middle, and *tp*, for transverse posterior. *ta* was the same plane used for quantifying embryo distortions due to ISH, the transverse plane in the midbrain where the neural tube is widest. *tm* is the narrowest point of the constriction, and *tp* was the transverse plane in the hindbrain where the neural tube is widest. These transverse sections, shown in Fig 4.5B, provided several

obvious choices of morphological landmarks, which we chose to concentrate close to the boundary where deformations between data sets to be registered were predicted to be greatest. We applied thin-plate spline registration in FIJI to register the neuroepithelium of embryos imaged post ISH to those imaged live, using the autofluorescence signal to obtain this mutual information. Fig 4.5C shows an overlay of the live (magenta) and registered post ISH (green) morphology and suggests qualitatively that the registration is reasonably accurate. We then sought to quantitatively determine registration accuracy at different scales relevant to the goals of our registration.

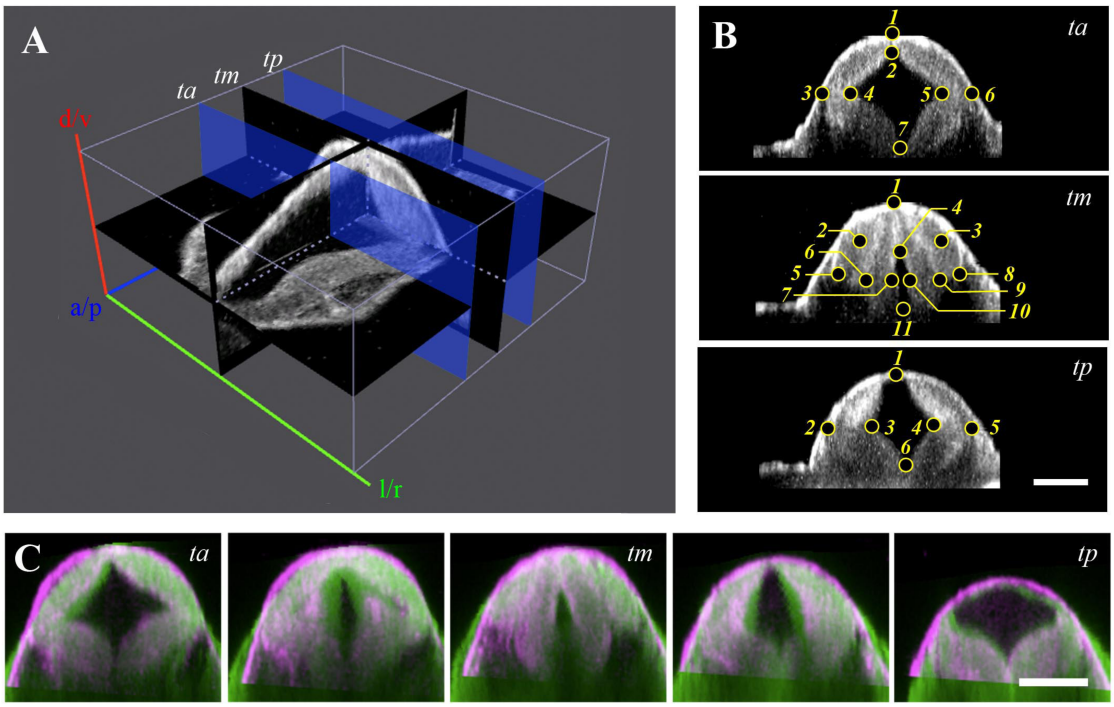

Fig 4.5 Qualitative performance of morphological landmark registration of different data sets from the embryonic zebrafish brain at 24-28 hpf. (A) To find the same landmarks in different data sets, point were selected from autofluorescence data in the anterior region of the MHD from the widest transverse section of the midbrain, t_a, from the narrowest section of the constriction, t_m, and posteriorly from the widest section of the hindbrain, t_p. (B) From each section, 6-11 landmarks can be identified from the distinct morphology introduced by the ventricles and the dorsolateral hinge points of the neural tube and the lobes of the expanding tectum. (C) Overlay of co-registered transverse sections of live (magenta) and post in situ hybridization (green) data sets, where the distorted morphology is restored onto the live morphology. Scale bar = 100 μm.

Analysis of registration accuracy depends highly on the application (235). We first evaluated the accuracy of registration of the data at the scale of the tissue, to characterize the global accuracy. Fig 4.6A shows the effect of registration on the parameters previously used to characterize deformations in the MHD due to ISH. In all cases, parameter values matching those for live embryos were recovered with registration. Target registration error (236) is a common method to quantify registration accuracy, but it is not suitable for this thin-plate spline implementation since it constrained our landmarks of interest to correspond exactly which would result in zero error unless alternative targets were measured. As we already implemented our most reliably identifiable landmarks (targets) for registration, it seemed more appropriate to use an overlap coefficient, *o.c.*, based on the Dice Similarity Index (237) that quantifies overlap between objects. Our results, ranging between 0.77 and 0.99 with an average of 0.89, fell within what is clinically considered useful for medical image registration (238).

To address registration accuracy at the level of the gene expression domain, we imaged Tg(*wnt1*:eGFP) embryos live with 2PF at 24 hpf, subsequently processed them with a mock ISH protocol, immunostained for GFP, and then re-imaged and registered the data sets. Immunostaining for GFP using FITC for secondary detection was necessary since the hybridization step in ISH required heating to 76°C which denatured the GFP protein. With these data, shown in Fig 4.7, we compared the lineage boundary of highest GFP expression at the MHB in the template and registered images. Using the same plotting tool we implemented to trace the dynamics of the GFP marked *wnt1* lineage, we plotted the live GFP distribution and post-ISH α-GFP distribution from different dorsal planes along the dorsoventral axis. The boundaries coincided within 3.2-8 μm, equivalent to 1-5 pixels, with best performance near the sulcus limitans that corresponds with many of our landmarks. These results suggested we can register the MHB in 3-D with an accuracy within 1-3 cells, given the density and orientation of the cells within the neuroepithelium at this stage of development.

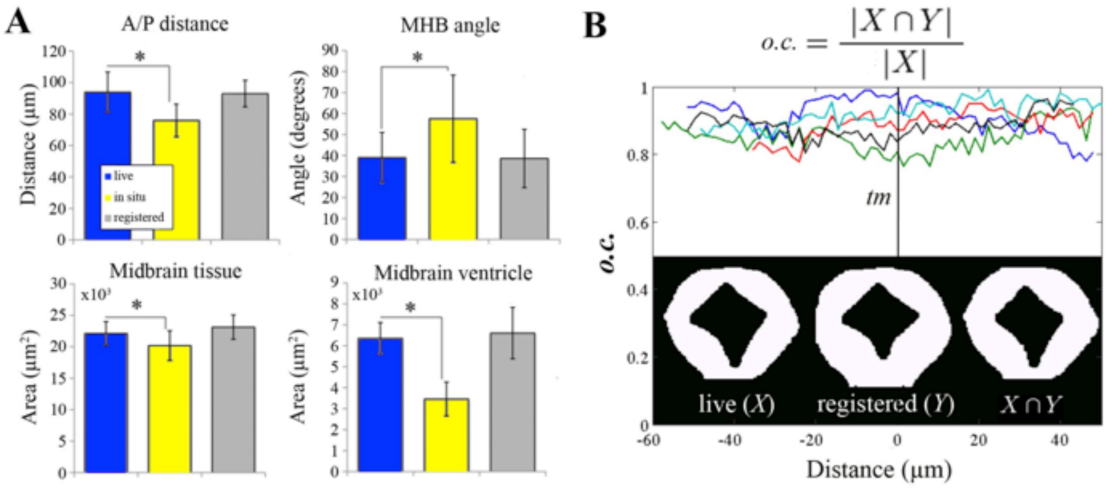

Fig 4.6 Quantitative analysis of the global accuracy of morphological landmark registration. (A) The significant tissue shrinkage and morphological distortions (p>0.5) to brain morphology measured from autofluorescence and introduced by in situ hybridization can be restored to values matching live morphology using landmark registration. (B) The overlap coefficient, *o.c.*, of binary transverse sections of manually segmented coregistered data sets was calculated to quantify the accuracy of the registration algorithm at the global or tissue level. Accuracy is comparable in both the constraining planes where the landmarks are selected and planes in between.

While our first application of thin-plate spline registration was reasonably accurate, improvements and further quantification of registration accuracy should be considered. If it can be determined that ISH caused the MHD tissue to shrink uniformly, scaling the embryos prior to registration could potentially improve accuracy. Also, an affine registration could be implemented prior to non-rigid registration to potentially increase performance and landmark selection could be automated to remove user error. Optimization of the registration approach should account for accuracy at the cellular scale. For example, morphological landmarks could be used for registration and individual cell positions, marked by mosaic expression of H2B-GFP for example, used to calculate target registration error.

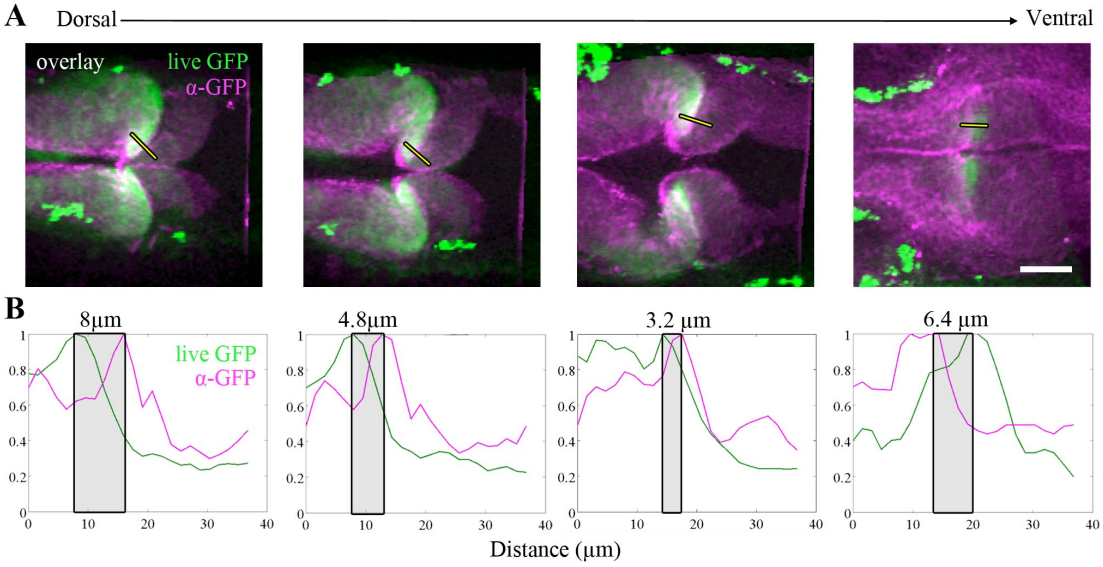

Fig 4.7 Qualitative and quantitative analysis of the local accuracy of morphological landmark registration. (A) Dorsal sections at varying depths from coregistered overlay of live GFP reporter distribution (green) and α-GFP immunostaining post mock in situ hybridization (pink). Outlined yellow lines correspond to normalized intensity plots depicted in (B) which show the MHB boundary, marked by peak GFP intensity, can be accurately aligned within one to two cell diameters. Scale bar = 50 *µ*m.

4.3.5 Registration of the wnt1 lineage and the sub-population of the wnt1 lineage still actively expressing wnt1 in a live morphological context

Having shown that the our registration approach using morphological landmarks from 2PF autofluorescence will allow us to compare the distribution of the GFP marked *wnt1* lineage in Tg(*wnt1*:eGFP) embryos to the distribution of *egfp* mRNA, we sought to determine which cells within mes/r1 were still actively expressing *wnt1* in order to shed light on how the MHB is sharpened. Fig 4.8A shows the results of registration of these data. Optical sections in the dorsal neuroepithelium of autofluorescence, GFP, and NBT-BCIP show the morphology, *wnt1 lineage*, and *wnt1* expressing cells, respectively. Maximum intensity projection of the data registered in 3-D show GFP lineage tracer perdurance away from the boundary (green) while NBT/BCIP is exclusive to a group of boundary cells anterior to the constriction within the *wnt1* lineage (yellow). Punctate NBT/BCIP signal in the dorsal

hindbrain may correspond to a small number of cells known to express *wnt1* as part of the initiation of a program of migration and differentiation to tegmental nuclei (34).

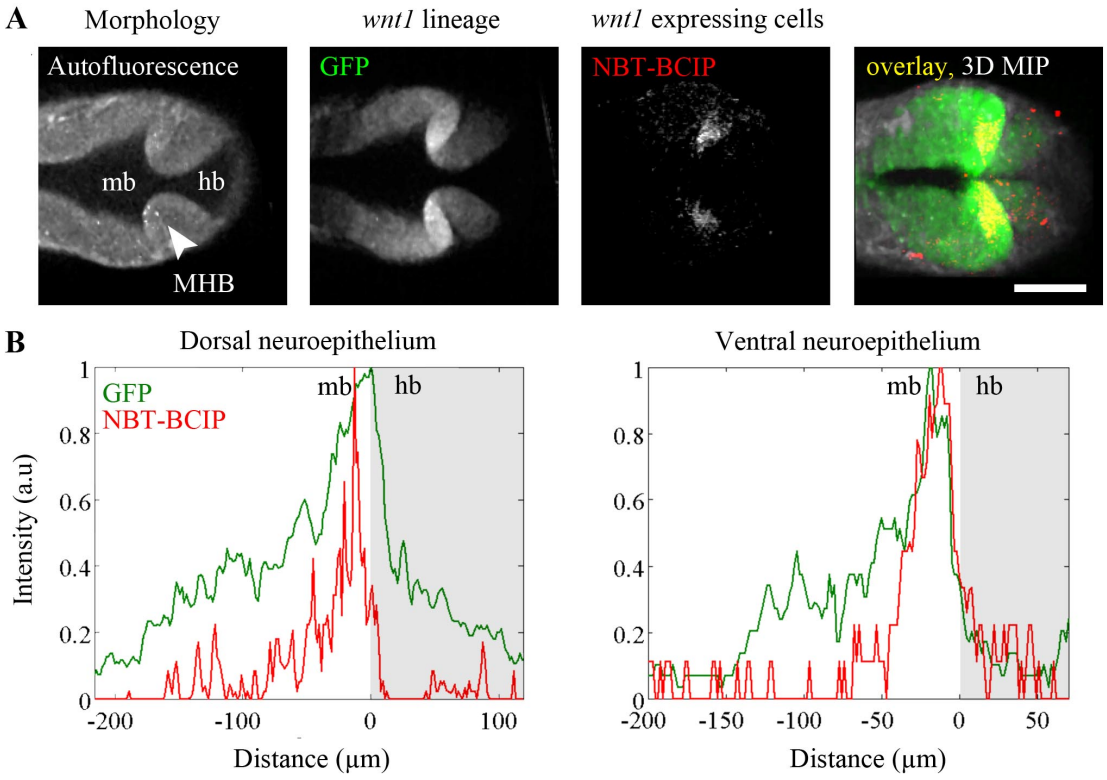

Fig 4.8 Visualization and quantification of the subset of the *wnt1* lineage actively transcribing *wnt1* mRNA in a live morphological context. (A) Dorsal sections of the autofluorescence, live GFP reporter, and coregistered NBT/BCIP signal from combined 2PM-OCM showing the live morphology, *wnt1* lineage, and actively *wnt1* expressing cells respectively in the MHD region at 24 hpf. A maximum-intensity projection of the 3-D pseudo-colored overlay shows that active gene expression is restricted to a subpopulation of the initially specified *wnt1* lineage in the posterior midbrain, just anterior to the MHB constriction, and isolated cells in the anterior hindbrain. Scale bar = 100 *µ*m. (B) Intensity profiles of the live reporter fluorescence and NBT-BCIP signal from dorsal sections in the neuroepithelium show that dorsally there is still a significant presence of *wnt1* lineage that has stopped expressing *wnt1* as evidenced by the GFP signal in the absence of NBT/BCIP. Ventrally, the anterior hindbrain does not have significant GFP or NBT/BCIP signal, indicating the *wnt1* lineage previously present has moved physically from the location, perhaps migrating into the midbrain or sorting to the dorsal region of the anterior hindbrain.

Similarly to previous dynamic lineage tracing, we quantified the distribution of GFP and NBT/BCIP across the MHB in the dorsal and ventral regions of the neural tube, respectively, shown in Fig 4.8B. Now it is possible to ascertain whether or not the *wnt1* lineage in the dorsal hindbrain has stopped expressing *wnt1,* which it appears the majority of the cells in that lineage have done. These results show that while *wnt1* was initially expressed across the presumptive MHB, cells in that region received signals telling them to stay in place and turn *wnt1* off, resulting in a sharp boundary of gene expression at the dorsal MHB constriction. In contrast, in the ventral neuroepithelium, we know from dynamic lineage tracing that the *wnt1* lineage is initially present in the ventral hindbrain but by the end of segmentation, no perduring GFP is found there. The lack of GFP in this region once occupied by part of the *wnt1* lineage suggests that those cells have physically moved to a new location, potentially by sorting either anteriorly across the MHB into the midbrain, or also possibly dorsally into the dorsal hindbrain, leading to the refinement of the ventral MHB. As the dorsal and ventral environments of the neuroepithelium are known to differ in terms of gene expression and subsequent fates, it is not surprising that the mechanism for refining the MHB should differ along the dorsoventral axis. What is remarkable is that two different mechanisms may exist to segment the midbrain and hindbrain along the anteroposterior axis, highlighting the importance of this evolutionarily conserved boundary.

4.4 Conclusion

We have discussed the importance of two common techniques used to study embryonic development, lineage tracing and in situ hybridization, and the potential for uncovering mechanisms of neural patterning by combining these analyses. To date, ISH data are rarely linked to lineage mapping data, and when they are, the fluorescent protein reporter is detected with immunostaining after ISH (34). We now know that while this approach provides a good comparison of lineage distribution and gene expression, the morphological context in which it is evaluated is significantly different from that *in vivo*. We have also used our approach to characterize dorsoventral differences in the mechanism of MHB boundary sharpening.

Combined 2PF-OCM using UPM can be used to examine both genetic lineages and gene expression patterns in their morphological context when intravital imaging is followed by in situ hybridization and registration. Several important, unique aspects of our approach enabled such analysis. First, this analysis was enabled by the preservation of eGFP perdurance throughout 2PF time-lapse imaging. Lack of photobleaching was apparent by comparison of the broad distribution of eGFP fluorescence and contrastingly narrow distribution of *egfp* mRNA transcripts from co-registration of the last time-lapse frame, that accurately reflected the historical and the instantaneous expression of *wnt1,* respectively, within the MHD. We also demonstrated embryo viability under these imaging conditions, showing that development of the MHD region progresses as expected in embryos that further develop normally to larval stages. Finally, we showed that sub-10-fs pulses excite autofluorescence signal well enough to see clearly the morphology of embryonic tissues, providing important context for analysis of cell lineage and molecular fate. The autofluorescence signal was strong enough to even visualize individual cell nuclei (239), data that could potentially be used for tracking individual cell behaviors label-free. Of particular importance was its usefulness both *in vivo* and post ISH for visualizing morphological landmark correspondences.

Our approach will also be useful for evaluating aberrant neural patterning. For example, *fgf8a* is an important signaling molecule in the MHD program expressed in a narrow ring at the MHB in the anterior hindbrain, as a counterpoint to *wnt1*. The major feature of the *fgf8a* mutant phenotype, *acerebellar*, is lack of a cerebellum. In these mutants, several MHB genes including *wnt1, pax2a,* and *engr2* are activated properly, but their expression at the MHB is not maintained after mid-somitogenesis (240). The subsequent fate of these lineages has not been well characterized, but since expression is properly activated, the perdurance of a reporter gene could be used to track these populations and, combined with ISH, to reveal morphogenetic and molecular alterations of their developmental programs due to lack of *fgf8a* activity. In such cases, combined 2PF-OCM could provide important insights into the roles and regulatory relationships of MHB genes.

Multi-modal image registration also provides a way to integrate various morphometric and molecular data collected from different embryos and build up systematic models of developmental processes (241, 242). Atlas and virtual embryo generation in model organisms have been areas of interest especially with the dawning of systems biology and bioimage informatics. Atlases in mice (243), chick (244), fly (69), worm (245), ascidians (246), frog (247), zebrafish (248), and even humans (249) have been reported targeting different developmental stages and structures. Here we demonstrated the beginnings toward a dynamic zebrafish atlas of early brain patterning that incorporates both gene expression and lineage information. With the development of UPM to dynamically image several fluorescent protein reporters at once (250), our lineage mapping experiments have the potential, with the requisite multi-color transgenic lines, to monitor the spatiotemporal distribution of multiple lineages simultaneously and map the unique pathways of gene expression leading to specification of different cell types. Subsequent ISH and image registration would reveal unique gene expression signatures within those lineages that could simultaneously be correlated with morphogenesis within a complex 3-D brain architecture. We conclude this approach will be generally useful for integrating the analysis of neural patterning at the morphological, cellular, and molecular levels.

5. MORPHOLOGICAL AND GENETIC DYNAMICS IN FGF8 LOSS OF FUNCTION DURING MES/R1 FORMATION

5.1 Background

To understand the mechanisms that pattern the embryonic brain and lead to the morphogenesis of proper brain structure, it is useful to study perturbed systems in which the function of a gene is disrupted. Zebrafish are excellent models for such study as large-scale mutagenesis screens (the only performed in a vertebrate model) have identified many useful mutant phenotypes, morpholinos can be used to knockdown specific genes, and several new promising strategies have recently been published for site-directed mutagenesis (251). Traditional methods for analyzing loss of function experiments affecting neural patterning include standard light microscopy to evaluate morphological responses followed by in situ hybridization to evaluate shifts in gene expression domains. These techniques, while having played an important role in constructing the current model for understanding neural patterning, typically fail to provide the resolution in space and time to fully capture the interplay between genetic programs and their resultant morphological phenotypes. Yet, the complexity of these developing systems warrants more detailed examination in order to elucidate the regulatory networks governing patterning and how they translate into specific cell behaviors that drive brain morphogenesis.

5.1.1 Molecular characterization of ace phenotype

The *ace* phenotype was originally reported from one of the first large-scale mutagenesis screens in zebrafish (22) and later linked with the *fgf8a* locus (240). The null phenotype, caused by mutations that result in deletion of the receptor-binding segment of the Fgf8 protein, is described (relating to CNS development) as completely lacking the morphological midbrain-hindbrain boundary (MHB) constriction (i.e. isthmic constriction) as well as the cerebellum, which arises from the most anterior segment of the hindbrain, r1. *fgf8a* itself is initially expressed in a broad domain spanning much of the presumptive anterior hindbrain at 70% and subsequently resolves into several distinct domains including a narrow ring

at the MHB. Further analysis of the *ace* phenotype showed that genes expressed at the MHB, including *fgf8a, wnt1, pax2a, eng1/2/3,* and *her5,* are initiated normally but appear to weaken at the 5 somite stage and are no longer expressed in the boundary region by 13 somites, indicating that *fgf8a* is not required to initiate the genetic MHB program but is required for its maintenance. Closer examination of *wnt1* expression in *ace* revealed that although expression in the MHB is lost, a population of *wnt1* cells in the dorsal midbrain stripe extends posteriorly, blending into the *wnt1* domain in the posterior of r1 (22). This observation, in combination with the enlarged tectum in *ace* embryos, led researchers to suggest that without *fgf8a*, the MHB and cerebellum were transformed to a mesencephalic fate (252). To demonstrate this transformation, Jaszai et al. showed the posterior expansion of fore/midbrain marker *otx2* to the anterior limit of *epha4a* at the r1/r2 boundary in *ace* by 9 somites accompanied by a lack of expression of the cerebellar markers *zath1* and *gap43* in presumptive r1 (252). The authors argued that early molecular transformation of the presumptive boundary precluded the formation of a physical constriction at the MHB. This cerebellar-to-tectal transformation was further confirmed with lineage tracing experiments in which boundary cells were injected with diI at 10 somites and their positions evaluated at 24 hpf. Results of this experiment showed that the labeled cells marked the posterior limit of the expanded tectum in the *ace* phenotype.

5.1.2 Roles for fgf8a and wnt1 in mes/r1 development

The line of investigation described above suggests a prominent role for *fgf8a* either directly or indirectly in the initiation of the isthmic constriction in accordance with previous reports that *fgf8a* is sufficient to induce a new MHB organizer and isthmic structures when expressed ectopically in chick and zebrafish (23). Indeed, *fgf8* was put forward as "the organizer molecule" responsible for orchestrating the boundary and patterning surrounding tissues, but more recently the prominence of its role has been questioned. Otx morphants are able to specify some cerebellar neuron differentiation with (24) and without Gbx (17) in an *fgf8a* loss of function background.

Wnt1, like Fgf8, is a secreted signaling molecule that is expressed at the MHB and in mice, loss of *wnt1* leads to deletion of the mes/r1 region (18). In zebrafish, several Wnts are expressed in mes/r1 and function redundantly. Combined loss of *wnt1*, *10b,* and *3a* results in loss of MHB (20, 21). Wnt1 has recently been proposed to mediate the timing of neurogenesis in the midbrain by driving Fgf8 expression at the boundary and gradually suppressing it away from the boundary by inducing Sprouty expression so that Fgf dependent *her5* also recedes to a narrow stripe at the boundary (253). It has also been shown to have an important role in axon guidance in the CNS (26).

Wnt and Fgf have also been recently implicated in changes in epithelial cell adhesion during cranial placode formation (254) and may also have a similar role at the MHB constriction. Some would argue, however, that other "non-classical" MHB genes, such as the grainy head-like 2 transcription factor, give rise to mes/r1 morphogenesis largely independently of major patterning molecules like Wnt and Fgf (255). Several lines of evidence, including the data we present in this section, suggest otherwise.

5.1.3 Using UPM for combined lineage tracing and gene expression analysis during disrupted morphogenesis at the perturbed MHB

Mes/r1 patterning by the MHB organizer may be a particularly suitable biological system for combined lineage mapping and fate profiling analysis with UPM. During normal development, the MHB is first specified with overlapping gene expression profiles that subsequently resolve into abutting exclusive domains, and as seen the in the previous section, UPM can be used to integrate the analysis of both the history of gene expression and the current state of gene expression within a live morphological context. In cases of aberrant development, such as in *ace,* the boundary is also first specified with overlapping gene expression profiles, but the expression of these MHB genes fails to be maintained. However, since the genes were activated, fluorescent protein reporters constructed to mark specific lineages would also be activated, and the fluorescent protein perdurance can be used to differentiate whether the loss of expression is due to the loss of a structure or if the tissue is still present and the expression profiles of the

constituent cells have changed. This distinction is difficult to make with ISH alone. UPM could also be used to profile the switch in gene expression in any identified transformed cell populations.

5.2. Materials and methods

5.2.1 Generation of transgenic fgf8a morphants and mutant zebrafish lines

To induce *fgf8a* morphants (*fgf8a* MO+ and *fgf8a* MO++), 5-10 ng of translation-blocking *fgf8a* morpholino oligonucleotides (256) were injected into established Tg(*wnt1*:eGFP) lines (170) at the one-cell stage.

To create a Tg(*wnt1:*eGFP);*fgf8a*$^{x15/+}$ line, the same Tg(*wnt1*:eGFP) line as above was outcrossed to identified carriers of the *fgf8a*^{x15} allele (257). Progeny were screened for eGFP and raised to adulthood according to standard protocols. Tg(*wnt1:*eGFP);*fgf8a*$^{x15/+}$ carriers were then identified by outcrossing to previously identified carriers and checking for *ace* phenotype at 24 hpf.

5.2.2 Chromogenic in situ hybridization

To test if the response of the *wnt1*:eGFP reporter in stable Tg(*wnt1*:eGFP) lines to *fgf8a* loss of function resembles the response of endogenous *wnt1* transcripts, in situ hybridization depositing NBT/BCIP at the site of *egfp* transcripts was performed on Tg(*wnt1*:eGFP) and Tg(*wnt1*:eGFP);*fgf8a*$^{x15/x15}$ embryos as described in previous sections.

5.2.3 Fluorescent in situ hybridization

For combined lineage tracing and gene expression analysis, in situ hybridization was performed as described in previous sections with the exception that digoxegenin-labeled *wnt1* antisense probe was detected by deposition of FITC-conjugated tyramides, synthesized in house, at the site of *wnt1* transcripts according to a previously described protocol (258). Sheep anti-dig POD Ab (Roche, 11207733910) was

diluted 1:500 and incubated with embryos at 4° C overnight. FITC-tyramide conjugates were diluted 1:250 and tyramine signal amplification reaction performed for 1 hour at room temperature.

5.2.4 Ultrashort pulse microscopy

Time-lapse UPM was performed as described in Section 4 for both Tg(*wnt1*:eGFP) and Tg(*wnt1*:eGFP);*fgf8a*$^{x15/x15}$ embryos. Embryos subsequently processed for FISH were re-imaged using the same mounting method, objective lens, and filter configuration to simultaneously collect and discriminate tissue autofluorescence and fluorescence from deposited FITC.

5.2.5 Image processing

Image processing was performed as described in Section 4.

5.3. Results and discussion

5.3.1 Label-free 3-D imaging of mes/r1 in wild-type and fgf8 loss of function with UPM

We first examined changes in the morphology of the mes/r1 region due to *fgf8a* loss of function at 24 hpf by imaging live embryos with UPM. The results, shown in Fig 5.1, captured the progressive loss of the isthmic constriction with decreasing *fgf8a* activity at 24 hpf. This dorsal view was taken at the dorsoventral position of the sulcus limitans. A lateral section through the neuroepithelium shows the posteriorly expanded tectum, presumably at the expense of the dorsal r1 region (252). A transverse section through presumptive r1 shows that in wild-type embryos, the epithelial tissue is tightly adhered at the midline, but in both morphant and *ace* embryos, a large gap separates the left and right sides of the presumptive r1 (white asterisk).

The most obvious difference comparing the morphant phenotype in *fgf8a* knockdown (*fgf8a* MO+) to the *ace* phenotype in *fgf8a* loss of function (*fgf8a*$^{x15/x15}$) is the clear presence of a constriction (white arrowhead). Based on the conclusions from previous studies, we interpreted this result to be the activation of a constriction morphogenesis program in the presence of low levels of *fgf8a* activity that

failed to execute to completion. However, it was curious that the presence of this constriction could not be deduced from examining the lateral sections or a dorsal maximum-intensity projection (3-D view) of the same embryo, the views most generally used to characterize mes/r1 morphology in zebrafish.

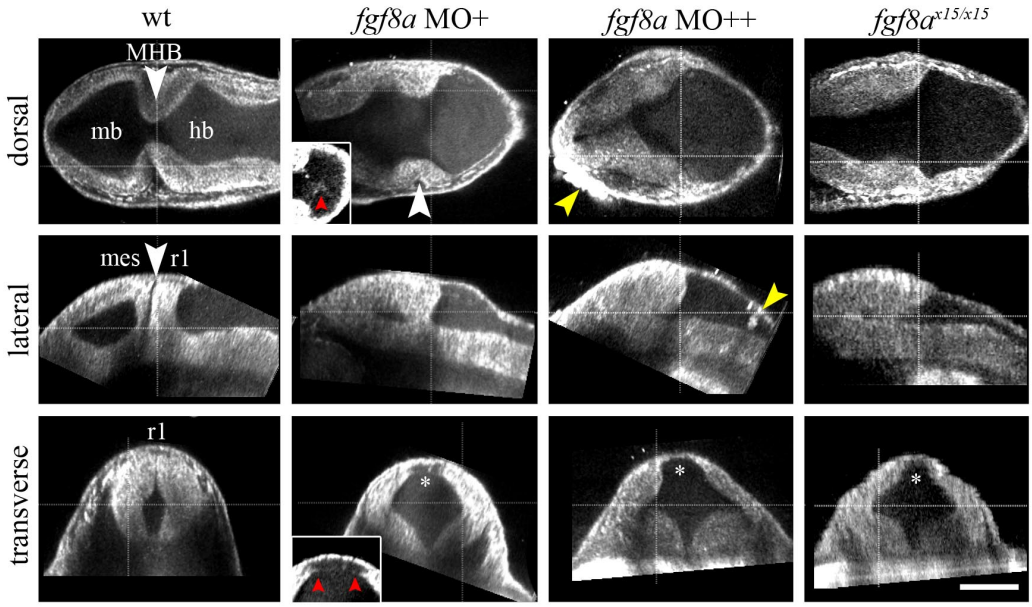

Fig 5.1 3-D comparison of the morphology in the mes/r1 region in wild-type, *fgf8a* knockdown, and *fgf8a* loss of function embryos at 24 hpf using label-free UPM. The midbrain-hindbrain boundary (MHB) constriction separating the midbrain (mb) and hindbrain (hb) (ie. Mesencephalon (mes) and rhombomere 1 (r1)) is progressively lost with decreasing *fgf8a* activity (white arrowheads), as well as cell adhesion at the midline in r1 (asterisk) marked by the presence of cellular processes in the gap in morphant embryos (red arrowheads). 10 ng/nl of translation-blocking *fgf8a* morpholino phenocopies (*fgf8a* MO++) but also induces cell stress marked by clumps of strongly autofluorescent cells (yellow arrowheads). Scale bar=100 µm.

Another feature of the morphant phenotype at 24 hpf was the presence of cell processes between the gap in dorsal r1 that are reminiscent of the processes seen during brain ventricle opening (Fig 5.1, dorsal and transverse insets). Their presence suggests a potential role for *fgf8a* or an *fgf8a* dependent process in maintaining cell adhesion at the midline in the boundary region during normal brain ventricle morphogenesis, as insufficient signaling may render dorsal r1 competent to a signal emanating from the

r1/r2 boundary that triggers hindbrain ventricle opening (Gutzman 2010). We did not observe these cellular processes in *fgf8a* MO++ or *fgf8a*$^{x15/x15}$ embryos at 24 hpf, perhaps because they had already retracted. In general, *fgf8a* MO++ embryos appeared to phenocopy *fgf8a*$^{x15/x15}$ embryos, with the important difference that groups of highly autofluorescent cells were dispersed around the neuroepithelial brain tube (yellow arrowheads) that were not present in *fgf8a*$^{x15/x15}$ embryos. As increasing autofluorescence has been associated with changes in cell metabolic state and cell stress (259), we were concerned about potential morpholino toxicity and used only *fgf8a*$^{x15/x15}$ embryos for subsequent loss of function analysis.

5.3.2 Transient constriction in fgf8 loss of function revealed with 4-D UPM

To further examine the dynamics of these morphogenetic features, we conducted time-lapse imaging with UPM in the mes/r1 region from 12 somites (t=0:00) to early pharyngula stage in wild type, *fgf8a* MO+, and *fgf8a*$^{x15/15}$ embryos. Fig 5.2 shows these dynamics as maximum intensity projections of the embryo at relevant time points excluding the roof plate. Surprisingly, a physical constriction was present at the 12 somite stage in wild type, *fgf8a* MO+, and *fgf8a*$^{x15/15}$ embryos (yellow arrowheads). In wild type embryos, as expected, the constriction matured into a narrow ring of cells separating the mesencephalon and r1. When *fgf8a* activity was diminished (*fgf8a* MO+), the constriction matured up until 8:02 at which point it began to relax. When no *fgf8a* activity was present (*fgf8a*$^{x15/15}$ embryos), the constriction matured up to 5:00 at which point it also failed to continue forming. At the end of the time-lapse, residual constrictions are still evident in both morphant and mutant embryos, especially on the basal side of the neuroepithelium (yellow arrowheads).

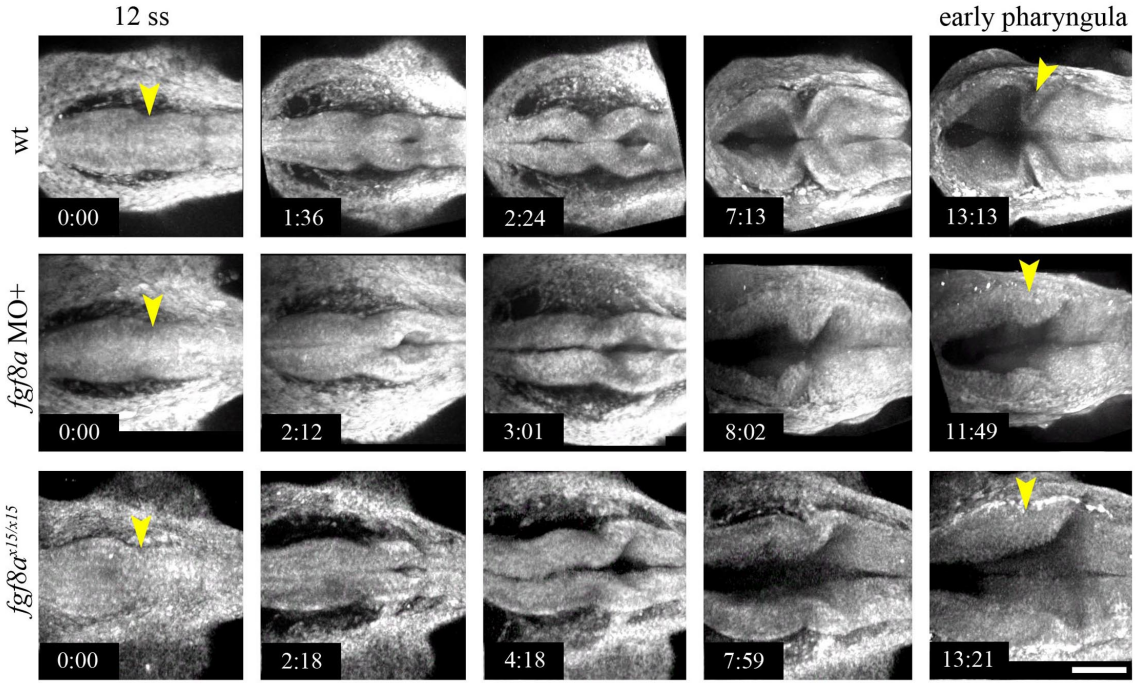

Fig 5.2 Time-lapse UPM reveals transient constriction in *fgf8a* loss of function *ace* phenotype. Wild-type, morphant (*fgf8a* MO+), and mutant (*fgf8a*$^{x15/x15}$) embryos were imaged with UPM from 12 ss (t=0:00) to early pharyngula stage. 3-D reconstructions generated using maximum intensity projection from autofluorescence signals (with sections from the roof plate removed so interior dynamics could be visualized) reveal the formation of an isthmic indentation (yellow arrowheads) that fails to mature without *fgf8a* in what appears to be a dose-dependent manner as isthmic relaxation occurs later in the presence of low levels of *fgf8a* signaling. Scale bar=100 µm.

Notably, visualizing these dynamics made it apparent that despite previous claims that the isthmic constriction fails to form in *fgf8a* loss of function embryos, a mechanism independent of *fgf8a* was able to appropriately position and initialize this physical boundary in *fgf8a*$^{x15/x15}$ embryos. The possibility of a transient constriction may have been disregarded previously due to results of gain of function studies in chick where Fgf8 soaked beads implanted in the forebrain and hindbrain were sufficient to induce ectopic MHB organizers including expression of MHB genes and a physical constriction (23), leading some to assume that *fgf8a* is necessary to initiate the constriction. However, as the dependencies of the genetic regulatory networks at the boundary shift over time, it may be the case that the morphogenetic program also has changing requirements and begins earlier than previously thought. Su et al. recently reported that

embryos lacking a combination of *otx2*, *gbx1/2,* and Fgf signaling initated cerebellar plate morphogenesis and Upper Rhombic Lip (URL) specification properly (17). What may be responsible for this initation is not clear. Under these conditions, although morphogenesis and induction occur, without Fgf signaling the MHB genetic program (by proxy of *pax2a* expression) halts and the URL fails to further develop and differentiate. Thus, the authors suggested a dual role for *fgf8a* in morphogenesis and specification, with the roles likely changing over time. Our results also indicate that *fgf8a* serves dual roles- a morphogenetic role to maintain the isthmic constriction, in addition to its role in maintaining gene regulatory networks at the MHB.

We do not know the exact cellular processes that may account for the relaxation of the transient isthmus in *fgf8a*$^{x15/x15}$ mutant embryos, but in hindbrain rhombomeres, which are transient in normal development, relaxation of the physical constriction at the boundaries is mediated by regulation of myosin II by *mypt1 (260)*. In *mypt1* mutants, hindbrain ventricles open as the midline separates, but the rhombomeres retain their constricted morphology. It would be interesting to see if *mypt1* is expressed near the MHB in *fgf8a* loss of function and could potentially disrupt a myosin-dependent contribution to the maintenance of the isthmic constriction. Gutzman et al. also showed the *mypt1* phenotype in hindbrain rhombomeres could be rescued by treatment with blebbistatin, a selective inhibitor of non-muscle myosin II. In this experiment, the MHB was not disrupted by attenuation of myosin II activity; however, the dose was low and not applied until late somitogenesis. Unpublished results by Gutzman et al. show morpholino knockdown of myosin IIa/b at the MHB induces a strikingly similar phenotype as *ace,* and differences in myosin contractility have been implicated in the evolution of brain ventricle morphology (48).

5.3.3 Brain ventricle opening begins normally but fails to be restricted in the boundary region in fgf8a loss of function

To analyze the dynamics of adhesion in the neuroepithelium of mes/r1 in wild type compared to *fgf8a* loss of function embryos, we examined lateral sections of our time-lapse data taken at the midline shown in Fig 5.3. During normal morphogenesis, hindbrain ventricle opening (ventricle IV) was initiated in the roof

plate above r2 and spread anteriorly to the r1/r2 boundary before changing axis to move ventrally. Shortly afterwards, ventricle opening spreading posteriorly from the fore- and midbrain (ventricle III) was apparent, with the midline remaining closed at the boundary (yellow arrows). Subsequently, a canal opens to connect the two ventricles in the ventral part of the boundary region. In both *fgf8* MO+ and *fgf8a*$^{x15/x15}$ embryos, this progression appears to initiate normally, albeit slightly delayed, compared to wild type controls, but by 3:00 the opening of the canal has progressed farther than in wild type (yellow arrows) and by 8:00 the dorsal neuroepithelium at the boundary has separated (asterisk). This aspect of the *ace* phenotype does not appear to be overtly dose-dependent, although a very slight anterior-most portion of dorsal r1 remained adhered at 8:33 and to the end of the time-lapse in the *fgf8a* MO+ embryo. This slight adhesion retained in low levels of *fgf8a* activity (red arrowhead) may account for the difference in the relative onset of isthmic relaxation shown in Fig 5.2. When *fgf8a* activity was knocked down, the majority of delamination in the boundary region preceded relaxation of the constriction but when *fgf8a* activity was completely lost, delamination and isthmic relaxation occurred in tandem.

Previously, increased levels of cell death were observed in dorsal r1 in *ace* mutants during mid-somitogenesis using TUNEL staining (240) and attributed to apoptosis following an r1-to-mesencephalic identity change. A similar Fgf8$^{-/-}$ phenotype was in mice (19). While such a phenomenon could potentially explain the loss of adhesion we have seen in dorsal r1, we have not observed any increase in autofluorescence signals that may indicate such events occurring in *fgf8a*$^{x15/x15}$ embryos. Instead, we argue that *fgf8a* plays a role in maintaining adhesion during normal development. Interestingly, the limits to which the initially broad *fgf8a* domain narrow (initially spanning r1-r4 and narrowed to discrete domains in r1, ventral r2, and r4) (240), mirrors the curious sequence of hindbrain ventricle opening in more posterior rhombomeres. Ventricles open first at the dorsal r1/r2 interface (our observations), followed by small openings at the r3/r4 and r4/5 boundaries (260). In Gutzman et al., r4 subsequently separates at seemingly the same time *fgf8a* expression is lost in r4 (261) and forebrain domains of *fgf8a* expression also correspond with areas that shape forebrain ventricle morphology. Also, in the combined *otx*/*gbx* loss of function experiments conducted by Su et al., during somitogenesis, a large *fgf8a* domain at the

boundary corresponded with an abnormally long constriction where cells seemed unable to properly delaminate at their apical interface. These results, combined with the dynamics we have captured, point to *fgf8a* as a necessary factor for maintaining adhesion at brain ventricle boundaries.

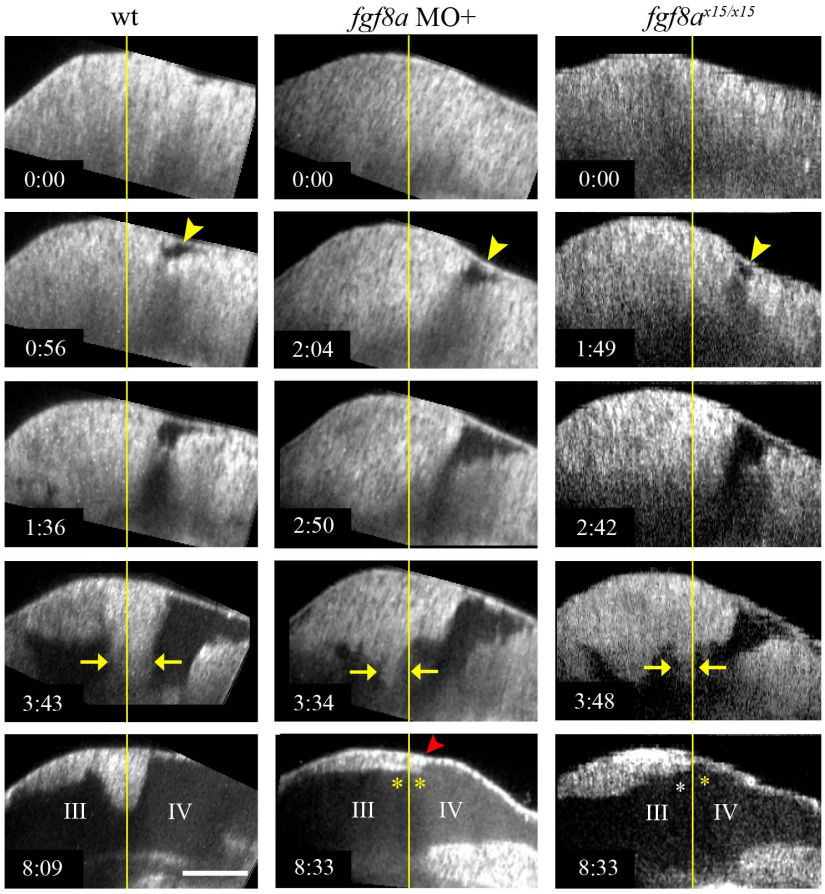

Fig 5.3 *fgf8a* is required for maintaining adhesion of the neuroepithelium in the boundary region during brain ventricle formation and mes/r1 morphogenesis. Opening of ventricle IV initiates normally, but slightly delayed (yellow arrowhead), with diminished and abolished *fgf8a* activity at relatively the same position posterior to the MHB constriction (yellow line) in the roof plate of r2. Later, accelerated delamination of the ventral boundary region is evident (yellow arrows) compared to wild-type embryos and spreads to the dorsal boundary region (yellow asterisk) on both sides of the physical constriction. A small portion of r1 remains adhered in *fgf8a* MO+ embryos (red arrowhead). Scale bar=100 µm.

Hindbrain opening initiates normally, but spreads anteriorly, possibly due to the failure to maintain the MHB genetic program without *fgf8a*. Thus, the role played by *fgf8a* in maintaining adhesion is likely indirect- *fgf8a* may be required to maintain the expression of directly responsible genes during this part of MHB formation. Adhesion loss at the midline progresses strikingly in step with the loss of *eng2* and *pax2a* expression patterns in *ace* at the MHB (240) and *eng2*, like *fgf8a,* is not present in r4 when ventricle IV opens there. It would be interesting to examine these patterns in detail to see if *eng2* or *pax2a* are expressed more in cells at the midline and potentially mediate adhesion maintenance. *wnt1*, *eng1.b, pax2a,* and *il17rd* overlap with *fgf8a* in that region and would be candidates genes that help to mediate this *fgf8a* dependent separation in mes/r1.

5.3.4 Proper formation of dorsoventral and anteroposterior morphology in mes/r1 require fgf8a

Having already discovered surprising features in *fgf8a* knockdown and loss of function embryos, we examined the data to generally characterize dynamic morphological differences along the anteroposterior and dorsoventral boundary. In the study described in the previous section, we noticed qualitative differences in the sharpness of the MHB constriction depending on dorsoventral position, which is not surprising considering the dorsal and ventral regions give rise to different structures in the adult brain (optic tectum and cerebellum, and tegmentum respectively). We first examined the angle of the MHB constriction quantitatively from dorsal sections in the roof plate, at the alar/basal boundary (which generally coincides with the sulcus limitans), and in the floor plate. These values, taken from a single embryo over time, are displayed in Fig 5.4. Each semicircle represents the right side of mes/r1 in an embryo at a specific point in time, with the different color outlines corresponding to the position and value of the constriction angle in different dorsoventral locations (Fig 5.4A,B).

In all embryos, the constriction is already present at 12 somites (t=0:00). In wild-type embryos, there was little variation in the constriction angle along the dorsoventral axis initially, but as time progressed, the behavior of the tissue surrounding the constriction began to diverge with dorsal tissues creating the sharpest constriction and ventral tissues creating only a moderate constriction. This difference

is presumably due to the rapid growth of the tectal lobes in the dorsal mesencephalon. When *fgf8a* activity is knocked down or lost, at 12 somites the mesencephalon has a similar constriction angle in the dorsal region of the boundary but is more relaxed in the middle and ventral region. This difference reflects the taller, narrower mesencephalon characteristic of the *ace* phenotype at this stage (see also transverse sections in Fig 5.5). As time progressed, in both *fgf8a* knockdown and loss of function embryos, the morphogenesis of the tectal lobes failed as can be seen by the fact the posterior limit of the lobes never crossed the transverse plane of the constriction as seen in wild type. This failure could be due to insufficient growth of the tectal tissue, lack of mechanical stability of the boundary, or a combination of both. Interestingly, in *fgf8a* knock down, there is a regression of the constriction at 3:57, which corresponds to the time that adhesion at the midline of r1 begins to be lost, but then the tectum apparently re-stabilizes. The regression and recovery of the MHB angle in the dorsal region of the *fgf8a* MO+ embryo may reflect the retention of epithelial constriction by low levels of *fgf8a* signaling despite the loss of adhesion at most of the midline at r1. Dynamics of the constriction at the alar/basal boundary show a less sharp constriction, while the constriction in the floor plate is comparable to wild type. In *fgf8a* loss of function embryos, in the roof plate the constriction does not mature appreciably, but at the alar/basal boundary it sharpens until about 5:00 and relaxes. In the floor plate the angle is similar to wild type until 7:34, but it also relaxes during the rest of the time course.

From this analysis, it would seem there are different mechanical forces exerted on the isthmic constriction along the dorsoventral axis of the tube during somitogenesis, which would potentially lead to different strategies in the dorsal and ventral compartments to maintain the mechanical integrity of the boundary for proper formation of the surrounding tissue. Shortening and subsequent basal-constriction of cells at the MHB has been implicated as one mechanism to mechanically stabilize the constriction (262); however, as the constriction is treated as virtually a two-dimensional object in most literature, it is difficult to interpret from where along the dorsoventral axis data is reported. It seems reasonable to assume that most reports focus on the dorsal compartment as, even in the relatively transparent zebrafish, it is easier to image.

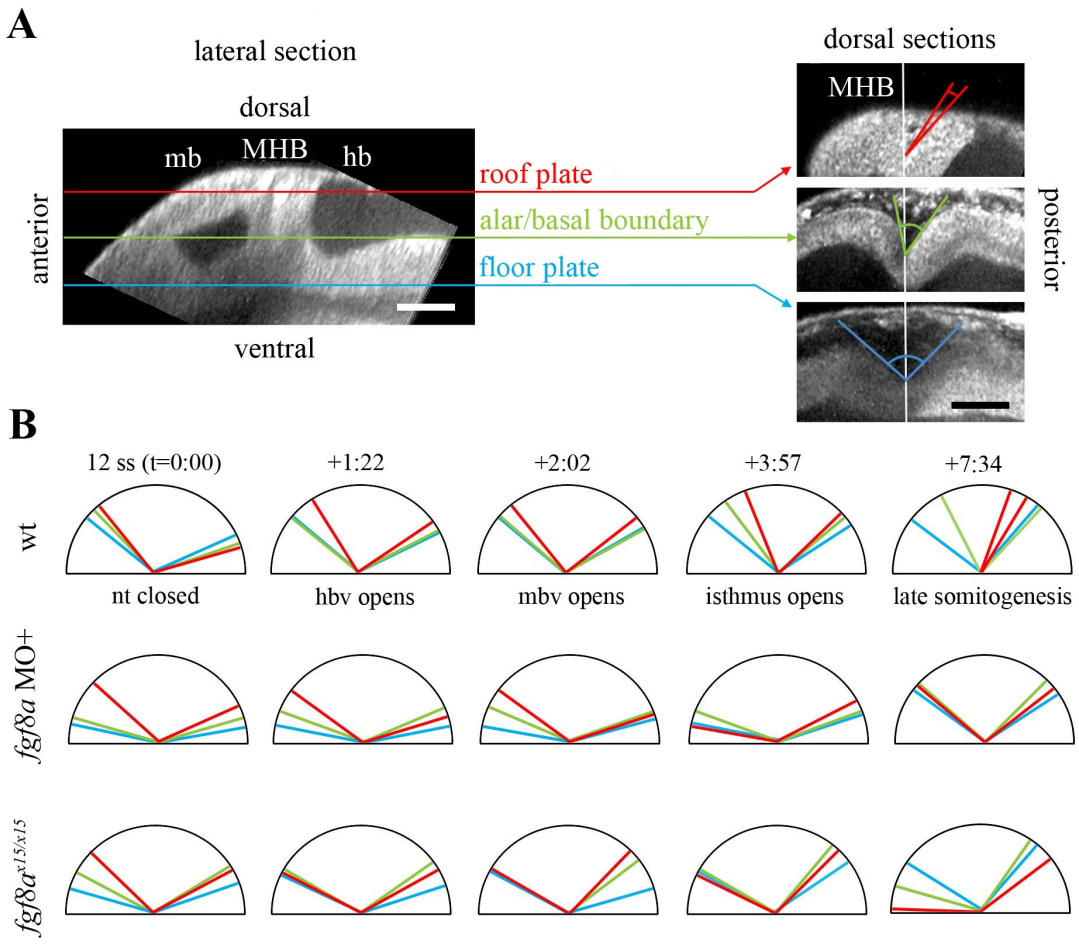

Fig 5.4 Differences in MHB angle sharpness depending on dorsoventral position. (A) Three different dorsal sections, one through the roof plate (red), one at the alar/basal boundary (green), and one in the floor plate (blue) of the neuroepithelium were used to quantify MHB angle sharpness. (B) The dorsoventral dynamics of the constriction angle show that in normal development, the constriction is sharpest in the dorsal region, which also corresponds to the region most disrupted in *fgf8a* knock down and loss of function. Scale bar = 50 µm.

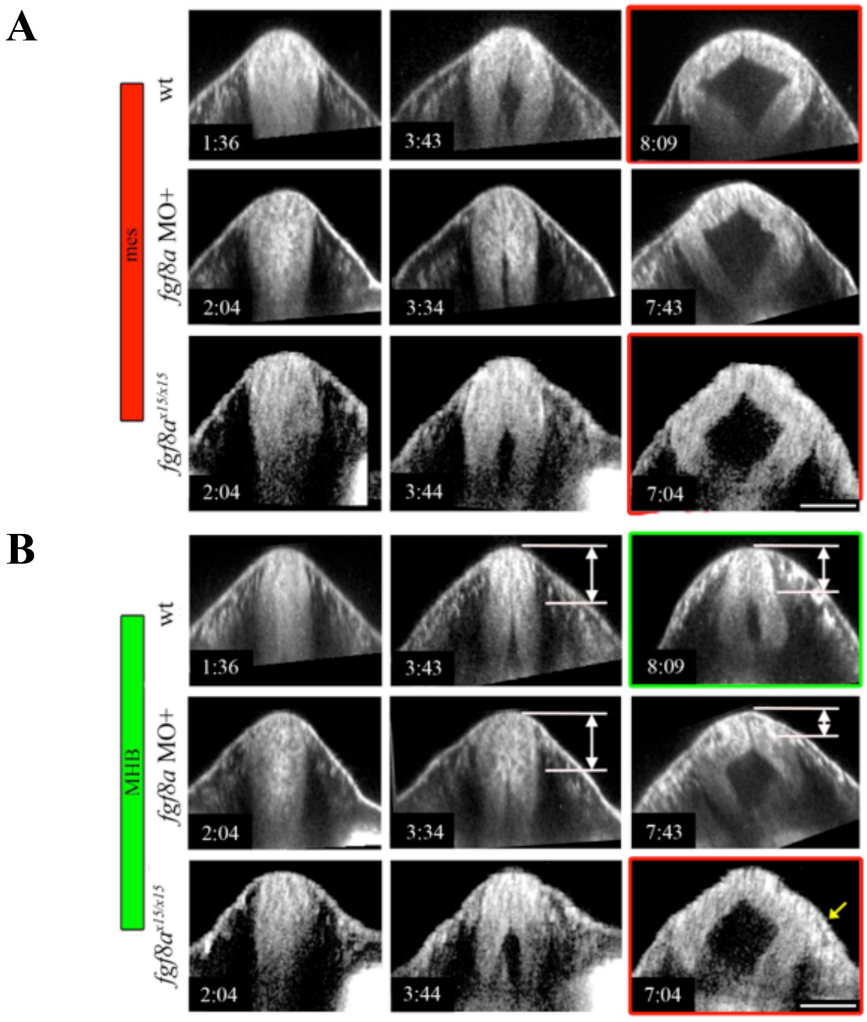

Fig 5.5 Boundary and r1 ventricle morphogenesis resembles mesencephalon ventricle morphogenesis in *fgf8* loss of function. Along the A/P axis, neuroepithelial morphology is initially uniform but diverges to distinct transverse morphologies in wild type embryos. In comparison, *fgf8a* knock down dampens these difference (white markers) and *fgf8a* loss of function results in no appreciable morphological difference along the A/P boundary except for a gap in the dorsal region of r1 (asterisk). A denser mesenchyme surrounded the boundary and r1 compartments in *fgf8ax15/x15* embryos (yellow arrow), which may be due to more neural crest migration from these compartments than in wild type embryos. Scale bar = 100 µm.

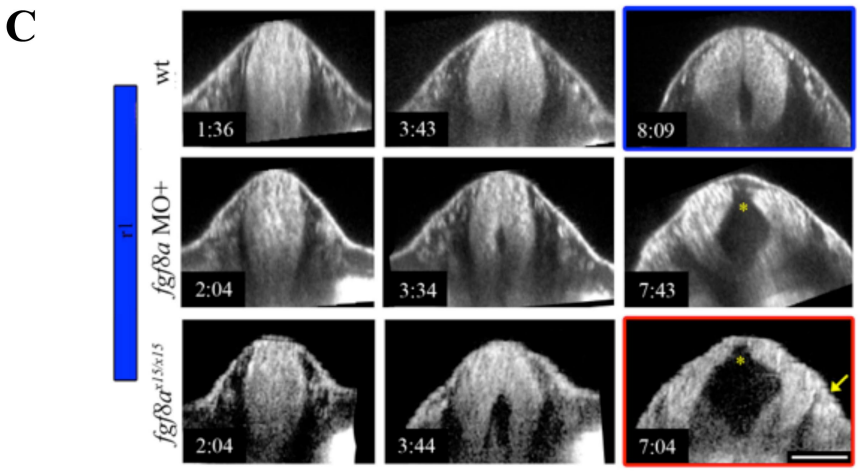

Fig 5.5 Continued.

We next examined the dynamics of the transverse morphology of the brain ventricles along the anteroposterior axis in wild type, *fgf8a* knock down, and *fgf8a* loss of function embryos shown in Fig 5.5. Along this axis, sections were taken through the widest point of the mesencephalon (red panel), at the narrowest point of the MHB constriction (green panel), and at the widest point in r1 (blue panel). Before brain ventricle morphogenesis, the transverse morphology of the neural tube is similar along the entire anteroposterior axis in all groups of embryos. When ventricles III and IV connect, there is still relatively little difference between wild type and *fgf8a* MO+ embryos that have begun to take on distinct morphologies in the different anteroposterior compartments; however, in *fgf8a*$^{x15/x15}$ embryos, the morphology still appears consistent along the entire axis. By 8:00, wild-type embryos have a characteristic kite-shaped transverse ventricle morphology in the mesencephalon (red outline), a narrow isthmus at the MHB constriction with a cap of tightly adhered cells in the dorsal part of the constriction (green outline, white marker), and a thickened epithelium in r1 known as the rhombic lips (blue outline). *fgf8a* MO+ embryos at this point have transverse morphology that resembles wild type embryos in the mesencephalon, and an intermediate appearance between wild type and mutant morphology at the MHB constriction and r1. *fgf8a*$^{x15/x15}$ embryos retain the transverse morphology of the midbrain compared to wild type, and this same morphology propagates along the anteroposterior axis through the boundary and r1,

with the notable exception of the gap separating the left and right portions of r1. In *fgf8a*$^{x15/x15}$ embryos, we also observed a higher occupancy of autofluorescence signal in the mesenchyme surrounding the neuroepithelium near the boundary and r1 (yellow arrow), which suggests there could be more neural crest migration from these regions in *fgf8a*$^{x15/x15}$ embryos compared to *fgf8a* knock down or wild type embryos.

From these results, we conclude that the default morphology in r1 is mesencephalic in nature without *fgf8a* and the MHB genetic program to properly maintain the MHB constriction. This result is consistent with a cerebellar-to-tectal transformation of the boundary/r1 region. We were, however, surprised to see what appeared to be more neural crest migrating from the boundary/r1 when *fgf8a* signaling was not present. It is interesting to consider whether the narrower epithelium in the dorsal region of r1 in *fgf8a*$^{x15/x15}$ embryos may be due to its depletion from a larger than normal population of neural crest cells migrating from r1, possibly resulting in a smaller than necessary progenitor pool within the cerebellar plate primordium similar to what has been seen in spinal cord dorsoventral patterning (263).

Having examined in detail the dynamics of brain ventricle opening relative to MHB morphogenesis, it appears that one function of the MHB constriction is to serve as a node for a transition between different anterior and posterior brain ventricle morphogenesis programs converging at the boundary. Such a structure would need to maintain cell adhesion at the boundary until brain ventricle morphology was established on the limits of either side to prevent misspecification of the surrounding tissues and could also mediate the timing of signaling between anterior and posterior brain compartments in the case of signaling molecules secreted in the cerebrospinal fluid. Such phenomena are not without precedent; for example, in mouse embryos it is well known that left/right asymmetry is broken by cilia-directed fluid flow in the node, though it is not known if the signal mediated through the unidirectional fluid flow is mechanical or chemical in nature (264). Brain ventricles have been shown to have cilia, and in zebrafish cilia in the developing telencephalon were shown to direct neuronal migration (265). Some such mechanism may account for the evolution of the closed primary neurulation strategy that transitions through a neural keel seen in zebrafish compared to neural tube infolding seen in other vertebrates.

5.3.5 Neural crest differences in fgf8a loss of function

To further examine the hypothesis that the denser mesenchyme surrounding the MHB and r1in *fg8a*$^{x15/x15}$ embryos is due to enhanced neural crest migration from those regions, we examined dorsal sections of wild type, *fgf8a* MO+, and *fgf8a*$^{x15/x15}$ embryos near the roof plate shown in Fig 5.6. At the beginning of the time-lapse experiments at the 12 ss, neural crest streams from r1 were already evident, as well as some neural crest cells migrating from the mesencephalon in wild type, *fgf8a* MO+, and *fgf8a*$^{x15/x15}$ embryos. By 5:00, neural crest migration from r1 appears to have stopped in wild-type embryos, compared to the corresponding time in *fgf8a*$^{x15/x15}$ embryos in which we observed cells in dorsal r1 still transitioning from an epithelial to mesenchymal nature (green arrow). In *fgf8a* knock down, we could not conclude if any cells were still migrating from r1 at 5:00.

Another feature of neural crest migration we observed that differed in these groups was the avoidance of a particular area in the head mesenchyme adjacent to the anterior mesencephalon (asterisk) and posterior to the optic cup that may correspond to the trigeminal placode (156). In *fgf8a* knock down, this region was reduced and in *fgf8a* loss of function, this area was absent.

Cranial neural crest have not been well-studied in zebrafish, so it is difficult to tell if our interpretation of the dynamics of the waves of neural crest migration observed match what is previously known. From this data, however, it appears that small levels of *fgf8a* signaling may restrict neural crest migration during late somitogenesis and loss of *fgf8a* signaling may contribute to the failure of this restriction. This behavior corresponds with constriction relaxation, and thus could be a consequence of the reprogramming of r1 to mesencephalic fate. Acquiring a mesencephalic identity may trigger a wave of migration associated with a more anterior position despite normal r1 migration having already taken place. Alternatively, this observation could represent a premature and aberrant migration of another group of cells from the URL, such as the *wnt1+* cells that migrate to tegmental hindbrain nuclei (34).

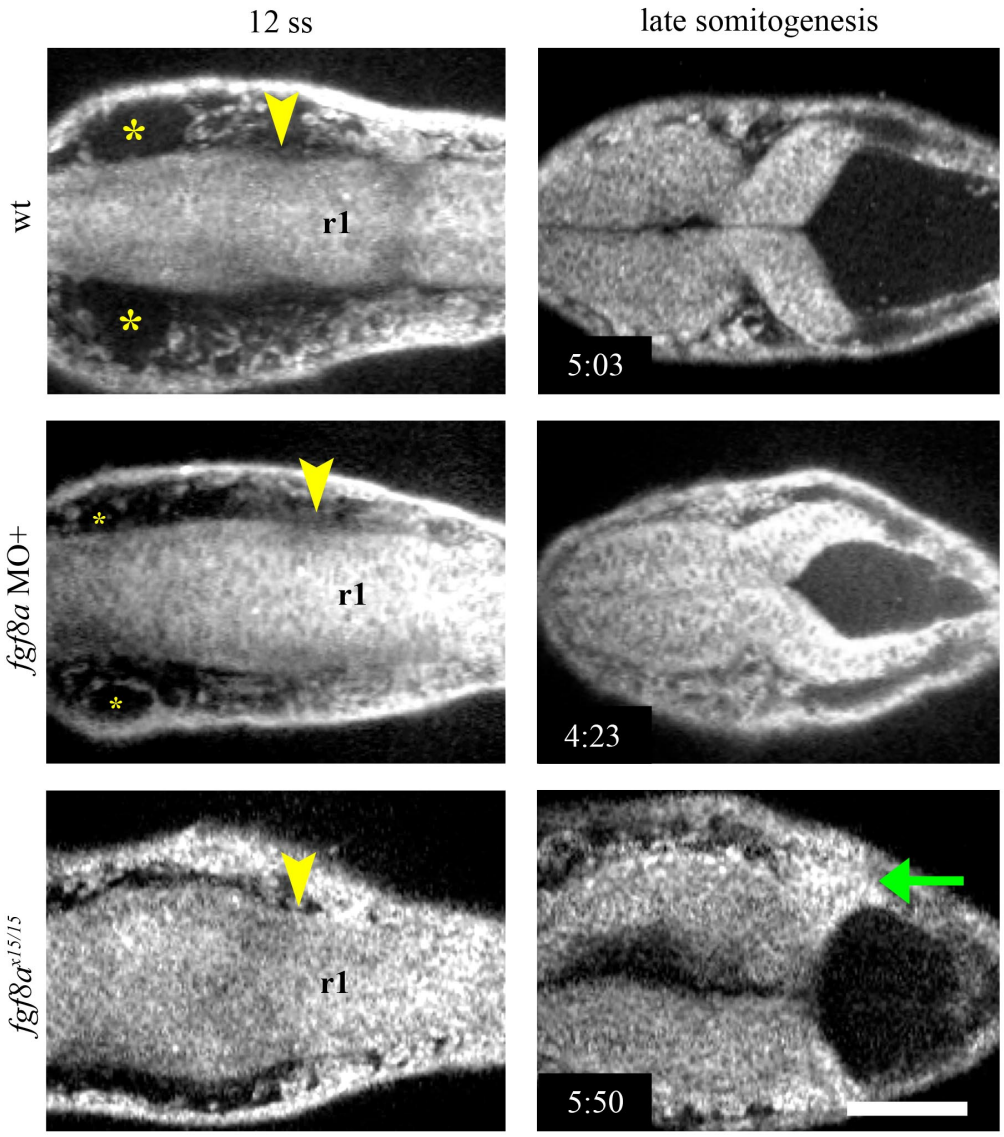

Fig 5.6 Cell migration from r1 persists longer in *fgf8a* loss of function embryos. Neural crest streams from the boundary (yellow arrowhead, constriction) and r1 seem to have ceased migration by 5:00, whereas in *fgf8a* loss of function there are still cells migrating from r1 (green arrow). What may be the trigeminal placode (yellow asterisk) is diminished with increasing loss of *fgf8a* activity. Scale bar = 100 µm.

5.3.6 wnt1 reporter transgene responds to fgf8a loss of function

We next set out to determine how these morphological changes in *fgf8a* loss of function correlated with changes in the behavior of the *wnt1* lineage using a stable Tg(*wnt1*:eGFP);*fgf8a*$^{x15/+}$ line. We tested whether the Tg(*wnt1*:eGFP) construct in these lines responds to *fgf8a* loss of function similarly to wild type by performing in situ hybridization on embryos at 24 hpf and comparing the location of *egfp* transcripts to the previously reported location of *wnt1* transcripts in *fgf8a* loss of function. Fig 5.7 shows these results, where at 24 hpf in Tg(*wnt1*:eGFP);*fgf8a*$^{x15/+}$ embryos, the *egfp* reporter transcript is found in a dorsal stripe along the midbrain and hindbrain, except for a gap (asterisk) in anterior r1, as well as throughout the dorsoventral axis of the MHB boundary (black arrowhead), which matches the expression of endogenous *wnt1* in a wild-type background (170). In Tg(*wnt1*:eGFP);*fgf8a*$^{x15/x15}$ embryos, the expression at the MHB boundary is lost (asterisk) and the dorsal stripe runs continuously from the midbrain through the presumptive transformed r1 region to the hindbrain (black arrowhead).

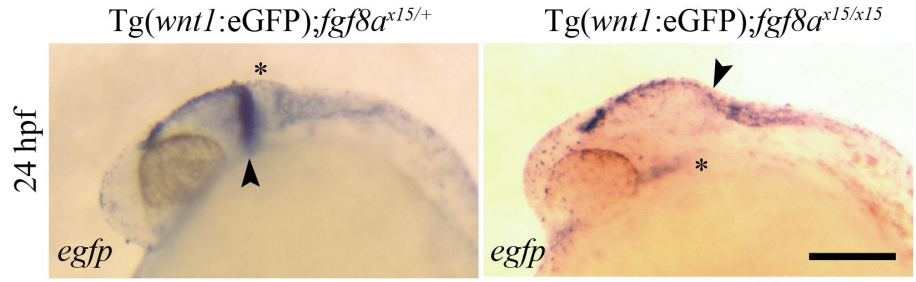

Fig 5.7 *wnt1* reporter is responsive to *fgf8a* loss of function in a stable Tg(*wnt1*:eGFP);*fgf8a*$^{x15/+}$ line. With normal *fgf8a* function, *egfp* transcripts in Tg(*wnt1*:eGFP);*fgf8a*$^{x15/+}$ embryos match endogenous *wnt1* expression at the MHB boundary (black arrowhead) and in the dorsal midbrain and hindbrain, including a gap in anterior r1 (asterisk). Without *fgf8a, egfp* transcripts in Tg(*wnt1*:eGFP);*fgf8a*$^{x15/x15}$ were found in the dorsal midbrain in a continuous stripe through the transformed r1 region into the hindbrain (black arrowhead), but not at the MHB boundary (asterisk), matching the *wnt1* expression pattern in *ace* phenotype. Scale bar = 200 µm.

We concluded this transgenic line was suitable for analyzing the dynamics of *wnt1* in *fgf8a* loss of function as the reporter transcript responds the same as the endogenous *wnt1* transcript. Therefore, we could use time-lapse UPM of this Tg(*wnt1*:eGFP);*fgf8a*$^{x15/+}$ line to visualize the eGFP marked *wnt1* lineage within mes/r1 during normal morphogenesis and during the isthmo/cerebellar-to-tectal transformation when *fgf8a* function was lost.

5.3.7 Lineage tracing dynamics show a genetic boundary forms at the transient constriction but does not sharpen properly

We previously showed that the narrow ring of *wnt1* expression is refined from a broader domain of expression by different cell behaviors depending on their dorsoventral position. During normal development, the *wnt1* lineage was present throughout dorsal r1 and these cells remained marked by GFP up to early pharyngula stages, though active *wnt1* expression marked by the deposition of NBT/BCIP in those embryos had receded to the dorsal stripe in the mesencephalon and in a ring just anterior to the boundary. In contrast, in the ventral part of r1, the *wnt1* lineage extended less posteriorly and over time the GFP signal dropped sharply, indicating the movement of these cells relative to the MHB boundary, perhaps either sorting into the midbrain or dorsal r1. The MHB boundary has been shown to be lineage restricted during this phase of development (44) but the data presented in that study extended only to the most upper portion of the ventral compartment.

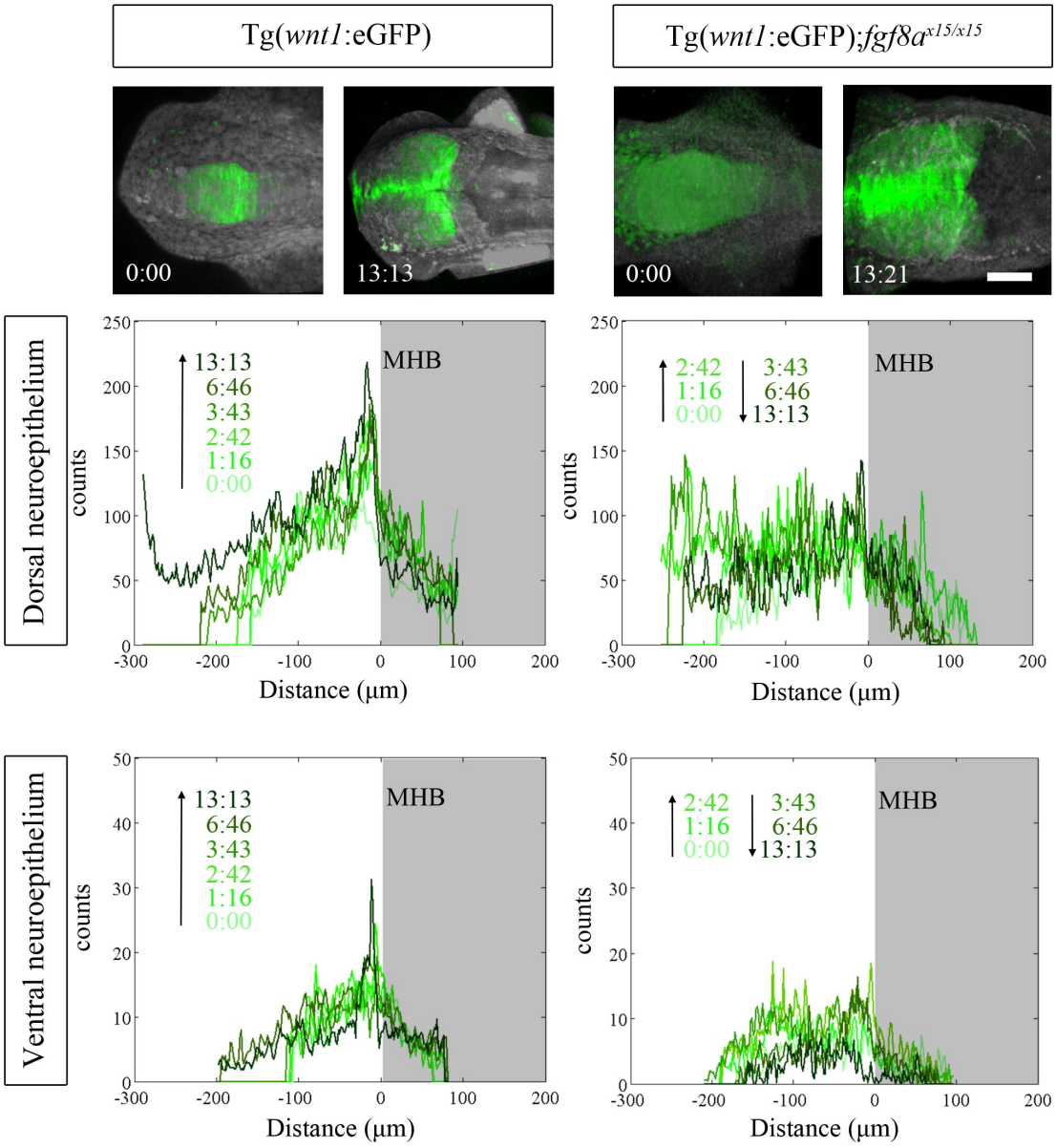

Fig 5.8 *wnt1* lineage is present but unpolarized in Tg(*wnt1:*eGFP);*fgf8a*$^{x15/x15}$ embryos. During normal development, the *wnt1* lineage increases expression of *wnt1* visualized by increasing eGFP reporter signal at the MHB boundary in both the dorsal and ventral neuroepithelium. In *fgf8a* loss of function, this genetic *wnt1* lineage is present but its anteroposterior polarization is disorganized and GFP intensity increases and then decreases over time. Scale bar = 100 µm.

We observed the same behavior of the *wnt1* lineage in the dorsal and ventral neuroepithelium in Tg(*wnt1*:eGFP) embryos shown in Fig 5.8. Maximum intensity projections of overlaid autofluorescence and GFP signals show the dramatic morphological development of the mes/r1 neuroepithelium during somitogenesis. Tracing the GFP intensity profile of cells in the mes/r1 neuroepithlium over time showed increasing GFP signal at the MHB boundary (from the 12 ss at t=0:00 to early pharyngula at 13:13) in both dorsal and ventral compartments. In contrast, in Tg(*wnt1:*eGFP);*fgf8a*$^{x15/x15}$ embryos, we observed a bounded *wnt1* lineage in the dorsal and ventral neuroepithelium, but GFP intensity at the anterior and posterior boundaries was similar, suggesting an unpolarized domain of *wnt1* expression, and appreciable amounts of GFP did not build up over time at the boundary. Similar to normal development, GFP perdurance marked a *wnt1* sublineage remaining in dorsal r1 while the *wnt1* lineage in ventral r1 appeared to move from that compartment to a new location as GFP intensity dropped appreciably in ventral r1.

It has been suggested previously that an Fgf signaling gradient from the MHB organizer serves to polarize the developing midbrain (266) resulting in proper growth of the tectal lobes and differentiation of cell types along the A/P axis. Our results are consistent with this hypothesis, showing a mirrored distribution of GFP signal intensity in the mesencephalic neuroepithelium that suggests the boundaries are present, but the cells lack positional cues to be able to determine whether they are at the anterior or posterior boundary. Alternatively, when faced with the loss of the posterior boundary, the cells may acquire a default mesencephalic nature.

5.3.8 Integrated analysis of morphogenesis and lineage tracing in fgf8a loss of function reveals wnt1 reporter intensity increases in r1 preceding boundary relaxation

We next analyzed the genetic and morphological basis of the isthmo/tectal-to-cerebellar transformation that has been reported in *fgf8a* loss of function by tracking the fluorescence intensity of Tg(*wnt1:*eGFP) in dorsal r1 relative to the MHB constriction angle taken at the sulcus limitans, as shown in Fig 5.9. We found that in wild type embryos, the intensity of the *wnt1* reporter, measured from the dorsal region of a transverse section in anterior r1, decreased slowly over time, while the MHB angle steadily sharpened. In

contrast, in Tg(*wnt1*:eGFP);*fgf8a*$^{x15/x15}$ embryos, *wnt1* reporter intensity in dorsal r1 increased steadily over time, and this increase preceded the relaxation of the boundary that began at approximately 300 minutes (red arrowhead).

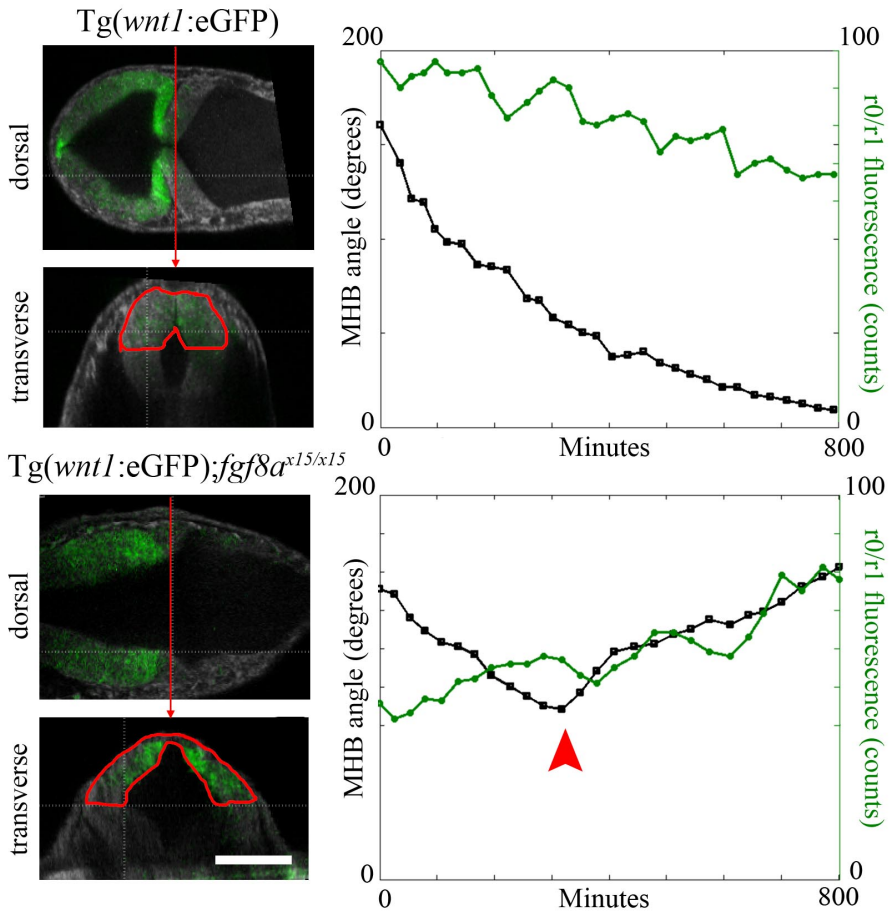

Fig 5.9 Increased reporter intensity in dorsal r1 precedes boundary relaxation in Tg(*wnt1*:eGFP);*fgf8a*$^{x15/x15}$ embryos. Transverse sections were taken in the anterior of r1 just posterior to the MHB boundary and the GFP intensity in the dorsal region (outline in red) and MHB constriction angle at the sulcus limitans were measured over time. Plots of these morphological (black line) and genetic (green line) dynamics show that in *fgf8a* loss of function, MHB boundary relaxation (red arrowhead) occurs after the reporter intensity in r1 has begun increasing. Scale bar = 150 µm.

The dynamics we measured support previous reports of an isthmo/cerebellar-to-tectal transformation that occurs with genetic reprogramming, as the *wnt1* lineage in dorsal r1 that should have stopped expressing *wnt1* and acquire a cerebellar identity (except for a handful of cells that will continue to express *wnt1* in the cerebellar plate (34)) rather continued to express *wnt1,* reflecting a potential dorsal mesencephalic identity. We observed that this reprogramming caused by a lack of *fgf8a* does not preclude the initiation of the morphogenesis of the boundary, but it does prevent it from executing properly.

5.3.9 Dorsoventral differences in response of wnt1 sublineages to fgf8a loss of function

We noted that there appeared to be two different responses among the *wnt1* lineage to *fgf8a* loss of function depending on spatial position. The above results from dynamic lineage tracing showed that cells of the *wnt1* lineage in dorsal r1 appear to either fail to stop expressing *wnt1* to resolve the genetic MHB boundary or briefly stop and then begin re-expressing *wnt1* as part of the isthmo/cerebellar-to-tectal transformation. This behavior differs from the *wnt1* sublineage at the MHB boundary in the mesencephalon that loses expression of *wnt1* as seen by ISH analysis. It was intriguing to us that, unlike other genes in the MHB program that completely lose expression in mes/r1 without *fgf8a,* such as *eng* and *pax* genes, *wnt1* responds in part to *fgf8a* loss of function by sustaining or reactivating expression in a population of cells in the presumptive dorsal r1 region.

We looked more closely at fluctuations in GFP intensity from individual cells in the dorsal mes/r1 as shown in Fig 5.10. By 7:00 (t = 0:00 at the 12 ss), adhesion has been lost and the constriction has started relaxing in *fgf8a* loss of function. When we examined the GFP intensity distribution (green line) from dorsal sections in Tg(*wnt1:*eGFP) compared to Tg(*wnt1*:eGFP);*fgf8a*$^{x15/x15}$ embryos at this point, we observed in both cases the presence of individual boundary cells with high levels of GFP anterior to the physical constriction (red rectangle). In both cases, we also observed individual cells in r1that had higher GFP intensity than their neighbors (red asterisk) and could observe peaks from the cell in r1 posterior to the physical constriction (yellow arrowheads). In Tg(*wnt1*:eGFP) embryos, we observed that from 7:00 to 13:00, the cell from the *wnt1* lineage in the mesencephalon maintained a high GFP intensity relative to its

neighbor in r1, concomitant with the maintenance of a basal-constricted cell morphology and increasing sharpness of MHB constriction. In contrast, from 7:00 to 13:00 in Tg(*wnt1*:eGFP);*fgf8a*$^{x15/x15}$ embryos, we observed the cell from the *wnt1* lineage in r1increased in GFP intensity relative to its neighbor in the mesencephalon, corresponding with what appears to also be a basal-constricted morphology that correlates with decreasing MHB angle. In both Tg(*wnt1*:eGFP) and Tg(*wnt1*:eGFP);*fgf8a*$^{x15/x15}$ embryos, cells at more posterior positions in dorsal r1 (red asterisk) that initially have higher GFP intensity decrease over time. This combination of behaviors may reflect the spread of a response to *fgf8a* loss of function from the anterior to posterior limits of r1, in which cells having determined to be specified to r1fate are reprogrammed to mesencephalic fate.

Though the results above show the increases in reporter intensity happening at nearly the same time the constriction physically relaxes, when using a reporter gene such as GFP, there is a delay between when the gene expression changes occur and when they are translated into changes in reporter intensity. This delay can lead to difficulties interpreting whether morphological changes are preceded by, occur concomitantly with, or precede changes changes in gene expression and the translation of a protein product, though such knowledge would be useful in understanding the regulatory interactions between cells and their mechanical environments. In our results shown in Fig 5.9 and Fig 5.10, increases in reporter intensity occurred at the same time the morphological environment is changed. If we assume an hour is required for fluorescent protein maturation (267), then it is reasonable to conclude that gene expression changes precede these morphological failures, but it is unclear if those changes in gene expression have been translated into changes in signaling protein and transcription factor to effect morphological change. In this context, it is reasonable to hypothesize that early posterior expansion of *otx2* in *ace* embryos signaled a fate transformation that precluded the morphogenetic program driving the constriction; however, we find that when *fgf8a* is not present to maintain expression of MHB genes, the morphogenetic program is initiated but responds to loss MHB gene expression by relaxing the dorsal boundary. In light of this, it would also be interesting to consider whether changes in mechanical environment in *fgf8a* mutants could be the change sensed by boundary cells that subsequently results in loss of MHB gene expression.

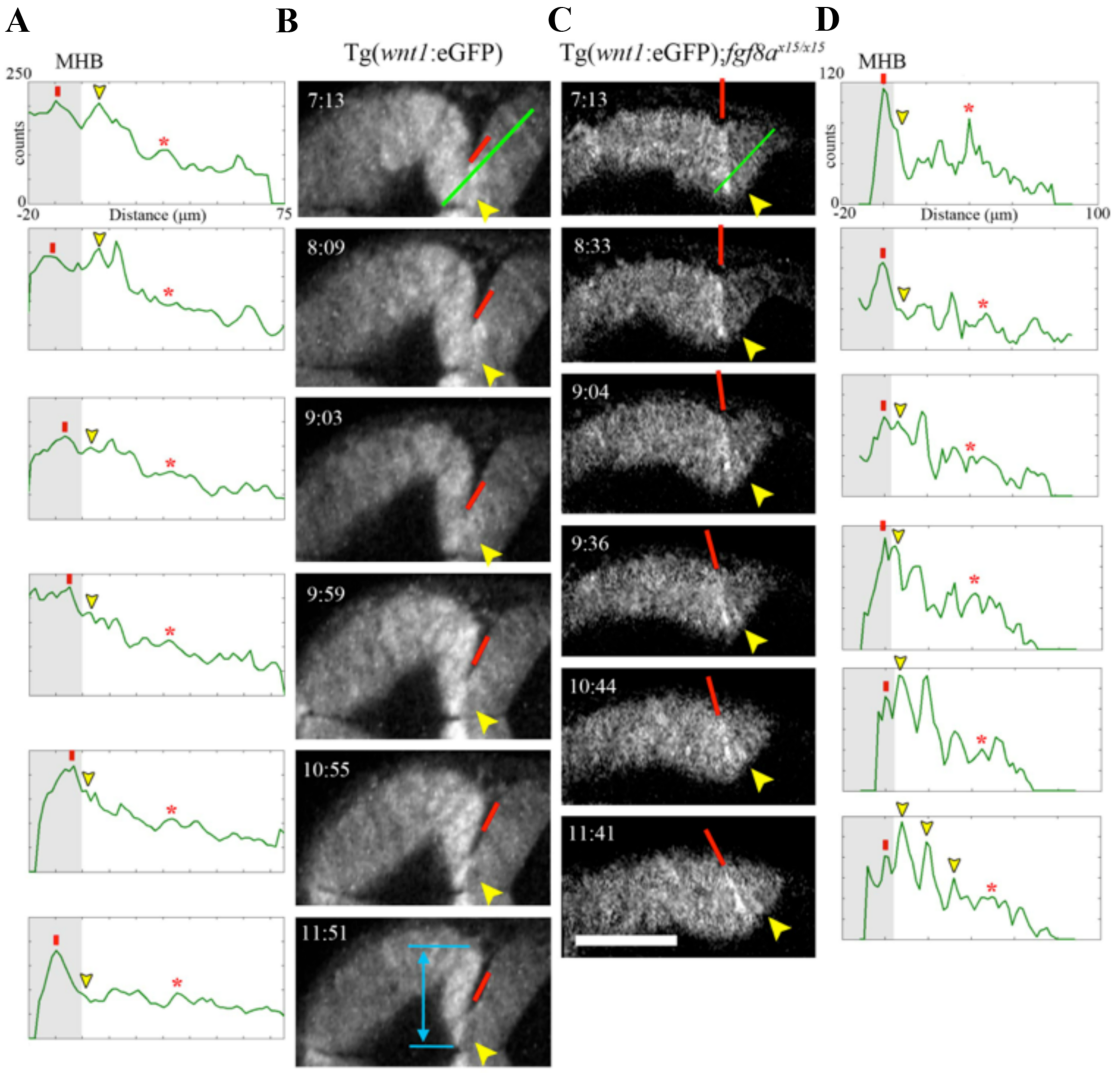

Fig 5.10 Individual cell tracking reveals increases in intensity in cells in r1 occurs with the relaxation of the boundary in dorsal mes/r1 in Tg(*wnt1:*eGFP);*fgf8a*$^{x15/x15}$ embryos. (A, B) During mid-somitogeneis to early pharyngula, Tg(*wnt1*:eGFP) embryos maintained and sharpened the isthmic constriction in part by basal-constriction of boundary cells (red rectangle) while neighbors in r1 (yellow arrowhead) displayed decreasing *wnt1* reporter fluorescence intensity (intensity profile measured form the green line). (C, D) At corresponding stages, in Tg(*wnt1:*eGFP);*fgf8a*$^{x15/x15}$ embryos, boundary cell fluorescence intensity decreases relative to its r1 neighbor as MHB angle relaxes. Scale bar = 100 μm.

With the visualization of individual cells shown in Fig 5.10, we also can deduce that adhesion and epithelial relaxation are decoupled from each other during dorsal isthmic relaxation in *fgf8a* loss of

function, which was suggested by the relative dynamics of these processes in the *fgf8a* MO+ embryo. The time point at which the tracking began in Fig 5.10 was after adhesion was already lost in r1, yet the orientation of the cells at the boundary changed over time from perpendicular to oblique relative to the A/P axis. We interpret these changes in orientation as reflecting another mechanism that contributes to continued change in the morphology of the boundary independent of adhesion loss. One possibility is a myosin mediated epithelial relaxation step similar to the mechanism used to create transient constrictions between hindbrain rhombomeres (260). Another possibility would be the failure of the boundary cells to initiate or maintain basal constriction, although from our data the cells appear to have a basal-restricted morphology in Tg(*wnt1*:eGFP);*fgf8a*$^{x15/x15}$ embryos. A more interesting possibility is that basal constriction that fails to be mechanically stabilized by surrounding tissues leads to a loss of proper boundary morphology. We have observed that the *wnt1* expressing cells in the dorsal posterior mesencephalon of Tg(*wnt1*:eGFP) embryos organize into a simple epithelium (Fig 5.10, blue marker) that is not present in Tg(*wnt1*:eGFP);*fgf8a*$^{x15/x15}$ embryos. Perhaps this special epithelium provides a local mechanical stiffness in the posterior mesencephalon that allows basal constriction (wedging) of boundary cells to result in a movement in the anterior versus the posterior direction. Or, perhaps the basement membrane of that epithelium interacts with the basement membrane of r1 to stabilize the area during cell wedging.

We also tracked similar dynamics in the ventral region of mes/r1 in Tg(*wnt1*:eGFP) and Tg(*wnt1*:eGFP);*fgf8a*$^{x15/x15}$ embryos, shown in Fig 5.11, though signal attenuation at these imaging depths made it difficult to track individual cells. We observed that in Tg(*wnt1*:eGFP) embryos, the *wnt1* lineage initially spread across the boundary was subsequently compressed into a more narrow region as the boundary angle sharpened (black markers). It was not clear if this behavior was a result of cell wedging. In contrast, in Tg(*wnt1*:eGFP);*fgf8a*$^{x15/x15}$ embryos, the *wnt1* lineage initially spanning the boundary failed to compress and organize into a ring of cells, though their orientation did seem to transition from perpendicular to oblique, perhaps as a result of forces resulting from constriction failure in the dorsal neuroepithelium.

From these data, we can clearly see different behaviors of the *wnt1* lineage in the dorsal and ventral compartments of mes/r1 both during normal development and in response to *fgf8a* loss of function that suggest different epithelial organization and mechanical environments in these two compartments.

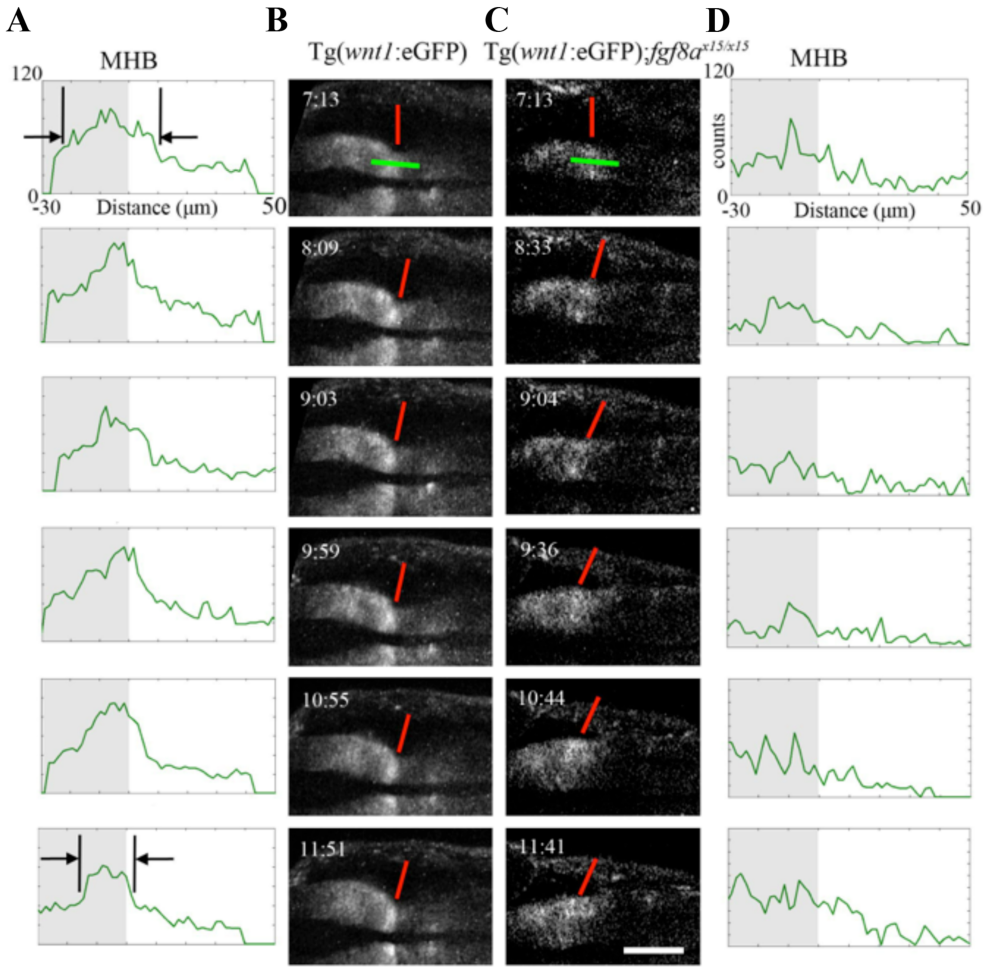

Fig 5.11 Lineage tracing reveals loss of organization of the *wnt1* lineage in the ventral neuroepithelium in Tg(*wnt1*:eGFP);*fgf8a*$^{x15/x15}$ compared to Tg(*wnt1*:eGFP) embryos. (A, B) During mid-somitogenesis to early pharyngula, the *wnt1* lineage in the ventral neuroepithelium of Tg(*wnt1*:eGFP) embryos compresses to a narrow ring of cells anterior to the physical MHB constriction (black markers) while in Tg(*wnt1*:eGFP);*fgf8*$^{x15/x15}$ embryos (C, D), this reorganization fails to occur. Scale bar = 100 μm.

5.3.10 Registration of wnt1 lineage and expression domains in ace phenotype

Tracking the ventral *wnt1* lineage in Tg(*wnt1*:eGFP);*fgf8a*$^{x15/x15}$ embryos was enabled by the perdurance of the GFP protein as *wnt1* expression was already lost in these cells by mid-somitogenesis according to previous reports. Based on the behavior of the dorsal mes/r1 tissue and *wnt1* in response to *fgf8a* loss of function, however, it was not clear to us that the continuous dorsal stripe along the transformed r1 region was due solely to a re-expression of *wnt1* in the roof plate of r1 or that the dorsal component of the ring of cells expressing *wnt1* at the boundary cease to express *wnt1* without *fgf8a*.

From lineage tracing, we characterized *wnt1+* cells in the dorsal boundary that continued to express *wnt1* and were displaced posteriorly by the mechanical instability of the constriction. At the same time, the more posterior neighbors of these cells began increasing *wnt1* expression. These results, in combination with our observation of the depleted morphology of the dorsal region of r1 (Fig 5.5, 5.6), lead us to suspect the dorsal region of the ring of *wnt1+* cells at the boundary contributed to the continuous stripe in the transformed r1 region in addition to the reactivation of *wnt1* in more posterior cells. To differentiate between these interpretations, we therefore integrated our dynamic lineage tracing data with domains of active *wnt1* expression using the method we developed in Section 4.

We previously identified landmarks in mes/r1 that allowed for sufficiently reliable registration of images obtained from embryos live and post in situ hybridization, however, many of these landmarks are missing in *fgf8a* loss of function. We redefined new landmarks shown in Fig 5.12 to allow us to register lineage dynamics and gene expression domains in Tg(*wnt1*:eGFP);*fgf8a*$^{x15/x15}$ embryos.

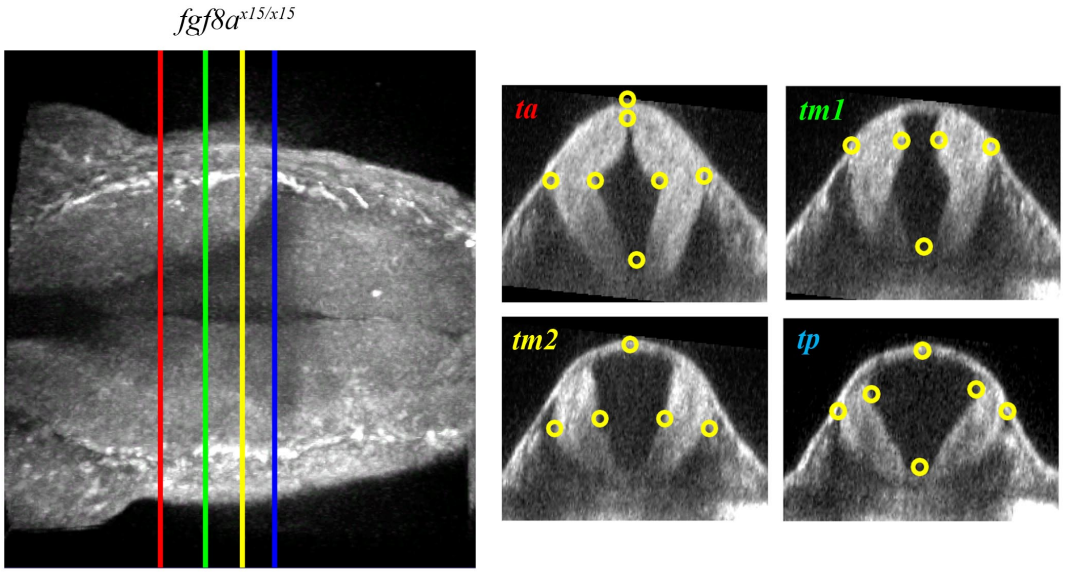

Fig 5.12 Morphological landmarks for registration of *fgf8a*$^{x15/x15}$ embryos. Four reliably identifiable transverse planes along the A/P axis, *ta*, *tm1*, *tm2*, and *tp*, were used to constrain landmarks selected from transverse morphology at each point.

We then imaged Tg(*wnt1*:eGFP) and Tg(*wnt1*:eGFP);*fgf8a*$^{x15/x15}$ embryos live and preformed fluorescence in situ hybridization (FISH) to deposit FITC where *wnt1* transcripts were located and reimaged the same embryos. We processed the images to optimize the orientation of the embryos and registered the FISH images onto the live morphology and GFP distribution using the landmarks shown above with a thin-plate spine elastic registration tool in FIJI. The resulting overlay, shown in Fig 5.13, depicts the current distribution of all cells that have expressed *wnt1:*GFP (lineage) as well as where cells are still currently expressing *wnt1* (gene expression) within the live *ace* mes/r1 morphology.

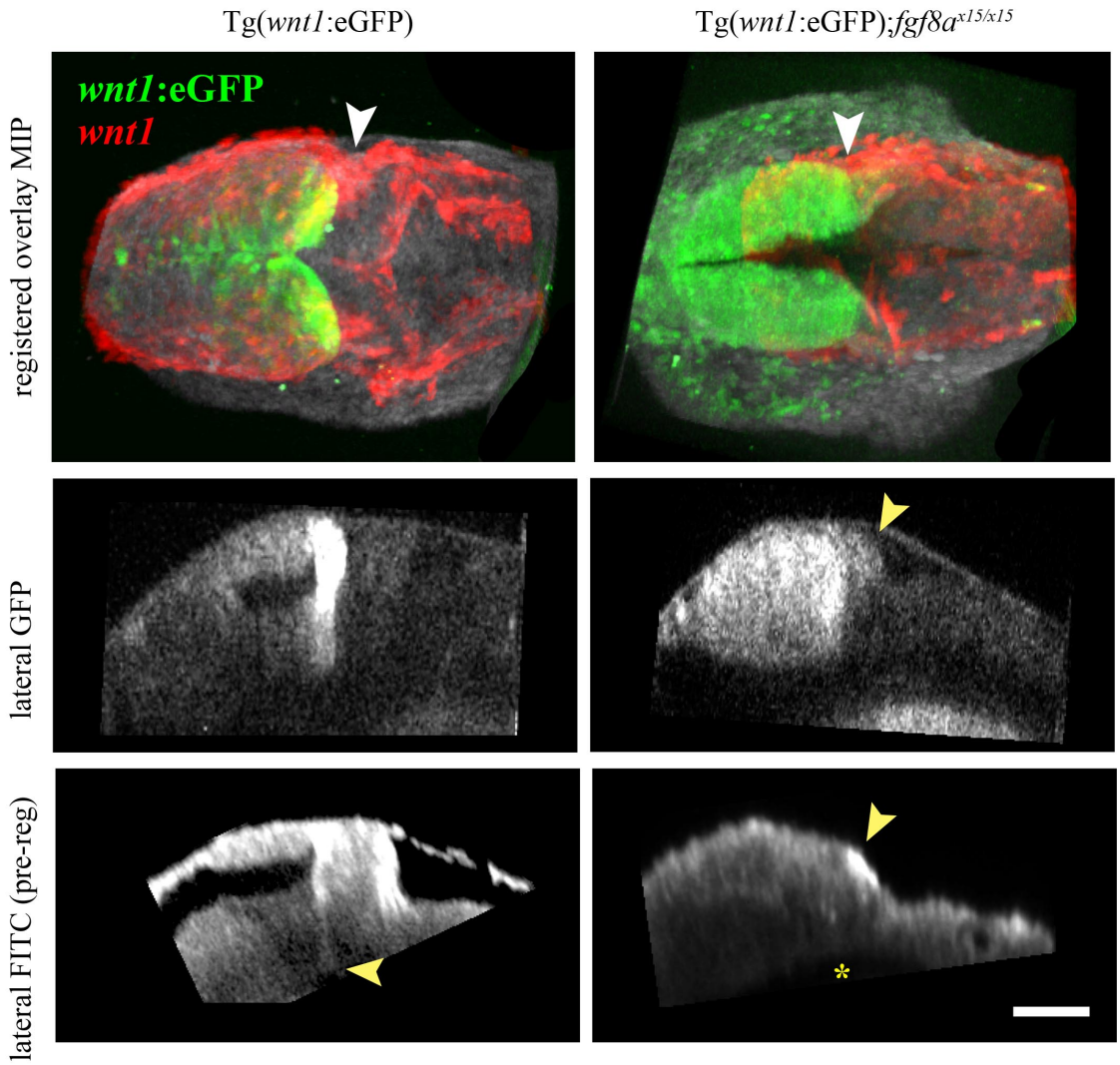

Fig 5.13 Comparison of *wnt1*:eGFP marked lineage compared to regions of active *wnt1* expression in mes/r1 in Tg(*wnt1*:eGFP) and Tg(*wnt1*:eGFP);*fgf8a*$^{x15/x15}$ embryos. Maximum intensity projections of a dorsal view of combined autofluorescence (white), *wnt1*:eGFP (green) and registered FITC (red) signal show overlap between *wnt1* lineage and active *wnt1* expression in the dorsal part of r1 (yellow arrowheads) at the MHB constriction (white arrowhead) in Tg(*wnt1*:eGFP) *fgf8a*$^{x15/x15}$ embryos while the ventral part of the *wnt1* lineage at the boundary no longer expresses *wnt1* (yellow asterisk) compared to Tg(*wnt1*:eGPF) embryos (yellow arrow). Scale bar = 100 µm.

Comparing the distribution of *wnt1*:eGFP in the dorsal and ventral parts of r1 to the location of FITC labeled *wnt1* transcript in Tg(*wnt1*:eGFP);*fgf8a*$^{x15/x15}$ embryos, we found that most of the initially

specified boundary cells appear to have stopped *wnt1* transcription, suggesting that though the relaxing boundary cells have moved slightly posteriorly, the dorsal portion of the ring has not collapsed significantly in the dorsoventral axis to contribute to the tissue that appeared to be presumptive r1. Rather, most of the boundary cells in the dorsal compartment do indeed stop expressing *wnt1* in the absence of *fgf8a*. Further optimization of the registration algorithm for *ace* phenotype may be required to show this more definitely, as registration accuracy was sub-optimal when compared to the performance of the landmarks for the wild-type phenotype. Optimizing the FISH protocol may improve registration accuracy also, as Tg(*wnt1*:eGFP);*fgf8a*$^{x15/x15}$ embryos appeared more distorted at the MHB boundary after FISH.

5.4 Conclusion

Our discovery of this transient constriction in *fgf8a* loss of function shows that using a combination of standard light microscopy techniques and ISH for analysis, even at multiple time points, can lead to the oversight of important morphological dynamics. This oversight is due to two main limitations- lack of 4-D resolution and significant morphological distortions due to tissue fixing and subsequent processing.

By examining morphological dynamics in *fgf8a* loss of function simultaneously with the behavior of the *wnt1* lineage, we have revealed several new important requirements for proper mes/r1 formation including cell adhesion during brain ventricle formation, regulation of epithelial tissue stiffness, and organization of cell morphology and epithelial structure. We have also shown the reliance of proper morphogenesis on the underlying genetic program of the mes/r1 tissue from early somitogenesis.

With these data combining dynamic lineage tracing and gene expression within a live three-dimensional context, we refined the idea that r1 is transformed from cerebellar to tectal fate in *fgf8a* loss of function. We found the transformation is evident, but precedes rather than precludes the formation of the isthmus, and that failure of the initiated morphogenetic program to execute properly contributes to the *ace* phenotype by apparently compromising the structural integrity of the tectum and dorsal boundary.

In the future, it will be of use to examine the potential roles of patterning genes with morphogenetic cell behaviors in mind, as patterning happens within a continuously changing 3-D

environment and it is reasonable to assume genes may have evolved roles to both govern shape changes in tissues and subsequently specify surrounding cell identities.

6. SUMMARY

In this dissertation, I have discussed the complexity of embryonic development in order to motivate the continued development of new imaging modalities that can simultaneously capture molecular and morphological information from live developing embryos. I have shown that Ultrashort Pulse Microscopy is a useful tool for this purpose in developing zebrafish embryos, with the potential for simultaneously imaging up to 5 genetically labeled lineages (marked with different fluorescent protein variants) alongside tissue morphology dynamics *in vivo*. I have also shown that the multiplexed capabilities of UPM enable the integration of data sets from different experiments on the same embryo through image registration. With these tools, I have begun to investigate the roles of *wnt1* and *fgf8a* in the formation of the midbrain-hindbrain boundary in a more complete manner than has been previously conducted and revealed a transient morphogenetic program initiated independently of *fgf8a*. I have also characterized differences in the behavior of the *wnt1* lineage in mes/r1 during both normal and aberrant development depending on their dorsoventral position.

I have taken steps towards demonstrating the potential of UPM for integrating the analysis of embryonic development at the tissue, cellular, and molecular scales. This demonstration includes:

- Robust label-free visualization of embryonic tissues by 2-photon excited autofluorescence with no damage to the embryo.
- Time-lapse experiments to characterize tissue dynamics.
- Time-lapse experiments to characterize a single genetically labeled cell lineage within its morphological context.
- Injection experiments and preliminary spectral unmixing showing the potential for imaging several genetically labeled cell lineages in time-lapse experiments simultaneously.
- OCM and 2PF imaging to visualize domains of gene expression labeled with NBT/BCIP or FITC, respectively, within tissue morphology.

- Registration of gene expression domains onto live embryo morphology and genetic reporter lineage distribution.

With even just these preliminary steps, we have gained new and important insight into the genetic control of morphogenesis in the mes/r1 region in zebrafish including:

- Dorsal and ventral compartments of the mes/r1 region may have different strategies for refining the boundary and perhaps different lineage restriction properties.
- There is a transient constriction that relaxes concomitant with changes in genetic program in *fgf8a* loss of function.
- The *fgf8a* loss of function phenotype includes dysregulation of cell adhesion.
- The *fgf8a* loss of function phenotype may also include aberrant cell migrations from r1.
- In *fgf8a* loss of function, there are two different responses of the *wnt1* lineage depending on their location that correlate with the failure of the MHB constriction to continue forming.

I conclude, based on these works, that UPM will continue to be a useful tool for studying developmental processes in the future.

Based on the experience described in this dissertation, I make the following recommendations. In terms of the imaging instrumentation, I suggest:

- Implementing spectral SPIM using 10 fs pulses to increase imaging speed, in accordance with the recommendation of Dr. Alvin Yeh.
- Adding different scan options to the acquisition software for scanning 256 x 256 and 512 x 512 pixels per image.
- Automate time-lapse acquisition with a tool that relocates the embryos position at each new time point (because it will have certainly moved a bit).
- Improve the axial resolution of the OCT/M system by matching dispersion in both arms, in accordance with the recommendation of Dr. Alvin Yeh.

In terms of the imaging application for studying embryonic development, I suggest:

- Characterizing the possibility of femtosecond microsurgery and/or photoactivation of heat-shock inducible genes.

In terms of image processing, I suggest:

- Automation of rigid registration of embryos to optimal orientation.
- Automation of image segmentation to isolate the neuroepithelium from 3-D image stacks.
- Automation of landmark detection for image registration.
- Improvement on registration accuracy for both wild type and mutant embryos.
- Investigation of algorithms to use the neuroepithelial autofluorescence for cell tracking.
- Initial building of a dynamic "average embryo" to begin creating a virtual atlas of gene expression and morphogenesis during mes/r1 formation.

In terms of genetic tools, I suggest:

- Using nuclear localized fluorescent protein reporters for lineage tracing.
- Characterizing the turnover rate of fluorescent protein reporters localized to different structures (free floating, versus nuclear or membrane localized).
- Consideration of the use of reporter proteins that have faster maturation rates (ex. TurboGreen).
- Consideration of the use of reporter proteins that have faster turnover rates.
- Optimizing fluorescent protein reporter selection to match the two-photon power spectrum of our 10 fs pulses.
- Comparing reporter constructs in stable transgenic lines to endogenous gene expression with 3-D resolution, so any subtle differences in expression will be characterized before experiments are performed.
- Development of a method for labeling and imaging mRNA transcripts live.

I also recommend following up on the possibility suggested by this work that Wnt and/or Fgf participate in morphogenesis during mes/r1 formation, especially to re-examine the literature concerning the evolutionary conservation of the MHB organizer.

Finally, I recommend the further collaboration of developmental biologists and those developing the frontier of biomedical optics instrumentation so that endless signals most beautiful can be used to understand the beginnings of endless forms most beautiful (268).

REFERENCES

1. Megason SG & Fraser SE (2007) Imaging in systems biology. *Cell* 130(5):784-795.
2. Echevarria D, Vieira C, Gimeno L, & Martinez S (2003) Neuroepithelial secondary organizers and cell fate specification in the developing brain. *Brain Research Reviews* 43(2):179-191.
3. Alvarado-Mallart RM (2005) The chick/quail transplantation model: discovery of the isthmic organizer center. *Brain Research Reviews* 49(2):109-113.
4. Raible F & Brand M (2004) Divide et impera - the midbrain-hindbrain boundary and its organizer. *Trends in Neurosciences* 27(12):727-734.
5. Kurokawa D, Ohmura T, Akasaka K, & Aizawa S (2012) A lineage specific enhancer drives otx2 expression in teleost organizer tissues. *Mechanisms of Development* 128(11/12):653-661.
6. Rhinn M, Lun K, Amores A, Yan YL, Postlethwait JH, *et al*. (2003) Cloning, expression and relationship of zebrafish gbx1 and gbx2 genes to Fgf signaling. *Mechanisms of Development* 120(8):919-936.
7. Rhinn M, Lun K, Ahrendt R, Geffarth M, & Brand M (2009) Zebrafish gbx1 refines the midbrain-hindbrain boundary border and mediates the Wnt8 posteriorization signal. *Neural Development* 4:12.
8. Burroughs-Garcia J, Sittaramane V, Chandrasekhar A, & Waters ST (2011) Evolutionarily conserved function of Gbx2 in anterior hindbrain development. *Developmental Dynamics* 240(4):828-838.
9. Hidalgo-Sanchez M, Millet S, Bloch-Gallego E, & Alvarado-Mallart RM (2005) Specification of the meso-isthmo-cerebellar region: the Otx2/Gbx2 boundary. *Brain Research Reviews* 49(2):134-149.
10. Tossell K, Kiecker C, Wizenmann A, Lang E, & Irving C (2011) Notch signalling stabilises boundary formation at the midbrain-hindbrain organiser. *Development* 138(17):3745-3757.

11. Heimbucher T, Murko C, Bajoghli B, Aghaallaei N, Huber A, *et al*. (2007) Gbx2 and Otx2 interact with the WD40 domain of Groucho/Tle corepressors. *Molecular and Cellular Biology* 27(1):340-351.

12. Inoue F, Kurokawa D, Takahashi M, & Aizawa S (2012) Gbx2 directly restricts Otx2 expression to forebrain and midbrain, competing with class III POU factors. *Molecular and Cellular Biology* 32(13):2618-2627.

13. Chung S, Leung A, Han BS, Chang MY, Moon JI, *et al*. (2009) Wnt1-Imx1a forms a novel autoregulatory loop and controls midbrain dopaminergic differentiation synergistically with the Shh-FoxA2 pathway. *Cell Stem Cell* 5(6):646-658.

14. Islam ME, Kikuta H, Inoue F, Kanai M, Kawakami A, *et al*. (2006) Three enhancer regions regulate gbx2 gene expression in the isthmic region during zebrafish development. *Mechanisms of Development* 123(12):907-924.

15. Garda AL, Echevarria D, & Martinez S (2001) Neuroepithelial co-expression of Gbx2 and Otx2 precedes Fgf8 expression in the isthmic organizer. *Mechanisms of Development* 101(1/2):111-118.

16. Li JYH & Joyner AL (2001) Otx2 and Gbx2 are required for refinement and not induction of mid-hindbrain gene expression. *Development* 128(24):4979-4991.

17. Su CY, Kemp HA, & Moens CB (2014) Cerebellar development in the absence of Gbx function in zebrafish. *Developmental Biology* 386(1):181-190.

18. McMahon AP & Bradley A (1990) The Wnt-1 (int-1) proto-oncogene is required for development of a large region of the mouse brain. *Cell* 62:1073-1085.

19. Chi CL, Martinez S, Wurst W, & Martin GR (2003) The isthmic organizer signal Fgf8 is required for cell survival in the prospective midbrain and cerebellum. *Development* 130(12):2633-2644.

20. Lekven AC, Buckles GR, Kostakis N, & Moon RT (2003) wnt1 and wnt10b function redundantly at the zebrafish midbrain-hindbrain boundary. *Developmental Biology* 254(2):172-187.

21. Buckles GR, Thorpe CJ, Ramel MC, & Lekven AC (2004) Combinatorial Wnt control of zebrafish midbrain-hindbrain boundary formation. *Mechanisms of Development* 121(5):437-447.

22. Brand M, Heisenberg CP, Jiang YJ, Beuchle D, Lun K, *et al*. (1996) Mutations in zebrafish genes affecting the formation of the boundary between midbrain and hindbrain. *Development* 123:179-190.

23. Martinez S, Crossley PH, Cobos I, Rubenstein JLR, & Martin GR (1999) Fgf8 induces formation of an ectopic isthmic organizer and isthmocerebellar development via a repressive effect on Otx2 expression. *Development* 126(6):1189-1200.

24. Foucher I, Mione M, Simeone A, Acampora D, Bally-Cuif L, *et al*. (2006) Differentiation of cerebellar cell identities in absence of Fgf signalling in zebrafish Otx morphants. *Development* 133(10):1891-1900.

25. Panhuysen M, Weisenhorn DMV, Blanquet V, Brodski C, Heinzmann U, *et al*. (2004) Effects of Wnt1 signaling on proliferation in the developing mid-hindbrain region. *Molecular and Cellular Neuroscience* 26(1):101-111.

26. Ciani L & Salinas PC (2005) Wnts in the vertebrate nervous system: from patterning to neuronal connectivity. *Nature Reviews Neuroscience* 6(5):351-362.

27. Canning CA, Lee L, Irving C, Mason I, & Jones CM (2007) Sustained interactive Wnt and Fgf signaling is required to maintain isthmic identity. *Developmental Biology* 305(1):276-286.

28. Adams KA, Maida JM, Golden JA, & Riddle RD (2000) The transcription factor Lmx1b maintains Wnt1 expression within the isthmic organizer. *Development* 127(9):1857-1867.

29. O'Hara FP, Beck E, Barr LK, Wong LL, Kessler DS, *et al*. (2005) Zebrafish Lmx1b.1 and Lmx1b.2 are required for maintenance of the isthmic organizer. *Development* 132(14):3163-3173.

30. Carletti B & Rossi F (2008) Neurogenesis in the cerebellum. *Neuroscientist* 14(1):91-100.

31. Tallafuss A & Bally-Cuif L (2003) Tracing of her5 progeny in zebrafish transgenics reveals the dynamics of midbrain-hindbrain neurogenesis and maintenance. *Development* 130(18):4307-4323.

32. Chilov D, Sinjushina N, Saarimaki-Vire J, Taketo MM, & Partanen J (2010) Beta-Catenin regulates intercellular signalling networks and cell-type specific transcription in the developing mouse midbrain-rhombomere 1 region. *PLoS One* 5(6):e10881.

33. Holzschuh J, Hauptmann G, & Driever W (2003) Genetic analysis of the roles of Hh, Fgf8, and Nodal signaling during catecholaminergic system development in the zebrafish brain. *Journal of Neuroscience* 23(13):5507-5519.

34. Volkmann K, Chen YY, Harris MP, Wullimann MF, & Koster RW (2010) The zebrafish cerebellar upper rhombic lip generates tegmental hindbrain nuclei by long-distance migration in an evolutionary conserved manner. *Journal of Comparative Neurology* 518(14):2794-2817.

35. Huang TW, Liu YG, Huang MG, Zhao XL, & Cheng LP (2010) Wnt1-cre-mediated conditional loss of Dicer results in malformation of the midbrain and cerebellum and failure of neural crest and dopaminergic differentiation in mice. *Journal of Molecular Cell Biology* 2(3):152-163.

36. Leucht C, Stigloher C, Wizenmann A, Klafke R, Folchert A, *et al*. (2008) MicroRNA-9 directs late organizer activity of the midbrain-hindbrain boundary. *Nature Neuroscience* 11(6):641-648.

37. Copp AJ (2005) Neurulation in the cranial region - normal and abnormal. *Journal of Anatomy* 207(5):623-635.

38. Gato A & Desmond ME (2009) Why the embryo still matters: CSF and the neuroepithelium as interdependent regulators of embryonic brain growth, morphogenesis and histiogenesis. *Developmental Biology* 327(2):263-272.

39. Parada C, Martin C, Alonso MI, Moro JA, Bueno D, *et al*. (2005) Embryonic cerebrospinal fluid collaborates with the isthmic organizer to regulate mesencephalic gene expression. *Journal of Neuroscience Research* 82(3):333-345.

40. Mathis L, Sieur J, Voiculescu O, Charnay P, & Nicolas JF (1999) Successive patterns of clonal cell dispersion in relation to neuromeric subdivision in the mouse neuroepithelium. *Development* 126(18):4095-4106.

41. Jungbluth S, Larsen C, Wizenmann A, & Lumsden A (2001) Cell mixing between the embryonic midbrain and hindbrain. *Current Biology* 11(3):204-207.

42. Tossell K, Andreae LC, Cudmore C, Lang E, Muthukrishnan U, *et al*. (2011) Lrrn1 is required for formation of the midbrain-hindbrain boundary and organiser through regulation of affinity differences between midbrain and hindbrain cells in chick. *Developmental Biology* 352(2):341-352.

43. Sunmonu NA, Li KR, Guo QX, & Li JYH (2011) Gbx2 and Fgf8 are sequentially required for formation of the midbrain-hindbrain compartment boundary. *Development* 138(4):725-734.

44. Langenberg T & Brand M (2005) Lineage restriction maintains a stable organizer cell population at the zebrafish midbrain-hindbrain boundary. *Development* 132(14):3209-3216.

45. Kasza KE & Zallen JA (2011) Dynamics and regulation of contractile actin-myosin networks in morphogenesis. *Current Opinion in Cell Biology* 23(1):30-38.

46. Lowery LA & Sive H (2005) The genetic mechanisms underlying brain ventricle morphogenesis in zebrafish. *Developmental Biology* 283(2):589-589.

47. Filas BA, Oltean A, Majidi S, Bayly PV, Beebe DC, *et al*. (2012) Regional differences in actomyosin contraction shape the primary vesicles in the embryonic chicken brain. *Physical Biology* 9(6):066007.

48. Filas BA, Oltean A, Beebe DC, Okamoto RJ, Bayly PV, *et al*. (2012) A potential role for differential contractility in early brain development and evolution. *Biomechanics and Modeling in Mechanobiology* 11(8):1251-1262.

49. Rapacioli M, Botelho J, Cerda G, Duarte S, Elliot M, *et al*. (2012) Sonic hedgehog (Shh)/Gli modulates the spatial organization of neuroepithelial cell proliferation in the developing chick optic tectum. *BMC Neuroscience* 13:117.

50. Harding MJ & Nechiporuk AV (2012) Fgfr-Ras-MAPK signaling is required for apical constriction via apical positioning of Rho-associated kinase during mechanosensory organ formation. *Development* 139(17):3130-3135.

51. Sai X & Ladher RK (2008) FGF signaling regulates cytoskeletal remodeling during epithelial morphogenesis. *Current Biology* 18(13):976-981.

52. Lapebie P, Borchiellini C, & Houliston E (2011) Dissecting the PCP pathway: one or more pathways?: Does a separate Wnt-Fz-Rho pathway drive morphogenesis? *Bioessays* 33(10):759-768.

53. Clark CEJ, Nourse CC, & Cooper HM (2012) The tangled web of non-canonical Wnt signalling in neural migration. *Neurosignals* 20(3):202-220.

54. Minsky M (1988) Memior on inventing the confocal scanning microscope. *Scanning* 10(4):128-138.

55. Carlsson K, Danielsson PE, Lenz R, Liljeborg A, Majlof L, *et al*. (1985) 3-dimensional microscopy using a confocal laser scanning microscope. *Optics Letters* 10(2):53-55.

56. Amos WB & White JG (2003) How the confocal laser scanning microscope entered biological research. *Biology of the Cell* 95(6):335-342.

57. White JG, Amos WB, & Fordham M (1987) An evaluation of confocal versus conventional imaging of biological structures by fluorescence light microscopy. *Journal of Cell Biology* 105(1):41-48.

58. Paddock SW (1994) To boldly glow ... applications of laser-scanning confocal microscopy in developmental biology. *Bioessays* 16(5):357-365.

59. Petran M, Hadravsk.M, Egger MD, & Galambos R (1968) Tandem-scanning reflected-light microscope. *Journal of the Optical Society of America* 58(5):661-664.

60. Bertrand JY, Chi NC, Santoso B, Teng ST, Stainier DYR, *et al*. (2010) Haematopoietic stem cells derive directly from aortic endothelium during development. *Nature* 464(7285):108-111.

61. Lam EYN, Hall CJ, Crosier PS, Crosier KE, & Flores MV (2010) Live imaging of Runx1 expression in the dorsal aorta tracks the emergence of blood progenitors from endothelial cells. *Blood* 116(6):909-914.

62. Kirby BB, Takada N, Latimer AJ, Shin J, Carney TJ, *et al*. (2006) In vivo time-lapse imaging shows dynamic oligodendrocyte progenitor behavior during zebrafish development. *Nature Neuroscience* 9(12):1506-1511.

63. Sonnefraud Y, Koh AL, McComb DW, & Maier SA (2012) Nanoplasmonics: engineering and observation of localized plasmon modes. *Laser & Photonics Reviews* 6(3):277-295.

64. Goishi K, Shimizu A, Najarro G, Watanabe S, Rogers R, *et al*. (2006) AlphaA-crystallin expression prevents gamma-crystallin insolubility and cataract formation in the zebrafish cloche mutant lens. *Development* 133(13):2585-2593.

65. Warger WC, Laevsky GS, Townsend DJ, Rajadhyaksha M, & DiMarzio CA (2007) Multimodal optical microscope for detecting viability of mouse embryos in vitro. *Journal of Biomedical Optics* 12(4):044006.

66. Yelin R, Yelin D, Oh WY, Yun SH, Boudoux C, *et al*. (2007) Multimodality optical imaging of embryonic heart microstructure. *Journal of Biomedical Optics* 12(6):064021.

67. Teddy JM, Lansford R, & Kulesa PM (2005) Four-color, 4-D time-lapse confocal imaging of chick embryos. *Biotechniques* 39(5):703-710.

68. Bao ZR, Murray JI, Boyle T, Ooi SL, Sandel MJ, *et al*. (2006) Automated cell lineage tracing in *Caenorhabditis elegans*. *PNAS* 103(8):2707-2712.

69. Fowlkes CC, Luengo Hendriks CL, Keranen SVE, Weber GH, Rubel O, *et al*. (2008) A quantitative spatiotemporal atlas of gene expression in the *Drosophila* blastoderm. *Cell* 133(2):364-374.

70. Huisken J (2012) Slicing embryos gently with laser light sheets. *Bioessays* 34(5):406-411.

71. Keller PJ, Schmidt AD, Santella A, Khairy K, Bao ZR, *et al*. (2010) Fast, high-contrast imaging of animal development with scanned light sheet-based structured-illumination microscopy. *Nature Methods* 7(8):637-642.

72. Santi PA (2011) Light sheet fluorescence microscopy: a review. *Journal of Histochemistry & Cytochemistry* 59(2):129-138.

73. Weber M & Huisken J (2011) Light sheet microscopy for real-time developmental biology. *Current Opinion in Genetics & Development* 21(5):566-572.

74. Keller PJ & Stelzer EHK (2008) Quantitative in vivo imaging of entire embryos with digital scanned laser light sheet fluorescence microscopy. *Current Opinion in Neurobiology* 18(6):624-632.

75. Huisken J, Swoger J, Del Bene F, Wittbrodt J, & Stelzer EHK (2004) Optical sectioning deep inside live embryos by selective plane illumination microscopy. *Science* 305(5686):1007-1009.

76. Keller PJ, Schmidt AD, Wittbrodt J, & Stelzer EHK (2008) Reconstruction of zebrafish early embryonic development by scanned light sheet microscopy. *Science* 322(5904):1065-1069.

77. Arrenberg AB, Stainier DYR, Baier H, & Huisken J (2010) Optogenetic control of cardiac function. *Science* 330(6006):971-974.

78. Engelbrecht CJ, Greger K, Reynaud EG, Krzic U, Colombelli J, *et al*. (2007) Three-dimensional laser microsurgery in light-sheet based microscopy (SPIM). *Optics Express* 15(10):6420-6430.

79. Wu YC, Ghitani A, Christensen R, Santella A, Du Z, *et al*. (2011) Inverted selective plane illumination microscopy (iSPIM) enables coupled cell identity lineaging and neurodevelopmental imaging in *Caenorhabditis elegans*. *PNAS* 108(43):17708-17713.

80. Truong TV, Supatto W, Koos DS, Choi JM, & Fraser SE (2011) Deep and fast live imaging with two-photon scanned light-sheet microscopy. *Nature Methods* 8(9):757-760.

81. Huang D, Swanson EA, Lin CP, Schuman JS, Stinson WG, *et al*. (1991) Optical coherence tomography. *Science* 254(5035):1178-1181.

82. Larina IV, Larin KV, Justice MJ, & Dickinson ME (2011) Optical coherence tomography for live imaging of mammalian development. *Current Opinion in Genetics & Development* 21(5):579-584.

83. Izatt JA, Kulkarni MD, Wang HW, Kobayashi K, & Sivak MV (1996) Optical coherence tomography and microscopy in gastrointestinal tissues. *IEEE Journal of Selected Topics in Quantum Electronics* 2(4):1017-1028.

84. Boppart SA, Brezinski ME, Bouma BE, Tearney GJ, & Fujimoto JG (1996) Investigation of developing embryonic morphology using optical coherence tomography. *Developmental Biology* 177(1):54-63.

85. Liebling M, Forouhar AS, Gharib M, Fraser SE, & Dickinson ME (2005) Four-dimensional cardiac imaging in living embryos via postacquisition synchronization of nongated slice sequences. *Journal of Biomedical Optics* 10(5):054001.

86. Luo W, Marks DL, Ralston TS, & Boppart SA (2006) Three-dimensional optical coherence tomography of the embryonic murine cardiovascular system. *Journal of Biomedical Optics* 11(2):021014.

87. Blanchard GB & Adams RJ (2011) Measuring the multi-scale integration of mechanical forces during morphogenesis. *Current Opinion in Genetics & Development* 21(5):653-663.

88. Varner VD, Voronov DA, & Taber LA (2010) Mechanics of head fold formation: investigating tissue-level forces during early development. *Development* 137(22):3801-3811.

89. Cadotte DW, Mariampillai A, Cadotte A, Lee KKC, Kiehl TR, *et al*. (2012) Speckle variance optical coherence tomography of the rodent spinal cord: in vivo feasibility. *Biomedical Optics Express* 3(5):911-919.

90. Sudheendran N, Syed SH, Dickinson ME, Larina IV, & Larin KV (2011) Speckle variance OCT imaging of the vasculature in live mammalian embryos. *Laser Physics Letters* 8(3):247-252.

91. Supatto W, Truong TV, Debarre D, & Beaurepaire E (2011) Advances in multiphoton microscopy for imaging embryos. *Current Opinion in Genetics & Development* 21(5):538-548.

92. Masters BR & So PTC (2004) Antecedents of two-photon excitation laser scanning microscopy. *Microscopy Research and Technique* 63(1):3-11.

93. Kaiser W & Garrett CGB (1961) 2-photon excitation in CaF_2:EU^{2+}. *Physical Review Letters* 7(6):229-231.

94. Denk W, Strickler JH, & Webb WW (1990) 2-photon laser scanning fluorescence microscopy. *Science* 248(4951):73-76.

95. Potter SM, Zheng C, Koos DS, Feinstein P, Fraser SE, *et al*. (2001) Structure and emergence of specific olfactory glomeruli in the mouse. *Journal of Neuroscience* 21(24):9713-9723.

96. Inada H, Watanabe M, Uchida T, Ishibashi H, Wake H, *et al*. (2011) GABA regulates the multidirectional tangential migration of GABAergic interneurons in living neonatal mice. *PLoS One* 6(12):e27048.

97. Rodriguez-Contreras A, van Hoeve JSS, Habets RLP, Locher H, & Borst JGG (2008) Dynamic development of the calyx of Held synapse. *PNAS* 105(14):5603-5608.

98. Brendza RP, O'Brien C, Simmons K, McKeel DW, Bales KR, *et al*. (2003) PDAPP;YFP double transgenic mice: a tool to study antyloid-beta associated changes in axonal, dendritic, and synaptic structures. *Journal of Comparative Neurology* 456(4):375-383.

99. Pan F, Aldridge GM, Greenough WT, & Gan WB (2010) Dendritic spine instability and insensitivity to modulation by sensory experience in a mouse model of fragile X syndrome. *PNAS* 107(41):17768-17773.

100. Cruz-Martin A, Crespo M, & Portera-Cailliau C (2010) Delayed stabilization of dendritic spines in fragile X mice. *Journal of Neuroscience* 30(23):7793-7803.

101. Squirrell JM, Wokosin DL, White JG, & Bavister BD (1999) Long-term two-photon fluorescence imaging of mammalian embryos without compromising viability. *Nature Biotechnology* 17(8):763-767.

102. Halacheva V, Fuchs M, Donitz J, Reupke T, Puschel B, *et al*. (2011) Planar cell movements and oriented cell division during early primitive streak formation in the mammalian embryo. *Developmental Dynamics* 240(8):1905-1916.

103. McMahon A, Supatto W, Fraser SE, & Stathopoulos A (2008) Dynamic analyses of *Drosophila* gastrulation provide insights into collective cell migration. *Science* 322:1546-1550.

104. Brodland GW, Conte V, Cranston PG, Veldhuis J, Narasimhan S, *et al*. (2010) Video force microscopy reveals the mechanics of ventral furrow invagination in *Drosophila*. *PNAS* 107(51):22111-22116.

105. Hagerling R, Pollmann C, Kremer L, Andresen V, & Kiefer F (2011) Intravital two-photon microscopy of lymphatic vessel development and function using a transgenic Prox1 promoter-directed mOrange2 reporter mouse. *Biochemical Society Transactions* 39(6):1674-1681.

106. McDole K, Xiong Y, Iglesias PA, & Zheng YX (2011) Lineage mapping the pre-implantation mouse embryo by two-photon microscopy, new insights into the segregation of cell fates. *Developmental Biology* 355(2):239-249.

107. Dickinson ME, Bearman G, Tille S, Lansford R, & Fraser SE (2001) Multi-spectral imaging and linear unmixing add a whole new dimension to laser scanning fluorescence microscopy. *Biotechniques* 31(6):1272, 1274-6, 1278.

108. Bower DV, Sato Y, & Lansford R (2011) Dynamic lineage analysis of embryonic morphogenesis using transgenic quail and 4D multispectral imaging. *Genesis* 49(7):619-643.

109. Sheetz KE, Hoover EE, Carriles R, Kleinfeld D, & Squier JA (2008) Advancing multifocal nonlinear microscopy: development and application of a novel multibeam Yb:KGd(WO_4)$_2$ oscillator. *Optics Express* 16(22):17574-17584.

110. Ragan T, Sylvan JD, Kim KH, Huang H, Bahlmann K, *et al*. (2007) High-resolution whole organ imaging using two-photon tissue cytometry. *Journal of Biomedical Optics* 12(1):014015.

111. Aviles-Espinosa R, Andilla J, Porcar-Guezenec R, Levecq X, Artigas D, *et al*. (2011) Open-loop wavefront sensing scheme for specimen aberrations correction in two-photon excited fluorescence microscopy. *Advanced Microscopy Techniques II,* Proceedings of SPIE, eds So PTC & Beaurepaire E, Vol 8086.

112. Cottet D, Douady J, Vial JC, & Wege HA (2011) Development of a non-linear optical microscope for real-time measurement of neuronal activity in sub-micrometric structures. *Optical Materials* 33(9):1434-1439.

113. Mahou P, Zimmerley M, Loulier K, Matho KS, Labroille G, *et al*. (2012) Multicolor two-photon tissue imaging by wavelength mixing. *Nature Methods* 9(8):815-818.

114. Debarre D, Pena AM, Supatto W, Boulesteix T, Strupler M, *et al*. (2006) Second- and third-harmonic generation microscopies for the structural imaging of intact tissues. *Medecine Sciences* 22(10):845-850.

115. Reeve JE, Anderson HL, & Clays K (2010) Dyes for biological second harmonic generation imaging. *Physical Chemistry Chemical Physics* 12(41):13484-13498.

116. Franken PA, Weinreich G, Peters CW, & Hill AE (1961) Generation of optical harmonics. *Physical Review Letters* 7(4):118-119.

117. Hellwart R & Christen P (1974) Nonlinear optical microscope examination of structure in polycrystalline ZnSe. *Optics Communications* 12(3):318-322.

118. Aviles-Espinosa R, Santos S, Brodschelm A, Kaenders WG, Alonso-Ortega C, *et al*. (2010) Third-harmonic generation for the study of *Caenorhabditis elegans* embryogenesis. *Journal of Biomedical Optics* 15(4):046020.

119. Hsieh CS, Chen SU, Lee YW, Yang YS, & Sun CK (2008) Higher harmonic generation microscopy of in vitro cultured mammal oocytes and embryos. *Optics Express* 16(15):11574-11588.

120. Olivier N, Luengo-Oroz MA, Duloquin L, Faure E, Savy T, *et al*. (2010) Cell lineage reconstruction of early zebrafish embryos using label-free nonlinear microscopy. *Science* 329(967):967-971.

121. Djaker N, Marguet D, & Rigneault H (2006) Stimulated Raman microscopy (CARS): from principles to applications. *Medecine Sciences* 22(10):853-858.

122. Pezacki JP, Blake JA, Danielson DC, Kennedy DC, Lyn RK, *et al*. (2011) Chemical contrast for imaging living systems: molecular vibrations drive CARS microscopy. *Nature Chemical Biology* 7(3):137-145.

123. Hartschuh A, Sanchez EJ, Xie XS, & Novotny L (2003) High-resolution near-field Raman microscopy of single-walled carbon nanotubes. *Physical Review Letters* 90(9):095503.

124. Freudiger CW, Min W, Saar BG, Lu S, Holtom GR, *et al*. (2008) Label-free biomedical imaging with high sensitivity by stimulated Raman scattering microscopy. *Science* 322(5909):1857-1861.

125. Chien CH, Chen WW, Wu JT, & Chang TC (2011) Label-free imaging of *Drosophila* in vivo by coherent anti-Stokes Raman scattering and two-photon excitation autofluorescence microscopy. *Journal of Biomedical Optics* 16(1):016012.

126. Folick A, Min W, & Wang MC (2011) Label-free imaging of lipid dynamics using coherent anti-Stokes Raman scattering (CARS) and stimulated Raman scattering (SRS) microscopy. *Current Opinion in Genetics & Development* 21(5):585-590.

127. Freudiger CW, Min W, Holtom GR, Xu BW, Dantus M, *et al*. (2011) Highly specific label-free molecular imaging with spectrally tailored excitation-stimulated Raman scattering (STE-SRS) microscopy. *Nature Photonics* 5(2):103-109.

128. Bardeen CJ, Yakovlev VV, Squier JA, Wilson KR, Carpenter SD, *et al*. (1999) Effect of pulse shape on the efficiency of multiphoton processes: implications for biological microscopy. *Journal of Biomedical Optics* 4(3):362-367.

129. Yeh AT, Gibbs H, Hu JJ, & Larson AM (2008) Advances in nonlinear optical microscopy for visualizing dynamic tissue properties in culture. *Tissue Engineering Part B: Reviews* 14(1):119-131.

130. Meshulach D & Silberberg Y (1998) Coherent quantum control of two-photon transitions by a femtosecond laser pulse. *Nature* 396(6708):239-242.

131. Albota MA, Xu C, & Webb WW (1998) Two-photon fluorescence excitation cross sections of biomolecular probes from 690 to 960 nm. *Applied Optics* 37(31):7352-7356.

132. Ogilvie JP, Kubarych KJ, Alexandrou A, & Joffre M (2005) Fourier transform measurement of two-photon excitation spectra: applications to microscopy and optimal control. *Optics Letters* 30(8):911-913.

133. Walowicz KA, Pastirk I, Lozovoy VV, & Dantus M (2002) Multiphoton intrapulse interference: control of multiphoton processes in condensed phases. *Journal of Physical Chemistry A* 106(41):9369-9373.

134. Hashimoto H, Isobe K, Suda A, Kannari F, Kawano H, *et al*. (2010) Measurement of two-photon excitation spectra of fluorescent proteins with nonlinear Fourier-transform spectroscopy. *Applied Optics* 49(17):3323-3329.

135. Pang S, Yeh AT, Wang C, & Meissner KE (2009) Beyond the 1/T-p limit: two-photon-excited fluorescence using pulses as short as sub-10-fs. *Journal of Biomedical Optics* 14(5):054041.

136. Wang C & Yeh AT (2012) Two-photon excited fluorescence enhancement with broadband versus tunable femtosecond laser pulse excitation. *Journal of Biomedical Optics* 17(2):025003.

137. Drexler W, Morgner U, Kartner FX, Pitris C, Boppart SA, *et al*. (1999) In vivo ultrahigh-resolution optical coherence tomography. *Optics Letters* 24(17):1221-1223.

138. Schmitt JM (1999) Optical coherence tomography (OCT): a review. *IEEE Journal of Selected Topics in Quantum Electronics* 5(4):1205-1215.

139. Wu QF, Applegate BE, & Yeh AT (2011) Cornea microstructure and mechanical responses measured with nonlinear optical and optical coherence microscopy using sub-10-fs pulses. *Biomedical Optics Express* 2(5):1135-1146.

140. Larson AM & Yeh AT (2006) Ex vivo characterization of sub-10-fs pulses. *Optics Letters* 31(11):1681-1683.

141. Larson AM, Lee A, Lee P, Bayless KJ, & Yeh AT (2009) Ultrashort pulse multispectral non-linear optical microscopy. *Journal of Innovative Optical Health Sciences* 2(1):27-35.

142. Spemann H & Mangold H (1924) The induction of embryonic predispositions by implantation of organizers foreign to the species. *Archiv Fur Mikroskopische Anatomie Und Entwicklungsmechanik* 100(3/4):599-638.

143. Mullins MC, Hammerschmidt M, Haffter P, & Nussleinvolhard C (1994) Large-scale mutagenesis in the zebrafish: in search ofgenes controlling development in a vertebrate. *Current Biology* 4(3):189-202.

144. Solnicakrezel L, Schier AF, & Driever W (1994) Efficient recovery of enu-induced mutations from the zebrafish germline. *Genetics* 136(4):1401-1420.

145. Garciafernandez J & Holland PWH (1994) Archetypal organization of the amphioxus hox gene-cluster. *Nature* 370(6490):563-566.

146. Soshnikova N, Dewaele R, Janvier P, Krumlauf R, & Duboule D (2013) Duplications of hox gene clusters and the emergence of vertebrates. *Developmental Biology* 378(2):194-199.

147. Shimomura O, Johnson FH, & Saiga Y (1962) Extraction, purification, and properties of Aequorin, a bioluminescent protein from luminous hydromedusan, *Aequorea*. *Journal of Cellular and Comparative Physiology* 59(3):223-239.

148. Heim R, Cubitt AB, & Tsien RY (1995) Improved green fluorescence. *Nature* 373(6516):663-664.

149. Chalfie M, Tu Y, Euskirchen G, Ward WW, & Prasher DC (1994) Green fluorescent protein as a marker for gene-expression. *Science* 263(5148):802-805.

150. Ciruna B, Jenny A, Lee D, Mlodzik M, & Schier AF (2006) Planar cell polarity signalling couples cell division and morphogenesis during neurulation. *Nature* 439(7073):220-224.

151. Dixon MJ, Marazita ML, Beaty TH, & Murray JC (2011) Cleft lip and palate: understanding genetic and environmental influences. *Nature Reviews Genetics* 12(3):167-178.

152. Marrs JA, Clendenon SG, Ratcliffe DR, Fielding SM, Liu Q*, et al*. (2010) Zebrafish fetal alcohol syndrome model: effects of ethanol are rescued by retinoic acid supplement. *Alcohol* 44(7/8):707-715.

153. Yang N, Zuchero JB, Ahlenius H, Marro S, Ng YH*, et al*. (2013) Generation of oligodendroglial cells by direct lineage conversion. *Nature Biotechnology* 31(5):434-439.

154. Margariti A, Winkler B, Karamariti E, Zampetaki A, Tsai T-n, *et al*. (2012) Direct reprogramming of fibroblasts into endothelial cells capable of angiogenesis and reendothelialization in tissue-engineered vessels. *PNAS* 109(34):13793-13798.

155. Vierbuchen T, Ostermeier A, Pang ZP, Kokubu Y, Suedhof TC, *et al*. (2010) Direct conversion of fibroblasts to functional neurons by defined factors. *Nature* 463(7284):1035-1041.

156. Kimmel CB, Ballard WW, Kimmel SR, Ullmann B, & Schilling TF (1995) Stages of embryonic development of the zebrafish. *Developmental Dynamics* 203(3):253-310.

157. Woo K, Shih J, & Fraser SE (1995) Fate maps of the zebrafish embryo. *Current Opinion in Genetics & Development* 5(4):439-443.

158. Ettensohn CA (2013) Encoding anatomy: developmental gene regulatory networks and morphogenesis. *Genesis* 51(6):383-409.

159. Streit A, Tambalo M, Chen J, Grocott T, Anwar M, *et al*. (2013) Experimental approaches for gene regulatory network construction: the chick as a model system. *Genesis* 51(5):296-310.

160. Squier J & Muller M (2001) High resolution nonlinear microscopy: a review of sources and methods for achieving optimal imaging. *Review of Scientific Instruments* 72(7):2855-2867.

161. Amat F & Keller PJ (2013) Towards comprehensive cell lineage reconstructions in complex organisms using light-sheet microscopy. *Development Growth & Differentiation* 55(4):563-578.

162. Truong TV & Supatto W (2011) Toward high-content/high-throughput imaging and analysis of embryonic morphogenesis. *Genesis* 49(7):555-569.

163. Planchon TA, Gao L, Milkie DE, Davidson MW, Galbraith JA, *et al*. (2011) Rapid three-dimensional isotropic imaging of living cells using Bessel beam plane illumination. *Nature Methods* 8(5):417-423.

164. Bhat S, Larina IV, Larin KV, Dickinson ME, & Liebling M (2013) 4D reconstruction of the beating embryonic heart from two orthogonal sets of parallel optical coherence tomography slice-sequences. *IEEE Transactions on Medical Imaging* 32(3):578-588.

165. Larina IV, Larin KV, Dickinson ME, & Liebling M (2012) Sequential turning acquisition and reconstruction (STAR) method for four-dimensional imaging of cyclically moving structures. *Biomedical Optics Express* 3(3):650-660.

166. Syed SH, Larin KV, Dickinson ME, & Larina IV (2011) Optical coherence tomography for high-resolution imaging of mouse development in utero. *Journal of Biomedical Optics* 16(4):046004.

167. Akam ME (1983) The location of ultrabithorax transcripts in *Drosophila* tissue sections. *EMBO Journal* 2(11):2075-2084.

168. Khairy K & Keller PJ (2011) Reconstructing embryonic development. *Genesis* 49(7):488-513.

169. Westerfield M (2000) *The zebrafish book. A guide for the laboratory use of zebrafish (Danio rerio)*. (University of Oregon Press, Eugene) 4th Ed.

170. Lilie C, Gibbs HC, Beaster-Jones L, Whitener A, Butler A, *et al*. (in revision) Cis-regulatory analysis of zebrafish wnt1/wnt10b reveals multiple activating enhancers and promoter-dependent enhancer suppression.

171. Schindelin J, Arganda-Carreras I, Frise E, Kaynig V, Longair M, *et al*. (2012) Fiji: an open-source platform for biological-image analysis. *Nature Methods* 9(7):676-682.

172. Peng HC, Ruan ZC, Long FH, Simpson JH, & Myers EW (2010) V3D enables real-time 3D visualization and quantitative analysis of large-scale biological image data sets. *Nature Biotechnology* 28(4):348-353.

173. Varner VD & Taber LA (2012) Not just inductive: a crucial mechanical role for the endoderm during heart tube assembly. *Development* 139(9):1680-1690.

174. Lister JA (2002) Development of pigment cells in the zebrafish embryo. *Microscopy Research and Technique* 58(6):435-441.

175. Rhinn M & Brand M (2001) The midbrain-hindbrain boundary organizer. *Current Opinion in Neurobiology* 11(1):34-42.

176. Huang SH, Heikal AA, & Webb WW (2002) Two-photon fluorescence spectroscopy and microscopy of NAD(P)H and flavoprotein. *Biophysical Journal* 82(5):2811-2825.

177. Greenhill ER, Rocco A, Vibert L, Nikaido M, & Kelsh RN (2011) An iterative genetic and dynamical modelling approach identifies novel features of the gene regulatory network underlying melanocyte development. *PLoS Genetics* 7(9):e1002265.

178. Raible DW, Wood A, Hodsdon W, Henion PD, Weston JA, *et al*. (1992) Segregation and early dispersal of neural crest cells in the embryonic zebrafish. *Developmental Dynamics* 195(1):29-42.

179. Taylor KL, Lister JA, Zeng ZQ, Ishizaki H, Anderson C, *et al*. (2011) Differentiated melanocyte cell division occurs in vivo and is promoted by mutations in Mitf. *Development* 138(16):3579-3589.

180. Russek-Blum N, Nabel-Rosen H, & Levkowitz G (2009) High resolution fate map of the zebrafish diencephalon. *Developmental Dynamics* 238(7):1827-1835.

181. Dancik Y, Favre A, Loy CJ, Zvyagin AV, & Roberts MS (2013) Use of multiphoton tomography and fluorescence lifetime imaging to investigate skin pigmentation in vivo. *Journal of Biomedical Optics* 18(2):29802.

182. Antoniou C, Lademann J, Richter H, Astner S, Patzelt A, *et al*. (2009) Analysis of the melanin distribution in different ethnic groups by in vivo laser scanning microscopy. *Laser Physics Letters* 6(5):393-398.

183. Lowery LA & Sive H (2004) Strategies of vertebrate neurulation and a re-evaluation of teleost neural tube formation. *Mechanisms of Development* 121(10):1189-1197.

184. Kaufmann A, Mickoleit M, Weber M, & Huisken J (2012) Multilayer mounting enables long-term imaging of zebrafish development in a light sheet microscope. *Development* 139(17):3242-3247.

185. Saytashev I, Arkhipov SN, Winkler N, Zuraski K, Lozovoy VV, *et al*. (2012) Pulse duration and energy dependence of photodamage and lethality induced by femtosecond near infrared laser pulses in *Drosophila melanogaster*. *Journal of Photochemistry and Photobiology B: Biology* 115:42-50.

186. Drobizhev M, Tillo S, Makarov NS, Hughes TE, & Rebane A (2009) Absolute two-photon absorption spectra and two-photon brightness of orange and red fluorescent proteins. *Journal of Physical Chemistry B* 113(4):855-859.

187. Jekely G & Arendt D (2007) Cellular resolution expression profiling using confocal detection of NBT/BCIP precipitate by reflection microscopy. *Biotechniques* 42(6):751-755.

188. Trinh LA, McCutchen MD, Bonner-Fraser M, Fraser SE, Bumm LA, *et al*. (2007) Fluorescent in situ hybridization employing the conventional NBT/BCIP chromogenic stain. *Biotechniques* 42(6):756-759.

189. Matuschek N, Kartner FX, & Keller U (1998) Theory of double-chirped mirrors. *IEEE Journal of Selected Topics in Quantum Electronics* 4(2):197-208.

190. Xi P, Andegeko Y, Weisel LR, Lozovoy VV, & Dantus M (2008) Greater signal, increased depth, and less photobleaching in two-photon microscopy with 10 fs pulses. *Optics Communications* 281(7):1841-1849.

191. Olivier N, Debarre D, & Beaurepaire E (2009) Dynamic aberration correction for multiharmonic microscopy. *Optics Letters* 34(20):3145-3147.

192. Chauhan VK, Cohen J, Vaughan PM, Bowlan P, & Trebino R (2010) Distortion-free single-prism/grating ultrashort laser pulse compressor. *IEEE Journal of Quantum Electronics* 46(12):1726-1731.

193. Li WH & Zheng G (2012) Photoactivatable fluorophores and techniques for biological imaging applications. *Photochemical & Photobiological Sciences* 11(3):460-471.

194. Dymecki SM, Ray RS, & Kim JC (2010) Mapping cellfate and function using recombinase-based intersectional strategies. *Methods in Enzymology* 477:183-213.

195. Corish P & Tyler-Smith C (1999) Attenuation of green fluorescent protein half-life in mammalian cells. *Protein Engineering* 12(12):1035-1040.

196. Peng H (2008) Bioimage informatics: a new area of engineering biology. *Bioinformatics* 24(17):1827-1836.

197. Tiedemann HB, Schneltzer E, Zeiser S, Hoesel B, Beckers J, *et al*. (2012) From dynamic expression patterns to boundary formation in the presomitic mesoderm. *PLoS Computational Biology* 8(6):e1002586.

198. Li XQ, Zhao XN, Fang Y, Jiang X, Duong T, *et al*. (1998) Generation of destabilized green fluorescent protein transcription reporter. *Journal of Biological Chemistry* 273(52):34970-34975.

199. Leibfarth S, Monnich D, Welz S, Siegel C, Schwenzer N, *et al*. (2013) A strategy for multimodal deformable image registration to integrate PET/MR into radiotherapy treatment planning. *Acta Oncology* 52(7):1353-1359.

200. Tavakoli V & Amini AA (2013) A survey of shaped-based registration and segmentation techniques for cardiac images. *Computer Vision and Image Understanding* 117(9):966-989.

201. Audette MA, Ferrie FP, & Peters TM (2000) An algorithmic overview of surface registration techniques for medical imaging. *Medical Image Analysis* 4(3):201-217.

202. Lippolis G, Edsjo A, Helczynski L, Bjartell A, & Overgaard NC (2013) Automatic registration of multi-modal microscopy images for integrative analysis of prostate tissue sections. *BMC Cancer* 13:408.

203. Michalek J, Capek M, & Kubinova L (2011) Nonrigid registration of CLSM images of physical sections with discontinuous deformations. *Microscopy and Microanalysis* 17(6):923-936.

204. Mosaliganti K, Pan T, Sharp R, Ridgway R, Iyengar S, *et al*. (2006) Registration and 3D visualization of large microscopy images. *Medical Imaging 2006: Image Processing, Pts 1-3,* Proceedings of SPIE, eds Reinhardt JM & Pluim JPW, Vol 6144.

205. Sorzano COS, Thevenaz P, & Unser M (2005) Elastic registration of biological images using vector-spline regularization. *IEEE Transactions on Biomedical Engineering* 52(4):652-663.

206. Holden M (2008) A review of geometric transformations for nonrigid body registration. *IEEE Transactions on Medical Imaging* 27(1):111-128.

207. Guo YJ, Sivaramakrishna R, Lu CC, Suri JS, & Laxminarayan S (2006) Breast image registration techniques: a survey. *Medical and Biological Computing and Engineering* 44(1/2):15-26.

208. Hofstad EF, Sorger H, Leira HO, Amundsen T, & Lango T (2014) Automatic registration of CT images to patient during the initial phase of bronchoscopy: a clinical pilot study. *Medical Physics* 41(4):041903.

209. Gallea R, Ardizzone E, Pirrone R, & Gambino O (2013) Three-dimensional fuzzy kernel regression framework for registration of medical volume data. *Pattern Recognition* 46(11):3000-3016.

210. Bookstein FL (1989) Principal warps: thin-plate splines and the decomposition of deformations. *IEEE Transactions on Pattern Analysis and Machine Intelligence* 11(6):567-585.

211. Ronneberger O, Liu K, Rath M, Ruess D, Mueller T, *et al*. (2012) ViBE-Z: a framework for 3D virtual colocalization analysis in zebrafish larval brains. *Nature Methods* 9(7):735-742.

212. Peng HC, Chung PO, Long FH, Qu L, Jenett A, *et al*. (2011) BrainAligner: 3D registration atlases of *Drosophila* brains. *Nature Methods* 8(6):493-498.

213. Liu X, Wang P, Fu J, Lv D, Chen D, *et al*. (2011) Two-photon fluorescence real-time imaging on the development of early mouse embryo by stages. *Journal of Microscopy* 241(2):212-218.

214. Rowitch DH, Echelard Y, Danielian PS, Gellner K, Brenner S, *et al*. (1998) Identification of an evolutionarily conserved 110 base-pair cis-acting regulatory sequence that governs Wnt-1 expression in the murine neural plate. *Development* 125(14):2735-2746.

215. Inoue D & Wittbrodt J (2011) One for all - a highly efficient and versatile method for fluorescent immunostaining in fish embryos. *PLoS One* 6(5):e19713.

216. Peng HC, Bria A, Zhou Z, Iannello G, & Long FH (2014) Extensible visualization and analysis for multidimensional images using Vaa3D. *Nature Protocols* 9(1):193-208.

217. Lowery LA & Sive H (2005) Initial formation of zebrafish brain ventricles occurs independently of circulation and requires the nagie oko and snakehead/atp1a1a.1 gene products. *Development* 132(9):2057-2067.

218. Medvedev SY, Tokunaga T, Schultz RM, Furukawa T, Nagai T, *et al*. (2002) Quantitative analysis of gene expression in preimplantation mouse embryos using green fluorescent protein reporter. *Biology of Reproduction* 67(1):282-286.

219. Frimpong EA & Henebry ML (2012) Short-term effects of formalin and ethanol fixation and preservation techniques on weight and size of fish eggs. *Transactions of the American Fisheries Society* 141(6):1472-1479.

220. Geldmacher A & Wieland K (1999) Implications of mechanical deformation and formaldehyde preservation for the identification of stage-specific characteristics of Baltic cod eggs. *Journal of Applied Ichthyology* 15(2):75-79.

221. Loqman MY, Bush PG, Farquharson C, & Hall AC (2010) A cell shrinkage artefact in growth plate chondrocytes with common fixative solutions: importance of fixative osmolarity for maintaining morphology. *European Cells & Materials* 19:214-227.

222. Schulz G, Crooijmans HJA, Germann M, Scheffler K, Mueller-Gerbl M, *et al*. (2011) Three-dimensional strain fields in human brain resulting from formalin fixation. *Journal of Neuroscience Methods* 202(1):17-27.

223. Zamir EA, Czirok A, Rongish BJ, & Little CD (2005) A digital image-based method for computational tissue fate mapping during early avian morphogenesis. *Annals of Biomedical Engineering* 33(6):854-865.

224. Bailey TJ, Davis DH, Vance JE, & Hyde DR (2012) Spectral-domain optical coherence tomography as a noninvasive method to assess damaged and regenerating adult zebrafish retinas. *Investigative Ophthalmology and Visual Science* 53(6):3126-3138.

225. Rao KD, Alex A, Verma Y, Thampi S, & Gupta PK (2009) Real-time in vivo imaging of adult zebrafish brain using optical coherence tomography. *Journal of Biophotonics* 2(5):288-291.

226. Rao KD, Upadhyaya P, Sharma M, & Gupta PK (2012) Noninvasive imaging of ethanol-induced developmental defects in zebrafish embryos using optical coherence tomography. *Birth Defects Research Part B: Developmental and Reproductive Toxicology* 95(1):7-11.

227. Kagemann L, Ishikawa H, Zou J, Charukamnoetkanok P, Wollstein G, *et al*. (2008) Repeated, noninvasive, high resolution spectral domain optical coherence tomography imaging of zebrafish embryos. *Molecular Vision* 14:2157-2170.

228. Zhang PF, Mehta K, Rehman S, & Chen NG (2014) Imaging single chiral nanoparticles in turbid media using circular-polarization optical coherence microscopy. *Scientific Reports* 4:4979.

229. Robles FE, Wilson C, Grant G, & Wax A (2011) Molecular imaging true-colour spectroscopic optical coherence tomography. *Nature Photonics* 5(12):744-747.

230. Khan MH, Choi B, Chess S, Kelly KM, McCullough J, *et al*. (2004) Optical clearing of in vivo human skin: implications for light-based diagnostic imaging and therapeutics. *Lasers in Surgery and Medicine* 34(2):83-85.

231. He RY, Wei HJ, Gu HM, Zhu ZG, Zhang YQ, *et al*. (2012) Effects of optical clearing agents on noninvasive blood glucose monitoring with optical coherence tomography: a pilot study. *Journal of Biomedical Optics* 17(10):101513.

232. Cicchi R, Pavone FS, Massi D, & Sampson DD (2005) Contrast and depth enhancement in two-photon microscopy of human skin ex vivo by use of optical clearing agents. *Optics Express* 13(7):2337-2344.

233. Hunsaker MR & Amaral DG (2014) A semi-automated pipeline for the segmentation of rhesus macaque hippocampus: validation across a wide age range. *PLoS One* 9(2):e89456.

234. Orczyk C, Rusinek H, Rosenkrantz AB, Mikheev A, Deng FM, *et al*. (2013) Preliminary experience with a novel method of three-dimensional co-registration of prostate cancer digital histology and in vivo multiparametric MRI. *Clinical Radiology* 68(12):652-658.

235. Li SS, Glide-Hurst C, Lu M, Kim J, Wen N, *et al*. (2013) Voxel-based statistical analysis of uncertainties associated with deformable image registration. *Physics in Medicine and Biology* 58(18):6481-6494.

236. Hoffmann C, Krause S, Stoiber EM, Mohr A, Rieken S, *et al*. (2014) Accuracy quantification of a deformable image registration tool applied in a clinical setting. *Journal of Applied Clinical Medical Physics* 15(1):237-245.

237. Loeckx D, Slagmolen P, Maes F, Vandermeulen D, & Suetens P (2010) Nonrigid image registration using conditional mutual information. *IEEE Transactions on Medical Imaging* 29(1):19-29.

238. Schiing J, Gomes LCR, Benavides E, Nguyen T, Paniagua B, *et al*. (2014) Regional 3D superimposition to assess temporomandibular joint condylar morphology. *Dentomaxillofacial Radiology* 43(1):20130273.

239. Gibbs HC, Dodson CR, Bai Y, Lekven AC, & Yeh AT (2013) Combined lineage mapping and fate specification profiling with NLOM-OCM using sub-10-fs pulses. *Imaging in Developmental Biology,* Proceedings of SPIE, ed Fraser SE & Rollins AM, Vol 85930K.

240. Reifers F, Bohli H, Walsh EC, Crossley PH, Stainier DYR, *et al*. (1998) Fgf8 is mutated in zebrafish acerebellar (ace) mutants and is required for maintenance of midbrain-hindbrain boundary development and somitogenesis. *Development* 125(13):2381-2395.

241. Frise E, Hammonds AS, & Celniker SE (2010) Systematic image-driven analysis of the spatial *Drosophila* embryonic expression landscape. *Molecular Systems Biology* 6:345.

242. Gutierrez J (2009) A developmental systems perspective on epistasis: computational exploration of mutational interactions in model developmental regulatory networks. *PLoS One* 4(9):e6823.

243. Christiansen JH, Yang Y, Venkataraman S, Richardson L, Stevenson P, *et al*. (2006) EMAGE: a spatial database of gene expression patterns during mouse embryo development. *Nucleic Acids Research* 34:637-641.

244. Wong F, Welten MCM, Anderson C, Bain AA, Liu JH, *et al*. (2013) eChickAtlas: an introduction to the database. *Genesis* 51(5):365-371.

245. Okubo R, Dauga D, Robin F, & Lemaire P (2008) Quantitative analysis of morphogenetic change during gastrulation movement in ascidian *Ciona intestinalis* by constructing 3-D virtual embryo. *Genes & Genetic Systems* 83(6):502-502.

246. Tassy O, Daian F, Hudson C, Bertrand V, & Lemaire P (2006) A quantitative approach to the study of cell shapes and interactions during early chordate embryogenesis. *Current Biology* 16(4):345-358.

247. Gerth VE, Katsuyama K, Snyder KA, Bowes JB, Kitayama A, *et al*. (2007) Projecting 2D gene expression data into 3D and 4D space. *Developmental Dynamics* 236(4):1036-1043.

248. Eames BF, DeLaurier A, Ullmann B, Huycke TR, Nichols JT, *et al*. (2013) FishFace: interactive atlas of zebrafish craniofacial development at cellular resolution. *BMC Developmental Biology* 13:23.

249. Kerwin J, Yang Y, Merchan P, Sarma S, Thompson J, *et al*. (2010) The HUDSEN Atlas: a three-dimensional (3D) spatial framework for studying gene expression in the developing human brain. *Journal of Anatomy* 217(4):289-299.

250. Gibbs HC, Bai YQ, Lekven AC, & Yeh AT (2014) Imaging embryonic development with ultrashort pulse microscopy. *Optical Engineering* 53(5):051506.

251. Xiao A, Wang ZX, Hu YY, Wu YD, Luo Z, *et al*. (2013) Chromosomal deletions and inversions mediated by TALENs and CRISPR/Cas in zebrafish. *Nucleic Acids Research* 41(14):1-13.

252. Jaszai J, Reifers F, Picker A, Langenberg T, & Brand M (2003) Isthmus-to-midbrain transformation in the absence of midbrain-hindbrain organizer activity. *Development* 130(26):6611-6623.

253. Dyer C, Blanc E, Hanisch A, Roehl H, Otto GW, *et al*. (2014) A bi-modal function of Wnt signalling directs an Fgf activity gradient to spatially regulate neuronal differentiation in the midbrain. *Development* 141(1):63-72.

254. Lassiter RNT, Stark MR, Zhao TY, & Zhou CJJ (2014) Signaling mechanisms controlling cranial placode neurogenesis and delamination. *Developmental Biology* 389(1):39-49.

255. Dworkin S, Darido C, Georgy SR, Wilanowski T, Srivastava S, *et al*. (2012) Midbrain-hindbrain boundary patterning and morphogenesis are regulated by diverse grainy head-like 2-dependent pathways. *Development* 139(3):525-536.

256. Bhat N & Riley BB (2011) Integrin-alpha 5 coordinates assembly of posterior cranial placodes in zebrafish and enhances Fgf-dependent regulation of otic/epibranchial cells. *PLoS One* 6(12):e27778.

257. Kwon HJ, Bhat N, Sweet EM, Cornell RA, & Riley BB (2010) Identification of early requirements for preplacodal ectoderm and sensory organ development. *PLoS Genetics* 6(9): e1001133.

258. Lauter G, Soll I, & Hauptmann G (2011) Multicolor fluorescent in situ hybridization to define abutting and overlapping gene expression in the embryonic zebrafish brain. *Neural Development* 6:10.

259. Buschke DG, Squirrell JM, Fong JJ, Eliceiri KW, & Ogle BM (2012) Cell death, non-invasively assessed by intrinsic fluorescence intensity of NADH, is a predictive indicator of functional differentiation of embryonic stem cells. *Biology of the Cell* 104(6):352-364.

260. Gutzman JH & Sive H (2010) Epithelial relaxation mediated by the myosin phosphatase regulator Mypt1 is required for brain ventricle lumen expansion and hindbrain morphogenesis. *Development* 137(5):795-804.

261. Reim G & Brand M (2002) Spiel-ohne-grenzen/pou2 mediates regional competence to respond to Fgf8 during zebrafish early neural development. *Development* 129(4):917-933.

262. Gutzman JH, Graeden EG, Lowery LA, Holley HS, & Sive H (2008) Formation of the zebrafish midbrain-hindbrain boundary constriction requires laminin-dependent basal constriction. *Mechanisms of Development* 125(11/12):974-983.

263. Kicheva A, Bollenbach T, Wartlick O, Julicher F, & Gonzalez-Gaitan M (2012) Investigating the principles of morphogen gradient formation: from tissues to cells. *Current Opinion in Genetics & Development* 22(6):527-532.

264. Yoshiba S & Hamada H (2014) Roles of cilia, fluid flow, and Ca2+ signaling in breaking of left-right symmetry. *Trends in Genetics* 30(1):10-17.

265. Kishimoto N, Alfaro-Cervello C, Shimizu K, Asakawa K, Urasaki A, *et al*. (2011) Migration of neuronal precursors from the telencephalic ventricular zone into the olfactory bulb in adult zebrafish. *Journal of Comparative Neurology* 519(17):3549-3565.

266. Lee SMK, Danielian PS, Fritzsch B, & McMahon AP (1997) Evidence that Fgf8 signalling from the midbrain-hindbrain junction regulates growth and polarity in the developing midbrain. *Development* 124(5):959-969.

267. Nagai T, Ibata K, Park ES, Kubota M, Mikoshiba K, *et al*. (2002) A variant of yellow fluorescent protein with fast and efficient maturation for cell-biological applications. *Nature Biotechnology* 20(1):87-90.

268. Darwin CR (1909) *The origin of species*. (P.F. Collier & Son, New York) 1st ed.